

UCLA

UCLA Electronic Theses and Dissertations

Title

Towards High Sensitivity and High Spatial Resolution Positron Emission Tomography Imaging

Permalink

<https://escholarship.org/uc/item/4mp632hr>

Author

Gu, Zheng

Publication Date

2014

Peer reviewed|Thesis/dissertation

UNIVERSITY OF CALIFORNIA

Los Angeles

Towards High Sensitivity and High Spatial Resolution
Positron Emission Tomography Imaging

A dissertation submitted in partial satisfaction of the
requirements for the degree Doctor of Philosophy
in Biomedical Physics

by

Zheng Gu

2014

© Copyright by

Zheng Gu

2014

ABSTRACT OF THE DISSERTATION

Towards High Sensitivity and High Spatial Resolution
Positron Emission Tomography Imaging

by

Zheng Gu

Doctor of Philosophy in Biomedical Physics

University of California, Los Angeles, 2014

Professor Arion-Xenofon Hadjioannou, Chair

High sensitivity and high resolution have been pursued as some of the most important research goals for preclinical Positron Emission Tomography (PET) imaging. PETbox4, a new, fully tomographic bench top PET scanner dedicated for mouse imaging, was designed and developed in this work. The aim of the PETbox4 scanner is to achieve very high sensitivity and produce high quality PET tomographic images for molecular imaging based biomedical research. Performance of the prototype PETbox4 system was characterized using the National Electrical Manufacturers Association (NEMA) NU 4-2008 standards.

Due to the different characteristics caused by the compact geometrical factors, PETbox4 requires data acquisition protocols that differ from those optimized for conventional large diameter ring systems. In this work the energy window for data acquisitions with PETbox4 was

optimized using the Geant4 Application for Tomographic Emission (GATE) simulation. A lower level discriminator (LLD) of 350 keV was proposed as the optimized energy threshold.

Pulse pileup is a common problem in multiplexed scintillator detectors readout by resistor divider networks. In this work, a new pileup rejection method named position shift rejection (PSR) is introduced. The PSR method is based on the detection of position shifts on event location as the signal is being integrated. Both simulations and physical measurements show that PSR performs more accurate rejection and avoids erroneous rejection and loss of sensitivity compared to the conventional leading edge rejection (LER) method.

A new phoswich DOI Detector with crystal scatter identification capability is being designed and developed for implementation in a next generation small animal PET system at UCLA. Both simulations and measurements were performed to evaluate the characteristics and benefits of the proposed design. In conclusion, these results demonstrate that the proposed detector is feasible and can potentially lead to a high spatial resolution, high sensitivity and DOI PET system.

The dissertation of Zheng Gu is approved.

Magnus Dahlbom

Anna Wu Work

Katsushi Arisaka

Arion-Xenofon Hadjioannou, Committee Chair

University of California, Los Angeles

2014

TABLE OF CONTENTS

Chapter 1 Introduction	1
1.1 Objective	2
1.2 Introduction and background	6
1.2.1 System development	6
1.2.1.1 PET basics	6
1.2.1.2 PETbox	7
1.2.1.3 PETbox4	8
1.2.2 System optimization	10
1.2.2.1 Energy window optimization	10
1.2.2.2 Pileup rejection	12
1.2.3 The next generation	14
1.3 References	16
Chapter 2 System Development.....	23
2.1. Introduction.....	25
2.2. Materials and methods	26
2.2.1. System description	26
2.2.2. Energy resolution and flood histograms.....	28
2.2.3. Spatial resolution.....	29
2.2.4. Scatter and count-rate performance.....	31
2.2.5. Imaging studies	32
2.3. Results.....	33
2.3.1. Energy resolution and flood histograms.....	33
2.3.2. Spatial resolution.....	33
2.3.3. Sensitivity.....	35
2.3.4. Scatter and count-rate performance.....	36
2.3.5. Imaging studies	38
2.4. Discussion	42
2.5. Conclusion	45

2.6. Acknowledgements.....	45
2.7. References.....	45
Chapter 3 System Optimization: Energy Window Optimization	48
3.1. Introduction.....	49
3.2. Methods.....	50
3.2.1. Modeling the System with GATE.....	50
3.2.2. Voxelized Phantom	50
3.2.3. Event Classification.....	51
3.2.4. Energy Window Optimization Based on NECR and SF.....	51
3.2.5. NEMA NU-4 Image Quality Phantom.....	52
3.3. Results.....	53
3.3.1. Event Classification.....	53
3.3.2. Energy Window Optimization	54
3.3.3. NEMA NU-4 Image Quality Phantom.....	55
3.4. Discussion	56
3.5. Conclusion	57
3.6. Appendix.....	57
3.7. Acknowledgement	57
3.8. References.....	57
Chapter 4 System Optimization: Pileup Rejection	59
4.1. Introduction.....	60
4.2. Methods.....	61
4.2.1. Pileup in PETbox4	61
4.2.2. Pulse leading edge rejection (LER) method.....	63
4.2.3. Position shift rejection (PSR) method.....	63
4.2.4. Synthetic pulse train evaluation	65
4.2.5. Measurement verification.....	66
4.3. Results.....	68
4.3.1. Synthetic pulse train evaluation	68
4.3.2. Measurement verification.....	68

4.4. Discussion and Conclusions	74
4.5. References.....	77
Chapter 5 The Next Generation	79
5.1. Introduction.....	80
5.2. Methods.....	82
5.2.1. Detector Description	82
5.2.2. Simulation.....	84
5.2.3. Measurement.....	86
5.3. Results.....	88
5.3.1. Simulation	88
5.3.2. Measurement.....	89
5.4. Discussion	92
5.5. Conclusion	95
5.6. References.....	96
Chapter 6 Conclusions and Future Work.....	101
6.1. System development	102
6.2. System optimization.....	103
6.2.1. Energy window optimization	103
6.2.2. Pileup rejection.....	104
6.3. The next generation.....	105
6.4. References.....	107

ACKNOWLEDGEMENTS

I would like to first of all acknowledge my committee chair and mentor, Arion Hadjioannou. I am grateful for his consistent guidance and support through all my projects past and present.

I would also like to thank my doctoral committee including Magnus Dahlbom, Anna Wu and Katsushi Arisaka, for their insightful discussions and review of this work.

I have been very fortunate to be surrounded by great scientists in our Imaging Sciences Lab. I would like to thank David Prout for his instruction and assistance from the beginning on nuclear instrumentation and radiation detection. I thank Richard Taschereau for his work on the image reconstruction and corrections for the PETbox4 system, as well as his instruction and assistance on my simulation studies. Also I thank three former group members: Qinan Bao, Hui Zhang and Ali Douraghy. Their work is educational to me and important for this project. I would like to thank Bob Silverman, Hongkai Wang, Alex Dooraghi, Yanisley Valenciaga, Henry Herman and Brittany Berry-Pusey for their generous help, advice and encouragement through the years and their contributions to this project.

I would like to thank the staff of the Crump Imaging facility at UCLA including David Stout, Waldemar Ladno, Jeffrey Collins, Darin Williams, Graciela Flores and Jason Lee for their assistance with obtaining the ^{18}F solution and performing the mouse scans.

I would also like to thank Michael Phelps, Richard Tavaré, Anna Wu, Melissa McCracken and Owen Witte from the department of molecular and medical pharmacology at UCLA for their contribution in performing mouse studies using the PETbox4 system.

I would like to thank Patrick Phelps and Nam Vu from Sofie Biosciences for their contribution in developing and commercializing the PETbox4 system.

Thank to our collaborators: Bing Bai from University of Southern California for his work on the normalization for the PETbox4 system, and Yuan-Chuan Tai from Washington University, Saint Louis for providing an LSO testing array in the early stage of developing the phoswich DOI detector.

It was a great pleasure coming into the biomedical physics program. Thanks to Mike McNitt-Gray, for leading the program and the generous help; To Magnus Dahlbom for teaching me the fundamentals of nuclear instrumentation. I also thank all the administrators: Terry Moore and Reth Thach Im at Biomedical Physics Program, and Erika Corrin and Karen Lum at Crump Institute for Molecular Imaging.

Finally, I would like to thank my mother for her everlasting love and support.

Chapter 5 has been submitted to a peer-reviewed journal for publication.

I also thank IOP Publishing Ltd for allowing the reprint of the paper shown in Chapter 2, and thank IEEE for allowing the reprint of the paper shown in Chapter 3.

This dissertation work is supported in part by the National Institutes of Health under grant no. R24CA92865, in part by the Department of Energy under Contract no. DE-FG02-06ER64249, and in part by the UCLA Foundation from a donation made by Ralph and Marjorie Crump for the UCLA Crump Institute for Molecular Imaging.

VITA

- 2008 B.S., Engineering Physics
Tsinghua University
Beijing, P.R. China
- 2009 UCLA Chancellor's Prize
UCLA Graduate Division
Los Angeles, California
- 2010 Graduate Student Travel Award
UCLA, Department of Molecular and Medical Pharmacology
Los Angeles, California
- 2013 Graduate Division Unrestricted Fellowship
UCLA Graduate Division
Los Angeles, California
- 2014 Internship
Sofie Biosciences
Culver City, California
- 2009-14 Graduate Student Researcher
UCLA, Department of Molecular and Medical Pharmacology
Los Angeles, California

PUBLICATIONS AND PRESENTATIONS

Gu Z, Prout D L, Silverman R W, Herman H, Dooraghi A and Chatziioannou A F A DOI Detector with Scatter Identification Capability for High Sensitivity, High Spatial Resolution PET Imaging *IEEE Nuclear Science Symposium and Medical Imaging Conference, Seattle, USA, November 8- 15,2014*

Gu Z, Prout D L, Valenciaga Y and Chatziioannou A F A Digital Pulse Library for the Optimization of Signal Processing in PET *IEEE International conference on imaging systems & techniques, Santorini, Greece, October 14-17,2014*

Gu Z, Q Bao, Taschereau R, Wang H, Bai B and Chatziioannou A F 2014 Optimization of the energy window for PETbox4, a preclinical PET tomograph with a small inner diameter *IEEE Transactions on Nuclear Science* vol. 61, pp. 1164-1173.

Gu Z, Taschereau R, Vu N T, Wang H, Prout D L, Silverman R W, Bai B, Stout D B, Phelps M E and Chatziioannou A F 2013 NEMA NU-4 performance evaluation of PETbox4, a high sensitivity dedicated PET preclinical tomograph *Physics in Medicine and Biology* **58** 3791-814

Gu Z, Prout D L, Bai B and Chatziioannou A F 2013 A New Pileup Rejection Method Based on Position Shift Identification *IEEE Nuclear Science Symposium and Medical Imaging Conference, Seoul, Korea, October 27–November 2, 2013*

Prout D L, **Gu Z**, Valenciaga Y and Chatziioannou A F 2013 Investigation of silicon photomultipliers for use in preclinical tomographs with BGO arrays *IEEE Nuclear Science Symposium and Medical Imaging Conference, Conference record*

Lasnon C, Quak E, Briand M, **Gu Z**, Louis M H and Aide N 2013 Contrast-enhanced small-animal PET/CT in cancer research: strong improvement of diagnostic accuracy without significant alteration of quantitative accuracy and NEMA NU 4-2008 image quality parameters *EJNMMI Res* **3** 5

Gu Z, Prout D L and Chatziioannou A F 2012 An Adaptive Method for Triggering, Event Validation and Pulse Pile-up Recovery in PET *IEEE Nuclear Science Symposium and Medical Imaging Conference, Conference record*

Gu Z, Bao Q, Taschereau R, Wang H, Vu N T and Chatziioannou A F 2012 Optimization of Energy Window and Multiple Event Acceptance Policy for PETbox4, a High Sensitivity Preclinical Imaging Tomograph *IEEE Nuclear Science Symposium and Medical Imaging Conference, Conference record*

Gu Z, Prout D L, Valenciaga Y and Chatziioannou A F 2012c A Digital Pulse Library for the Optimization of Signal Processing in PET *IEEE Nuclear Science Symposium and Medical Imaging Conference, Anaheim, California USA, October 29-November 3, 2012*

Wang H K, Stout D B, Taschereau R, **Gu Z**, Vu N T, Prout D L and Chatziioannou A F 2012 MARS: a mouse atlas registration system based on a planar x-ray projector and an optical camera *Physics in Medicine and Biology* **57** 6063-77

Valenciaga Y, Prout D L, **Gu Z**, Taschereau R and Chatziioannou A F 2012 Matched Filter for Event Identification and Processing in PET *IEEE Nuclear Science Symposium and Medical Imaging Conference, Conference record*

Gu Z, Taschereau R, Vu N T, Wang H, Prout D L, Silverman R W, Stout D B, Phelps M E and Chatziioannou A F 2011 Design and initial performance of PETbox4, a high sensitivity preclinical imaging tomograph *IEEE Nuclear Science Symposium and Medical Imaging Conference, Conference record* 2328-31

Gu Z, Bao Q and Chatziioannou A F 2010 Evaluation of the detection limit at low activity levels for three preclinical PET systems *IEEE Nuclear Science Symposium and Medical Imaging Conference, Conference record* 3619-21

Chapter 1

Introduction

Chapter 1 Introduction

1.1 Objective

Translational research is essential for improving human health. New knowledge, mechanisms, and techniques generated by advances in lab bench research, especially based on molecular biology and sequencing of the human genome, have been translated into new approaches for prevention, diagnosis, and treatment of disease in the clinical bedside. Therefore, the National Institutes of Health (NIH) has made translational research a top priority [1].

Biomedical translational research has always relied on in-vivo experiments with animal models of human disease due to the similarities of their biochemical interactions and pathways to those of humans [2]. Among the widely used animal models, genetically modified mice have been made the animal of choice to mimic human subjects for both healthy and diseased states [3]. The mouse genome was the second mammalian genome to be fully sequenced after the human [4]. The use of mouse models is further supported by the relatively low cost of maintaining colonies due to the rapid reproduction and short normal life span of mice [5]. It is worthwhile to note that genetically modified mice represent more than 90% of the mammalian preclinical disease models in biological research [6].

Molecular imaging technologies play an important role in examining the integrative functions of molecules, cells, organ systems, and whole organisms [5, 7]. Positron emission tomography (PET) is an imaging modality that enables non-invasive, in vivo detection and quantification of biological processes at the molecular level. In-vivo imaging of animals using small animal PET has been a driving force behind the advances of molecular biology [7-10].

The use of mice as animal models for applications in pharmacology, genetics, pathology and oncology, demands preclinical PET scanners featuring high resolution and high sensitivity, to visualize subtle spatial distribution and quantify low concentrations of PET probes [11]. Advances in spatial resolution and sensitivity performance of imaging systems can open up applications currently out of the range of PET because of resolution limitations, such as mouse brain imaging and early lesion and metastasis detection in mouse models of cancer [12]. Therefore, high sensitivity and high resolution have been pursued as some of the most important research goals for preclinical PET imaging [13].

On the other hand, it is also important to take into account the targeted applications of the PET imaging system, the availability and cost of the technologies, and the ease and cost of its operation. Compromises in performance characteristics might be necessary to make a compact, relatively low-cost, high-throughput, and user friendly benchtop system widely available to the research community and the pharmaceutical and biotechnology industries in order to maximize the number of the biological scientists who capitalize on the advantages of using PET imaging for research [14].

Investigators are creating a wide variety of outstanding technologies for facilitating the advance of biomedical research. At UCLA, we have been looking at preclinical imaging as an integrated experiment and are addressing some key components within the context of the entire imaging process. Our aim is to establish a high performance, cost effective and user friendly molecular imaging platform, leading to increased use and acceptance of in vivo molecular imaging techniques in biological laboratories. Investigations in our institute include (Figure 1.1):

- (1) Vascular access system (VAS) for probe injection and eventually blood sampling [15].

- (2) Animal handling including reproducible positioning, anesthesia delivery, temperature regulation and physiological monitoring [16].
- (3) Small animal PET imaging [17, 18].
- (4) Anatomical reference and data analysis [19, 20].

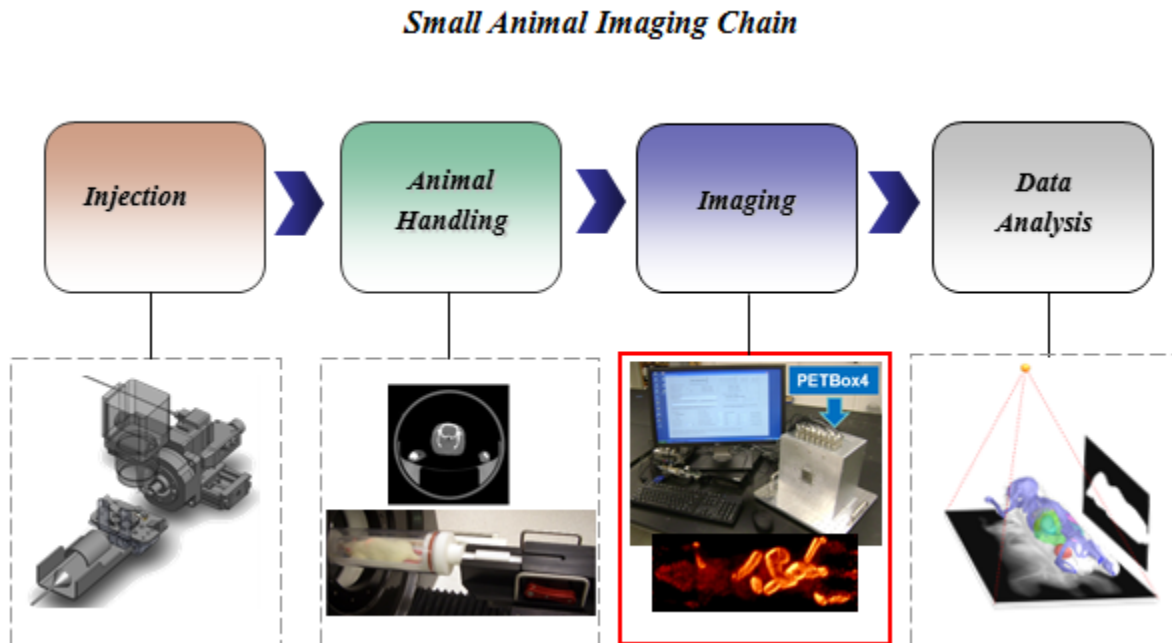


Figure 1. 1 Small animal imaging chain at the Crump Imaging Institute at UCLA.

The work presented here concentrates on the third component of the preclinical imaging chain shown in Figure 1.1, describing methods developed at the Crump Institute for Molecular Imaging at UCLA towards high sensitivity, high resolution and low cost small animal PET imaging. In chapter 2, the design, development and performance evaluation of PETbox4, a very high sensitivity PET dedicated to mouse imaging are described in detail. Due to the compact geometry of the PETbox4 in comparison to most other preclinical imaging systems, optimization of the imaging protocol is necessary to improve imaging performance and is discussed in Chapter 3. A novel pileup event rejection technique improving the count rate performance of the

PETbox4 is described in Chapter 4. Lastly, towards the next generation system with further sensitivity and resolution improvements, a phoswich DOI detector with scatter identification capability is designed and developed, as described in Chapter 5.

1.2 Introduction and background

1.2.1 System development

1.2.1.1 PET basics

Positron emission tomography (PET) is a nuclear medical imaging technique that allows physicians or researchers to image and quantitatively measure the spatial-temporal distribution of positron-emitting radio-labeled biomarkers in-vivo. During PET imaging, a biomarker labeled with a positron-emitting radionuclide is administered to the subject. The introduced biomarker gives rise to a distribution that reveals the characteristics of the biological process within the subject. The radioactive atoms in the administered biomarker decay in a process where a proton is converted into a neutron and a positron is emitted from the nucleus with a certain amount of energy. The positron then travels through the surrounding medium and once it has lost sufficient kinetic energy through Coulomb interactions, it pairs with an electron partner forming an unstable positronium. Shortly the matter-antimatter pair annihilates and two gamma photons each with 511 keV of energy are emitted 180° apart due to conservation of mass and momentum.

A PET tomograph retrieves the spatial distribution of the administered radioactive biomarker based on detection of the two 511 keV annihilation photons emitted from a positron decay. Sensitive detectors within the PET scanner transfer the energy deposited from interactions with the annihilation photons to electronic signals, based on which the position, energy and timing information of each detection are retrieved and the qualified coincidence events are recorded. Three dimensional images representing the distribution of the radioactive biomarker within the subject can be mathematically reconstructed from this set of qualified coincidence measurements [21].

1.2.1.2 PETbox

A low-cost, user friendly benchtop PET system can facilitate the use and acceptance of in vivo PET imaging techniques in biological laboratories, and therefore has been pursued as an important research goal [11, 13, 14]. The largest part of the cost for a PET system comes from the detectors and the corresponding data acquisition electronics. Hundreds of detector blocks comprised of tens of thousands of crystal elements, together with the costly data acquisition electronics are required in traditional PET scanner configurations [22]. As a result, most preclinical PET tomographs present significant up-front manufacturing, operation and maintenance costs, greatly diminishing the potential use basis.

In 2009, an integrated benchtop preclinical PET scanner, PETbox, was designed and developed at Crump Institute for Molecular Imaging at UCLA [17, 23]. The goal of the PETbox was to perform high throughput quantitative pharmacokinetic and pharmacodynamic studies dedicated for laboratory mice only, with a good overall system performance and at the lowest cost and system complexity. Since the detector cost of a PET tomograph is at a first approximation proportional to the physical detector surface, the PETbox system employed two opposing stationary flat panel detectors measuring $\sim 5 \times 10 \text{ cm}^2$ (the minimum required detector surface area for covering the field of view for mice whole body imaging without any moving components), forming a dual-head geometry, limited angle tomography system. The compact benchtop configuration of the PETbox successfully reduced the cost as well as the space needed for researchers to access PET imaging technology, with many phantom and in vivo animal studies demonstrating the capabilities of the PETbox for small animal imaging [17].

1.2.1.3 PETbox4

The volume and mass of mice are approximately 3000 times smaller than that of humans and 10–20 times smaller than an average rat. The spatial resolution of a PET scanner dedicated for mouse imaging should be similarly higher and the voxel size in the reconstructed images should also be reduced according to sampling theory [24]. To obtain images of the same statistical quality as in humans, the number of counts detected per voxel, which is inversely proportional to voxel volume, could be compensated by either increasing the radioactivity of injected probes or by improving the sensitivity of the scanner. However, with a typical amount of radioactivity administered (7.4 MBq (200 μ Ci)) [25], the concentration of radionuclides in mice is already much higher than that in humans. It has been shown that during preclinical PET imaging procedures, major organs like the bladder, brain, heart, and tumor xenografts of mice could receive an absorbed dose in a range for which biological effects such as stimulated cell proliferation [26], induced radio-resistance [27], elevated gene expression [28], have been reported [29, 30]. Those biological effects may interfere and bias the results in pharmaceutical and genetic studies, leading to discrepancies on translational research between mouse models and clinical applications. Also, for many applications such as neuroreceptor imaging, the signal of concern can be inherently limited by the number of binding sites available, as well as by the specificity and affinity of the radiotracers. The injected probe mass, which should be below levels that perturb the studied biological system, may limit the amount of radioactivity that can be injected into a mouse to the range of 0.37–3.7 MBq (10–100 μ Ci) [31]. High sensitivity imaging systems are therefore desirable to obtain count statistics adequate per volumetric resolution element with lower amounts of radioactivity and reduce radiation dose delivered to mice. This is especially important in the case of longitudinal studies, in which multiple

experiments take place over a period of time. In addition, high sensitivity also contributes to higher imaging throughput, by maintaining optimized imaging performance within the required scan time, which is especially important when imaging a considerable number of subjects in one study [32]. Besides, an additional benefit from the high sensitivity and low injected activity is the reduced exposure to the scanner operator.

PETbox4, the second generation of the previous prototype PETbox system, is a new, fully tomographic PET scanner developed by our group since 2010 [18]. Several design concepts of the PETbox including the compact geometry, low cost, dedicated mice imaging, are also adopted by the PETbox4 system. The aim of the PETbox4 scanner is to achieve very high sensitivity and produce high quality PET tomographic images for molecular imaging based biomedical research. The high sensitivity of the PETbox4 system is achieved by employing two additional detector blocks on the sides of the PETbox system to maximize the solid angle coverage, and by using thicker crystals for higher 511 keV gamma photon detection efficiency. The spatial resolution of the PETbox4 is also significantly improved. Because PETbox is a dual-head limited angle tomograph, the data in the anterior-posterior (AP) direction is not completely sampled, leading to lower spatial resolution in the AP direction. The fully tomographic geometry of the PETbox4 improves the data sampling completeness at all angles. As a result, the resolution along the AP direction is improved as well as the quantification accuracy. The design, development and performance evaluation of the PETbox4 system are described in detail in chapter 2.

1.2.2 System optimization

1.2.2.1 Energy window optimization

The main interaction types in transferring the energy of the 511 keV photons to matter are the photoelectric effect and Compton scattering. The photoelectric effect is an atomic absorption process in which the total energy of an incident photon is absorbed in the interaction. In Compton scattering, the incident photon is deflected through a scattering angle and loses part of its energy in the process, which is transferred to a recoil electron [21].

Both of these two interaction types can contribute to useful detections in PET imaging. Photoelectric effect is the most desirable interaction in annihilation photon detection. Maximum photon energy is deposited in a photoelectric interaction, leading to the optimal performance in event triggering, positioning and qualification. The 511 keV photon may also undergo single Compton scattering in a crystal, deposit part of its energy and then escape the detector. These single Compton scattering interactions may also convey correct position information and therefore can increase the detection efficiency if accurately detected.

Compton scatter is one of the main sources of coincidence detections with incorrect position information in PET. When the radioactive probe is embedded at depth within the tissue, as it is for most in vivo measurements, one (or both) of the photons from an annihilation event can undergo scattering in the object before detected in a detector. The 511 keV gamma photons also have a probability of undergoing a Compton scatter interaction in one detector and then being detected in a second detector, resulting in backscatter coincidence events [33]. Those resulting scatter coincidences provide incorrect localization of the line of response (LOR) corresponding to the positron annihilation event, leading to a broad distribution of mispositioned

events that form a hazy background in the reconstructed images. This loss of image contrast can result in degraded visibility of both large low-contrast objects and fine details in the image, and cause errors in the quantitative relationship between the measured image intensity and the actual distribution of activity in the object.

Because the Compton-scattered photons have lower energy, it is possible to discriminate against their further detection using energy thresholds. An energy window, including a lower level discriminator (LLD) and an up level discriminator (ULD), is commonly used to select for imaging only those detector output signals within a desired energy range. Energy discrimination provides a means to discriminate against gamma rays that are initially scattered in the object or elsewhere before reaching the detector and would therefore give a false position indication. On the other hand, it is not possible to distinguish between scatter events in the body versus single Compton scatter events of annihilation photons in the detector merely based on event energy. Using a narrower energy window for object scatter rejection also decreases the useful crystal Compton scatter count rate, reducing system sensitivity and leading to increased statistical noise in the image. Therefore, a reasonable tradeoff between the detection efficiency and scatter rejection for PET imaging systems needs to be obtained to achieve an overall optimal imaging quality. In Chapter 3, the imaging protocols including energy window and event acceptance policy were optimized on the basis of investigating the contributions from all event types in the scanner.

1.2.2.2 Pileup rejection

The most common type of PET detector is based on inorganic scintillator materials due to their high stopping power. When an incoming annihilation photon interacts with the scintillator, a large number of electron-hole pairs are formed. These electrons drop into the activator sites (deliberately added impurities) of the scintillator, creating a neutral configuration that has its own set of excited energy states. The excited impurity configurations subsequently de-excite to the ground state, emitting photons in the visible light energy range (1-2 eV). The half-life characteristic of the excited states of the scintillator determines the time characteristics of the emitted scintillation light [34]. The *decay time* τ for commonly used scintillators for PET detectors are summarized in table 1.1. Due to the coincidence detection and event qualification schemes of PET, these detectors need to be operated in event-mode, processing a single event at a time for retrieving energy and position information of individual detections. Because of the non-zero response time of the scintillator based PET detectors, a period of time equal to 3τ is commonly required in a standard signal measurement procedure to integrate the scintillation pulses for collecting about 95% scintillation light. This event processing duration inhibits the detector's ability to process a second event within this time period. If a second pulse occurs within the 3τ period before the first pulse has disappeared, the two pulses will overlap to form a single distorted pulse also called a *pileup event*. Pileup events cause event loss and mispositioning, energy spectrum distortion and reduced timing resolution, leading to a deterioration of signal-to-noise ratio (SNR), a loss of resolution and contrast and introduction of image artifacts in PET images.

Table 1. 1 The decay time of commonly used scintillators for PET detectors

Scintillator	NaI	BGO	LSO	LYSO	GSO
Decay constant (ns)	230	300	40	42	50-60

The highly multiplexed methods of readout in conventional PET detectors further exacerbate the event pileup problem. In the PETbox4 system, each detector panel consists of a 24×50 pixelated BGO scintillator array. The scintillation light generated by gamma-ray interactions in the detector block is sensed by two position-sensitive photomultiplier tubes (PSPMT; Hamamatsu Photonics, Bridgewater, NJ) that completely cover one of the flat faces of the detector block. Each scintillation event generates electronic pulses of significant amplitude from the PMT anodes that are near the location of the interaction. The "center of gravity" of the scintillation light is interpolated from the 128 PMT anode signals using a charge division process [35], in which a portion of each PMT anode signal is coupled to two position encoding outputs (denoted as the x and y signals), and the summed output from all the PMT anodes is used (denoted as the sum signals) as a measure of the total amount of light produced by a scintillation event in the detector. The resulting analog x, y position signals and the sum energy signal are digitized by free running analogue-to-digital converters (ADC) and accumulated in a field programmable gate array (FPGA) with an integration period of 3τ . The two-dimensional positions of each event measured by the detector are calculated as $X=x/\text{sum}$ and $Y=y/\text{sum}$ by the event position logic [18]. Because of this multiplexing scheme, a pileup event appears as long as two or more photons hit one detector panel within one integration period.

The high absolute sensitivity of PETbox4, together with the long decay time τ of BGO used as the detector material and the highly multiplexed electronics lead to a significant fraction

of pileup, reached at lower total activity for this scanner, than for comparable instruments. Therefore, it is important to implement pileup event correction for PETbox4. In Chapter 4, a novel pileup rejection method named Position Shift Rejection (PSR) is introduced.

1.2.3 The next generation

High sensitivity and high spatial resolution have been pursued as some of the most important research goals for preclinical PET imaging [13]. For conventional pixelated scintillator detectors, the spatial resolution is determined by the cross section of the scintillator crystal elements [36]. The sensitivity can be increased by employing a compact system geometry to maximize solid angle coverage, and by using long crystals for higher overall 511 keV gamma photon detection efficiency.

Unfortunately, long and narrow crystals in a small diameter gantry lead to increased penetration of oblique incident gamma rays before interaction. This causes event mispositioning also called parallax error, degrading the spatial resolution uniformity and distorting the appearance of the source [37]. Therefore, detectors with the capability of encoding the depth of annihilation photon interaction (DOI) are necessary. Much effort has been devoted to develop DOI PET detectors over the past several years [38-55]. Among those designs, phoswich detector approaches [53-55] obtain DOI information by measuring differences in light decay time between multiple layers of different scintillators. The phoswich detector design has attracted considerable interest and has been employed in several prototype scanners and commercial systems [56-58]. Improved spatial resolution uniformity has been achieved in these phoswich DOI scanners compared to scanners of single layer design with equivalent scintillator volume and no DOI capability [59].

Inter-crystal scatter (ICS) events, for which the incoming annihilation photons interact with more than one detection element within the same block detector, is another cause of event mispositioning in addition to the parallax error. As the detection elements become narrower and longer, the fraction of these ICS events increases [60]. With conventional PET detector designs that employ Anger logic positioning schemes [61], such ICS events appear as inaccurate detections. The spatial coordinates corresponding to the energy weighted mean of the multiple interaction sites are different from the location of first interaction. This error in determining the initial interaction location reduces image contrast and degrades spatial resolution. This leads to degradation of the lesion detectability and quantitative characteristics of an imaging system [62, 63]. Therefore, appropriate ICS event identification and correction methods should be pursued if possible. Studies have shown that the capability of rejecting ICS events, or estimating the first interaction site of an ICS event using selection criteria [60, 64, 65], or maximum likelihood based on Compton kinematics [63, 66], yields improved image quality and quantification. However, those approaches require complicated and costly data acquisition systems for measuring individual interactions of the ICS events [51] and significant computational efforts for determining the location of first interaction [66], neither of which are available for conventional Anger logic detectors.

In Chapter 5, a phoswich depth of interaction (DOI) detector design composed by two layers of scintillator array made from cerium doped lutetium-yttrium oxyorthosilicate (LYSO) and bismuth germanate (BGO) is proposed. The aim of the detector design is to achieve high sensitivity and high spatial resolution PET imaging. This new design is expected to be implemented in the next generation small animal PET tomograph being developed at the Crump Institute for Molecular Imaging, at UCLA.

References

- [1] S. H. Woolf, "The meaning of translational research and why it matters," *JAMA*, vol. 299, pp. 211-3, Jan 9 2008.
- [2] H. R. Herschman, "Molecular imaging: Looking at problems, seeing solutions," *Science*, vol. 302, pp. 605-608, Oct 24 2003.
- [3] K. Paigen, "A miracle enough: the power of mice," *Nature Medicine*, vol. 1, pp. 215-20, Mar 1995.
- [4] E. Marshall, "Genome sequencing - Celera assembles mouse genome; Public labs plan new strategy," *Science*, vol. 292, pp. 822-823, May 4 2001.
- [5] R. Weissleder and U. Mahmood, "Molecular imaging," *Radiology*, vol. 219, pp. 316-333, May 2001.
- [6] D. Malakoff, "The rise of the mouse, biomedicine's model mammal," *Science*, vol. 288, pp. 248+, Apr 14 2000.
- [7] M. E. Phelps, "Positron emission tomography provides molecular imaging of biological processes," *Proc Natl Acad Sci U S A*, vol. 97, pp. 9226-33, Aug 1 2000.
- [8] S. S. Gambhir, "Molecular imaging of cancer with positron emission tomography," *Nat Rev Cancer*, vol. 2, pp. 683-93, Sep 2002.
- [9] R. Myers, "The biological application of small animal PET imaging," *Nucl Med Biol*, vol. 28, pp. 585-593, Jul 2001.
- [10] A. F. Chatziioannou, "Molecular imaging of small animals with dedicated PET tomographs," *Eur J Nucl Med*, vol. 29, pp. 98-114, Jan 2002.
- [11] S. R. Cherry, "In vivo molecular and genomic imaging: new challenges for imaging physics," *Physics in Medicine and Biology*, vol. 49, pp. R13-R48, Feb 7 2004.

- [12] S. R. Cherry, "The 2006 Henry N. Wagner lecture: Of mice and men (and positrons) - Advances in PET imaging technology," *Journal of Nuclear Medicine*, vol. 47, pp. 1735-1745, Nov 2006.
- [13] T. K. Lewellen, "Recent developments in PET detector technology," *Physics in Medicine and Biology*, vol. 53, pp. R287-R317, Sep 7 2008.
- [14] Y. C. Tai and R. Laforest, "Instrumentation aspects of animal pet," *Annual Review of Biomedical Engineering*, vol. 7, pp. 255-285, 2005.
- [15] B. N. Berry-Pusey, Y. C. Chang, S. W. Prince, K. Chu, J. David, R. Taschereau, *et al.*, "A semi-automated vascular access system for preclinical models," *Physics in Medicine and Biology*, vol. 58, pp. 5351-5362, Aug 21 2013.
- [16] C. Suckow, C. Kuntner, P. Chow, R. Silverman, A. Chatziioannou, and D. Stout, "Multimodality Rodent Imaging Chambers for Use Under Barrier Conditions with Gas Anesthesia," *Molecular Imaging and Biology*, vol. 11, pp. 100-106, Mar 2009.
- [17] H. Zhang, Q. A. Bao, N. T. Vu, R. W. Silverman, R. Taschereau, B. N. Berry-Pusey, *et al.*, "Performance Evaluation of PETbox: A Low Cost Bench Top Preclinical PET Scanner," *Molecular Imaging and Biology*, vol. 13, pp. 949-961, Oct 2011.
- [18] Z. Gu, R. Taschereau, N. T. Vu, H. Wang, D. L. Prout, R. W. Silverman, *et al.*, "NEMA NU-4 performance evaluation of PETbox4, a high sensitivity dedicated PET preclinical tomograph," *Phys Med Biol*, vol. 58, pp. 3791-3814, Jun 7 2013.
- [19] H. Wang, D. B. Stout, and A. F. Chatziioannou, "Mouse Atlas Registration with Non-tomographic Imaging Modalities-a Pilot Study Based on Simulation," *Molecular Imaging and Biology*, Oct 8 2011.
- [20] H. K. Wang, D. B. Stout, R. Taschereau, Z. Gu, N. T. Vu, D. L. Prout, *et al.*, "MARS: a mouse atlas registration system based on a planar x-ray projector and an optical camera," *Physics in Medicine and Biology*, vol. 57, pp. 6063-6077, Oct 7 2012.
- [21] S. R. Cherry, J. A. Sorenson, and M. E. Phelps, *Physics in nuclear medicine*: Elsevier Science, PA. 2003.

- [22] Q. Bao, D. Newport, M. Chen, D. B. Stout, and A. F. Chatziioannou, "Performance Evaluation of the Inveon Dedicated PET Preclinical Tomograph Based on the NEMA NU-4 Standards," *Journal of Nuclear Medicine*, vol. 50, pp. 401-408, Mar 2009.
- [23] H. Zhang, N. T. Vu, Q. Bao, R. W. Silverman, B. N. Berry-Pusey, A. Douraghy, *et al.*, "Performance Characteristics of BGO Detectors for a Low Cost Preclinical PET Scanner," *Ieee Transactions on Nuclear Science*, vol. 57, pp. 1038-1044, Jun 2010.
- [24] A. F. Chatziioannou, "PET scanners dedicated to molecular imaging of small animal models," *Mol Imaging Biol*, vol. 4, pp. 47-63, Jan 2002.
- [25] A. F. Chatziioannou, S. R. Cherry, Y. P. Shao, R. W. Silverman, K. Meadors, T. H. Farquhar, *et al.*, "Performance evaluation of microPET: A high-resolution lutetium oxyorthosilicate PET scanner for animal imaging," *Journal of Nuclear Medicine*, vol. 40, pp. 1164-1175, Jul 1999.
- [26] G. J. Wang and L. Cai, "Induction of cell-proliferation hormesis and cell-survival adaptive response in mouse hematopoietic cells by whole-body low-dose radiation," *Toxicological Sciences*, vol. 53, pp. 369-76, Feb 2000.
- [27] M. Yonezawa, "Induction of radio-resistance by low dose X-irradiation," *Yakugaku Zasshi-Journal of the Pharmaceutical Society of Japan*, vol. 126, pp. 833-840, 2006.
- [28] S. A. Amundson, M. Bittner, P. Meltzer, J. Trent, and A. J. Fornace, "Induction of gene expression as a monitor of exposure to ionizing radiation," *Radiation Research*, vol. 156, pp. 657-661, Nov 2001.
- [29] R. Taschereau and A. F. Chatziioannou, "Monte Carlo simulations of absorbed dose in a mouse phantom from 18-fluorine compounds," *Medical Physics*, vol. 34, pp. 1026-36, Mar 2007.
- [30] T. Funk, M. Sun, and B. H. Hasegawa, "Radiation dose estimate in small animal SPECT and PET," *Medical Physics*, vol. 31, pp. 2680-6, Sep 2004.
- [31] S. P. Hume, R. N. Gunn, and T. Jones, "Pharmacological constraints associated with positron emission tomographic scanning of small laboratory animals," *European Journal of Nuclear Medicine*, vol. 25, pp. 173-176, Feb 1998.

- [32] M. K. Gagnon, S. H. Hausner, J. Marik, C. K. Abbey, J. F. Marshall, and J. L. Sutcliffe, "High-throughput in vivo screening of targeted molecular imaging agents," *Proc Natl Acad Sci U S A*, vol. 106, pp. 17904-9, Oct 20 2009.
- [33] A. L. Goertzen, "Coincidences originating from a single photon: An unrecognized and potentially significant source of scatter in small animal PET?," in *IEEE Nuclear Science Symposium and Medical Imaging Conference*, Oct. 2009, pp. 2888-91.
- [34] G. F. Knoll, *Radiation Detection and Measurement*: Wiley, New Jersey.
- [35] S. Siegel, R. W. Silverman, Y. P. Shao, and S. R. Cherry, "Simple charge division readouts for imaging scintillator arrays using a multi-channel PMT," *Ieee Transactions on Nuclear Science*, vol. 43, pp. 1634-1641, Jun 1996.
- [36] J. R. Stickel and S. R. Cherry, "High-resolution PET detector design: modelling components of intrinsic spatial resolution," *Physics in Medicine and Biology*, vol. 50, pp. 179-195, Jan 21 2005.
- [37] E. J. Hoffman, T. M. Guerrero, G. Germano, W. M. Digby, and M. Dahlbom, "Pet System Calibrations and Corrections for Quantitative and Spatially Accurate Images," *Ieee Transactions on Nuclear Science*, vol. 36, pp. 1108-1112, Feb 1989.
- [38] W. H. Wong, "Designing a Stratified Detection System for Pet Cameras," *Ieee Transactions on Nuclear Science*, vol. 33, pp. 591-596, Feb 1986.
- [39] N. Zhang, C. J. Thompson, F. Cayouette, D. Jolly, and S. Kecani, "A prototype modular detector design for high resolution positron emission mammography imaging," *Ieee Transactions on Nuclear Science*, vol. 50, pp. 1624-1629, Oct 2003.
- [40] W. W. Moses and S. E. Derenzo, "Design Studies for a Pet Detector Module Using a Pin Photodiode to Measure Depth of Interaction," *Ieee Transactions on Nuclear Science*, vol. 41, pp. 1441-1445, Aug 1994.
- [41] Y. F. Yang, P. A. Dokhale, R. W. Silverman, K. S. Shah, M. A. McClish, R. Farrell, *et al.*, "Depth of interaction resolution measurements for a high resolution PET detector using position sensitive avalanche photodiodes," *Physics in Medicine and Biology*, vol. 51, pp. 2131-2142, May 7 2006.

- [42] T. Tsuda, H. Murayama, K. Kitamura, T. Yamaya, E. Yoshida, T. Omura, *et al.*, "A four-layer depth of interaction detector block for small animal PET," *Ieee Transactions on Nuclear Science*, vol. 51, pp. 2537-2542, Oct 2004.
- [43] H. Murayama, H. Ishibashi, H. Uchida, T. Omura, and T. Yamashita, "Depth encoding multicrystal detectors for PET," *Ieee Transactions on Nuclear Science*, vol. 45, pp. 1152-1157, Jun 1998.
- [44] N. Inadama, H. Murayama, M. Hamamoto, T. Tsuda, Y. Ono, T. Yamaya, *et al.*, "8-Layer DOI encoding of 3-dimensional crystal array," *Ieee Transactions on Nuclear Science*, vol. 53, pp. 2523-2528, Oct 2006.
- [45] S. Yamamoto and H. Ishibashi, "A GSO depth of interaction detector for PET," *Ieee Transactions on Nuclear Science*, vol. 45, pp. 1078-1082, Jun 1998.
- [46] Y. Yazaki, N. Inadama, F. Nishikido, T. Mitsuhashi, M. Suga, K. Shibuya, *et al.*, "Development of the X'tal Cube: A 3D Position-Sensitive Radiation Detector With All-Surface MPPC Readout," *Ieee Transactions on Nuclear Science*, vol. 59, pp. 462-468, Apr 2012.
- [47] Y. P. Shao, X. S. Sun, K. J. A. Lan, C. Bircher, K. Lou, and Z. Deng, "Development of a prototype PET scanner with depth-of-interaction measurement using solid-state photomultiplier arrays and parallel readout electronics," *Physics in Medicine and Biology*, vol. 59, Mar 7 2014.
- [48] H. N. Du, Y. F. Yang, J. Glodo, Y. B. Wu, K. Shah, and S. R. Cherry, "Continuous depth-of-interaction encoding using phosphor-coated scintillators," *Physics in Medicine and Biology*, vol. 54, pp. 1757-1771, Mar 2009.
- [49] T. Ling, T. K. Lewellen, and R. S. Miyaoka, "Depth of interaction decoding of a continuous crystal detector module," *Physics in Medicine and Biology*, vol. 52, pp. 2213-2228, Apr 21 2007.
- [50] Y. Gu, J. L. Matteson, R. T. Skelton, A. C. Deal, E. A. Stephan, F. Duttweiler, *et al.*, "Study of a high-resolution, 3D positioning cadmium zinc telluride detector for PET," *Phys Med Biol*, vol. 56, pp. 1563-84, Mar 21 2011.
- [51] A. Vandenbroucke, A. M. K. Foudray, P. D. Olcott, and C. S. Levin, "Performance characterization of a new high resolution PET scintillation detector," *Physics in Medicine and Biology*, vol. 55, pp. 5895-5911, Oct 7 2010.

- [52] D. P. McElroy, W. Pimpl, B. J. Pichler, M. Rafecas, T. Schuler, and S. I. Ziegler, "Characterization and readout of MADPET-II detector modules: Validation of a unique design concept for high resolution small animal PET," *Ieee Transactions on Nuclear Science*, vol. 52, pp. 199-204, Feb 2005.
- [53] J. Seidel, J. J. Vaquero, S. Siegel, W. R. Gandler, and M. V. Green, "Depth identification accuracy of a three layer phoswich PET detector module," *Ieee Transactions on Nuclear Science*, vol. 46, pp. 485-490, Jun 1999.
- [54] A. Saoudi, C. M. Pepin, F. Dion, M. Bentourkia, R. Lecomte, M. Andreaco, *et al.*, "Investigation of depth-of-interaction by pulse shape discrimination in multicrystal detectors read out by avalanche photodiodes," *Ieee Transactions on Nuclear Science*, vol. 46, pp. 462-467, Jun 1999.
- [55] J. B. Mosset, O. Devroede, M. Krieguer, M. Rey, J. M. Vieira, J. H. Jung, *et al.*, "Development of an optimized LSO/LuYAP phoswich detector head for the Lausanne ClearPET demonstrator," *Ieee Transactions on Nuclear Science*, vol. 53, pp. 25-29, Feb 2006.
- [56] Y. C. Wang, J. Seidel, B. M. W. Tsui, J. J. Vaquero, and M. G. Pomper, "Performance evaluation of the GE healthcare eXplore VISTA dual-ring small-animal PET scanner," *Journal of Nuclear Medicine*, vol. 47, pp. 1891-1900, Nov 2006.
- [57] P. S. Roldan, E. Chereul, O. Dietzel, L. Magnier, C. Pautrot, L. Rbah, *et al.*, "Raytest ClearPET (TM), a new generation small animal PET scanner," *Nuclear Instruments & Methods in Physics Research Section a-Accelerators Spectrometers Detectors and Associated Equipment*, vol. 571, pp. 498-501, Feb 1 2007.
- [58] H. W. A. M. de Jong, F. H. P. van Velden, R. W. Kloet, F. L. Buijs, R. Boellaard, and A. A. Lammertsma, "Performance evaluation of the ECAT HRRT: an LSO-LYSO double layer high resolution, high sensitivity scanner," *Physics in Medicine and Biology*, vol. 52, pp. 1505-1526, Mar 7 2007.
- [59] J. Seidel, J. J. Vaquero, and M. V. Green, "Resolution uniformity and sensitivity of the NIH ATLAS small animal PET scanner: Comparison to simulated LSO scanners without depth-of-interaction capability," *Ieee Transactions on Nuclear Science*, vol. 50, pp. 1347-1350, Oct 2003.
- [60] Y. P. Shao, S. R. Cherry, S. Siegel, and R. W. Silverman, "Study of inter-crystal scatter in small scintillator arrays designed for high resolution PET imaging," *Ieee Transactions on Nuclear Science*, vol. 43, pp. 1938-1944, Jun 1996.

- [61] H. O. Anger, "Scintillation Camera," *Review of Scientific Instruments*, vol. 29, pp. 27-33, 1958.
- [62] C. S. Levin, M. P. Tornai, S. R. Cherry, L. R. MacDonald, and E. J. Hoffman, "Compton scatter and X-ray crosstalk and the use of very thin intercrystal septa in high-resolution PET detectors," *Ieee Transactions on Nuclear Science*, vol. 44, pp. 218-224, Apr 1997.
- [63] Y. Gu, G. Pratz, F. W. Y. Lau, and C. S. Levin, "Effects of multiple-interaction photon events in a high-resolution PET system that uses 3-D positioning detectors," *Medical Physics*, vol. 37, pp. 5494-5508, Oct 2010.
- [64] K. A. Comanor, P. R. G. Virador, and W. W. Moses, "Algorithms to identify detector Compton scatter in PET modules," *Ieee Transactions on Nuclear Science*, vol. 43, pp. 2213-2218, Aug 1996.
- [65] R. S. Miyaoka and T. K. Lewellen, "Effect of detector scatter on the decoding accuracy of a DOT detector module," *Ieee Transactions on Nuclear Science*, vol. 47, pp. 1614-1619, Aug 2000.
- [66] G. Pratz and C. S. Levin, "Bayesian reconstruction of photon interaction sequences for high-resolution PET detectors," *Physics in Medicine and Biology*, vol. 54, pp. 5073-5094, Sep 7 2009.

Chapter 2

System Development

NEMA NU-4 performance evaluation of PETbox4, a high sensitivity dedicated PET preclinical tomograph

Z Gu¹, R Taschereau¹, N T Vu², H Wang¹, D L Prout¹, R W Silverman¹,
B Bai³, D B Stout^{1,2}, M E Phelps^{1,2} and A F Chatzioannou^{1,2}

¹ Crump Institute for Molecular Imaging, David Geffen School of Medicine, University of California at Los Angeles, Los Angeles, CA, USA

² Sofie Biosciences, Culver City, California, USA

³ Keck School of Medicine, University of Southern California, Los Angeles, CA, USA

E-mail: zhgu@mednet.ucla.edu

Received 22 February 2013, in final form 5 April 2013


Published 10 May 2013

Online at stacks.iop.org/PMB/58/3791

Abstract

PETbox4 is a new, fully tomographic bench top PET scanner dedicated to high sensitivity and high resolution imaging of mice. This manuscript characterizes the performance of the prototype system using the National Electrical Manufacturers Association NU 4-2008 standards, including studies of sensitivity, spatial resolution, energy resolution, scatter fraction, count-rate performance and image quality. The PETbox4 performance is also compared with the performance of PETbox, a previous generation limited angle tomography system. PETbox4 consists of four opposing flat-panel type detectors arranged in a box-like geometry. Each panel is made by a 24×50 pixelated array of $1.82 \times 1.82 \times 7$ mm bismuth germanate scintillation crystals with a crystal pitch of 1.90 mm. Each of these scintillation arrays is coupled to two Hamamatsu H8500 photomultiplier tubes via a glass light guide. Volumetric images for a $45 \times 45 \times 95$ mm field of view (FOV) are reconstructed with a maximum likelihood expectation maximization algorithm incorporating a system model based on a parameterized detector response. With an energy window of 150–650 keV, the peak absolute sensitivity is approximately 18% at the center of FOV. The measured crystal energy resolution ranges from 13.5% to 48.3% full width at half maximum (FWHM), with a mean of 18.0%. The intrinsic detector spatial resolution is 1.5 mm FWHM in both transverse and axial directions. The reconstructed image spatial resolution for different locations in the FOV ranges from 1.32 to 1.93 mm, with an average of 1.46 mm. The peak noise equivalent count rate for the mouse-sized phantom is 35 keps for a total activity of 1.5 MBq (40 μ Ci) and the scatter fraction is 28%. The standard deviation in the uniform region of the image quality phantom is 5.7%. The recovery coefficients range from 0.10 to 0.93. In comparison to the first generation two panel PETbox system, PETbox4 achieves substantial improvements on sensitivity and spatial resolution. The overall

performance demonstrates that the PETbox4 scanner is suitable for producing high quality images for molecular imaging based biomedical research.

 Online supplementary data available from stacks.iop.org/PMB/58/3791/mmedia

(Some figures may appear in colour only in the online journal)

1. Introduction

Positron emission tomography (PET) is an imaging modality that enables non-invasive, *in vivo* detection and quantification of biological processes at the molecular level and has found wide applications in pharmacology, genetics, and pathology investigations (Phelps 2000, Gambhir 2002, Myers 2001, Chatziioannou 2002a). Since the 1990s, significant efforts in the development of small animal PET prototype scanners have pushed the limits of resolution and sensitivity with various approaches (Bloomfield *et al* 1995, Lecomte *et al* 1996, Cherry *et al* 1997, Chatziioannou *et al* 1999, Jeavons *et al* 1999, Weber *et al* 2000, Di Domenico *et al* 2003, Seidel *et al* 2003, Surti *et al* 2003, Tai *et al* 2003, Correia *et al* 2004, Rouze *et al* 2004, Miyaoka *et al* 2005, Schafers *et al* 2005, Ziemons *et al* 2005, Li *et al* 2007, Bergeron *et al* 2009, Lage *et al* 2009, Prasad *et al* 2010, Zhang *et al* 2011, Szanda *et al* 2011, Canadas *et al* 2011, Sanchez *et al* 2012). Commercial preclinical PET systems also became available from 2000 (Tai *et al* 2001, Knoess *et al* 2003, Tai *et al* 2005, Laforest *et al* 2007, Schafers *et al* 2005, Wang *et al* 2006, Huisman *et al* 2007, de Jong *et al* 2007, Bao *et al* 2009, Canadas *et al* 2011, Prasad *et al* 2010, 2011, Szanda *et al* 2011). The performance and capabilities of these systems evolved rapidly and have led to an increased use and acceptance of *in vivo* molecular imaging techniques in biological laboratories.

Advancements in molecular biology have made genetically modified mice the animal of choice to mimic human subjects for both healthy and diseased states (Paigen 1995). The mouse genome was the second mammalian genome to be fully sequenced after the human (Marshall 2001). The use of mouse models also has a relatively low cost of maintaining colonies due to the rapid reproduction and short normal life span of mice (Weissleder and Mahmood 2001). It is worthwhile to note that genetically modified mice represent more than 90% of the preclinical disease models in biological research (Malakoff 2000). The requirement to image in addition to mice, larger rodents such as rats, necessitates an enlarged imaging field of view (FOV), which leads to significantly larger detector surfaces, with tens of thousands of crystal elements and complicated electronics for most configurations, significantly increasing cost. Furthermore, the increased geometric detector separation leads to significant reduction to the system sensitivity, compromising performance. In this work, the design of the PETbox4 optimized specifically for imaging mice, with a useful FOV that can accommodate the vast majority of mice (18–40 g), therefore presents a compromise in the target subject size, in exchange for low cost and high sensitivity.

The volume and mass of mice are approximately 3000 times smaller than that of humans and 10–20 times smaller than an average rat. The spatial resolution of a PET scanner dedicated for mouse imaging should be similarly higher and the voxel size in the reconstructed images should also be reduced according to sampling theory (Chatziioannou 2002b). To obtain images of the same statistical quality as in humans, the number of counts detected per voxel, which is inversely proportional to voxel volume, could be compensated by either increasing the radioactivity of injected probes or by improving the sensitivity of the scanner. However, with a typical amount of radioactivity administered (7.4 MBq (200 μ Ci)) (Chatziioannou *et al* 1999), the concentration of radionuclides in mice is already much higher than that in

humans. It has been shown that during preclinical PET imaging procedures, major organs like the bladder, brain, heart, and tumor xenografts of mice could receive an absorbed dose in a range for which biological effects such as stimulated cell proliferation (Wang and Cai 2000), induced radio-resistance (Yonezawa 2006), elevated gene expression (Amundson *et al* 2001), have been reported (Taschereau and Chatziioannou 2007, Funk *et al* 2004). Those biological effects may interfere and bias the results in pharmaceutical and genetic studies, leading to discrepancies on translational research between mouse models and clinical applications. Also, for many applications such as neuroreceptor imaging, the signal of concern can be inherently limited by the number of binding sites available, as well as by the specificity and affinity of the radiotracers (Hume *et al* 1998). The injected probe mass, which should be below levels that perturb the studied biological system, may limit the amount of radioactivity that can be injected into a mouse to the range of 0.37–3.7 MBq (10–100 μ Ci) (Hume *et al* 1998). High sensitivity imaging systems are therefore desirable to obtain count statistics adequate per volumetric resolution element with lower amounts of radioactivity and reduce radiation dose delivered to mice. This is especially important in the case of longitudinal studies, in which multiple experiments take place over a period of time. In addition, high sensitivity also contributes to higher imaging throughput, by maintaining optimized imaging performance within the required scan time, which is especially important when imaging a considerable number of subjects in one study (Gagnon *et al* 2009).

Combining these considerations, PETbox4, a bench top PET scanner dedicated to high sensitivity and high resolution imaging of mice, was recently designed and built at our institute. PETbox4 is configured using a close geometry of flat panel detectors to provide large solid angle coverage. The addition of a multiplexing scheme for each detector head allows for a low number of required electronic channels to be readout. These parameters provide a system with high performance, low cost and reduced complexity. For typical biodistribution studies in this system, we anticipate an administered radioactivity amount of less than 1.5 MBq (40 μ Ci), which is five times lower than established procedures. PETbox4 is the second generation of the previous prototype PETbox system developed by our group (Zhang *et al* 2011, Zhang *et al* 2010) and presents a significant improvement on sensitivity and spatial resolution. This work aims to characterize the overall performance of the PETbox4 system using the National Electrical Manufacturers Association (NEMA) NU 4-2008 standards wherever possible. The NEMA NU-4 standards offer a consistent and standardized methodology for small animal PET performance assessment, including sensitivity, spatial resolution, scatter fraction (SF), count rate performance and image quality characteristics. Additional measurements were also performed: energy resolution and intrinsic detector spatial resolution. The overall imaging capabilities of the scanner and its suitability for high-sensitivity high-resolution molecular imaging were also demonstrated through *in-vivo* rodent studies.

2. Materials and methods

2.1. System description

PETbox4 employs four opposing panel detectors placed at a spacing of 5 cm, arranged in a compact, box-like geometry (figure 1(a)). The effective area of each scintillator array is 45.58×95.05 mm, large enough to cover the whole body of the vast majority of laboratory mice (18–40 g). For the scintillator material of the detectors, bismuth germanate (BGO) was chosen. This scintillator has a high effective atomic number ($Z = 83$) which increases the probability of a photoelectric event at the first interaction site and reduces inter-crystal scatter, leading to more accurate event positioning and higher spatial resolution. BGO also has an

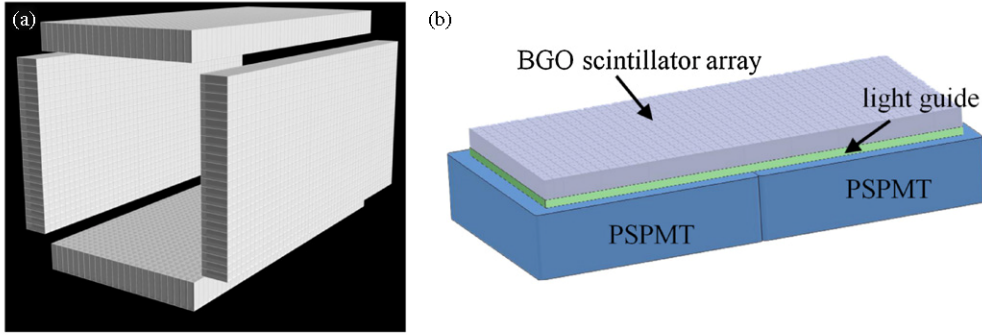


Figure 1. (a) PETbox4 system detector configuration. Four detectors are arranged in a box-like geometry, with a spacing of 5 cm between opposing detector panels. (b) Schematic drawing of a PETbox4 detector module. The complete detector module employs two H8500 PMTs to detect scintillation light from a 24×50 BGO crystal array.

overall stopping power for 511 keV photons comparable to that of lutetium oxyorthosilicate (LSO). In previous work, we have shown that a BGO based scanner has higher system sensitivity and lower SF than the equivalent LSO based scanner (Bao and Chatziioannou 2007). To achieve equivalent sensitivity, a BGO system requires lower detector thickness, leading to reduced parallax errors and better spatial resolution. Additionally, BGO has about 35 times lower intrinsic radioactivity compared with LSO (de Marcellac *et al* 2003). Therefore, the system background will not adversely affect the system minimum detectable activity (MDA) (Goertzen *et al* 2007, Bao and Chatziioannou 2010), especially when considering a very compact geometry and the intended use of the system at low activity levels. Each panel detector of the PETbox4 is comprised of a 24×50 pixelated BGO scintillator array with individual crystals measuring $1.82 \times 1.82 \times 7$ mm (± 0.05 mm) and a pitch of 1.90 mm (Proteus, Chagrin Falls, OH). The individual pixels are cut but not optically polished, and are separated by VM2000 a specular optical reflector (3M, St Paul, MN), generating optical properties that are a mixture of specular and diffuse reflection. The entire array is permanently coupled with a polymer silicon material to two H8500 multi-channel position-sensitive photomultiplier tubes (PSPMT; Hamamatsu Photonics, Bridgewater, NJ) via a glass light guide (figure 1(b)). The read-out electronics of each detector are integrated in a compact printed circuit board stack directly attached to the PMT sockets. A charge-division readout circuit is used to convert the anode outputs from the two PSPMTs into position encoding signals, while the timing signal is obtained directly from the 12th dynode signal on the H8500 PSPMTs. The four detector modules and the associated readout circuitry are encased in an aluminum housing and mounted on a frame.

Position and timing signals from the readout circuitry of the four panel detectors are digitized by sixteen 104 MHz free running analogue-to-digital converters (ADC) on an FPGA-based signal processing card (VHS-ADC, Lyrtech Signal Processing, Quebec City, Quebec). The digital samples are then processed in a Xilinx Virtex-4 field programmable gate array (Xilinx, San Jose, CA) in real time, including pulse shaping, event triggering, event qualification and coincidence detection. The 128 MB synchronous dynamic random access memory (SDRAM) on the VHS-ADC board stores look-up tables (LUT) that are applied to the digitized energy and position data for online identification of the crystal of interaction and for energy discrimination. A delayed window method is also implemented in the FPGA to estimate random coincidence event rates. A compactPCI CPU card (cPCI-6965, ADLINK, San

Table 1. Characteristics of the PETbox and the PETbox4 system.

		PETbox	PETbox4
Detector	Crystal material	BGO	BGO
	Crystal size	$2 \times 2 \times 5 \text{ mm}^3$	$1.82 \times 1.82 \times 7 \text{ mm}^3$
	Crystal pitch	2.2 mm	1.90 mm
	Packing fraction	0.83	0.92
	Crystal Array	20×44 crystals/PMT	24×50 crystals/PMT
	PMTs	Hamamatsu H8500 PSPMT	Hamamatsu H8500 PSPMT
	Reflector between crystals	NA	VM2000
System	Number of detectors	2	4
	Number of crystals	1760	4800
	Axial FOV	96.8 mm	95 mm
	Transaxial FOV	44 mm	45 mm

Jose, CA) is used to control the FPGA logic on the VHS-ADC card, to receive the generated 32-Bit list-mode data stream and to save the data to an external hard disk.

For the work described here, all measurements were acquired with a coincidence timing window of 20 ns, and the acquired list-mode data were histogrammed into sinograms with delayed events subtracted to correct for random coincidences. Unless explicitly stated otherwise, all list-mode data measurements were acquired with an energy window of 150–650 keV, which is the default operating window for imaging with the PETbox4. The notable exception to this was the sensitivity measurement, for which the lower energy was varied, to show the influence of energy window on system sensitivity.

Component-based normalization (Mumcuoglu *et al* 1994) was applied to compensate for the differences in individual detector efficiencies, estimated from measurements of a cylindrical source filled with ^{18}F . Fully 3D tomographic images were reconstructed by a maximum likelihood and expectation maximization (ML-EM) algorithm with the incorporation of a system model based on a parameterized detector response (Taschereau *et al* 2011). For all studies in this paper, 60 iterations were used for the reconstruction of image data with no regularization. The resulting image matrix consisted of $96 \times 96 \times 200$ voxel bins with a cubic voxel of $0.476 \times 0.476 \times 0.476 \text{ mm}^3$, forming an entire reconstructed FOV of $45 \times 45 \times 95 \text{ mm}^3$. Table 1 summarizes the geometric and physical characteristics of the PETbox4 and the first generation PETbox system.

The PETbox4 is integrated with a Mouse Atlas Registration System (MARS) which provides a novel anatomical reference approach via a combination of x-ray projection, optical photographic images and a digital mouse atlas (Wang *et al* 2011, Wang *et al* 2012). The MARS consists of a miniature x-ray tube (MAGNUM[®] 40 kV x-ray source, Moxtek Inc., UT, USA), an x-ray detector (RedEyeTM200 Remote Sensor, Rad-Icon Imaging Corp. CA, USA) and a webcam (Firefly[®] MV, Point Grey Research Inc., BC, Canada). The complete PETbox4/MARS system retains a small overall footprint, as shown in figure 2.

2.2. Energy resolution and flood histograms

A 0.106 MBq ^{68}Ge (2.86 μCi) cylinder source (Eckert & Ziegler Isotope Products, Valencia, CA) with a diameter of 32 mm and 67 mm length was placed at the center of the field of view (CFOV) of the system to acquire a two-dimensional flood image for each detector, for singles events. Boundaries were determined using a semi-automated program to define the crystal LUT that classify regions in the flood image into the proper crystal of the BGO array. For this acquisition, specialized software was utilized on the system electronics, recording

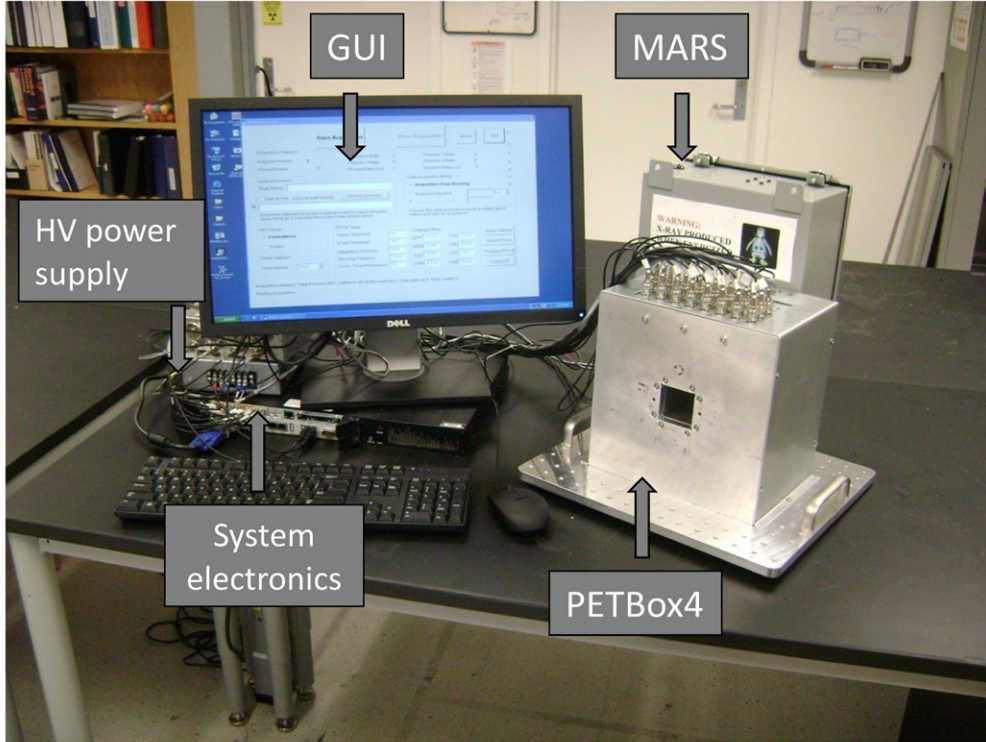


Figure 2. A photograph of the entire PETbox4 system, including the MARS, the data acquisition electronics and the controlling computer.

the energy of each event into the list-mode data. Energy spectra of individual crystals were extracted based on the LUTs and a Gaussian function was fitted to the photopeak of each energy spectra. Energy resolution was measured for every crystal in the scanner as the full width at half-maximum (FWHM) of the Gaussian function divided by the energy corresponding to the center of the photopeak, expressed as a percentage resolution.

2.3. Spatial resolution

A 1.05 MBq (28.3 μCi) ^{22}Na point source with a nominal size of 0.3 mm, embedded in a 1 cm³ piece of acrylic was used (NEMA NU4 compliant, Eckert & Ziegler Isotope Products, Valencia, CA). The system was configured to acquire data in coincidence mode. Measurements were not corrected for the point source dimensions, positron range, or the non-collinearity of positron annihilation.

2.3.1. Intrinsic spatial resolution. Starting from the center of the FOV, the point source was attached to a translation stage and stepped at 0.4 mm steps across the mid line of two opposing panel detectors along the long axis of the system. An assumption was made that the detector coincidence pair configuration is symmetric and therefore measurements were performed for only half of the detector axial FOV. Due to geometric restriction by the two side detectors, the point source could not be stepped across half of the detector along the short axis. Instead, the source was stepped across the central 14 crystals in the central axial plane. The acquisition

time was 30 s at each location. The coincidence counts for directly opposing crystal pairs were plotted as a function of source location. The count distribution of each crystal pair was fitted with a Gaussian function and the FWHM was calculated to determine the intrinsic spatial resolution of the detectors.

2.3.2. Image spatial resolution. The point source was imaged at two axial locations: (a) the center of the axial FOV and (b) one fourth of the axial FOV, 23.5 mm from the center along the axial direction. For each of these two axial locations, the source was stepped in 5 mm increments toward the edge of the transverse FOV at the following radial distances from the geometric center: 0 mm, 5 mm, 10 mm, 15 mm and 20 mm. Acquisition time was 1 min at each position and more than 10^5 prompt counts were acquired per measurement. The NEMA NU-4 document also recommends a measurement at 25 mm from the center, which was out of the transaxial FOV of the PETbox4 and is therefore not included in this study.

The list-mode data acquired at each position were histogrammed into sinograms with delayed events subtracted to correct for random coincidences and with a normalization to compensate for the differences in individual detector efficiencies. The images were reconstructed using the ML-EM algorithm. As specified in the NEMA NU-4 2008 protocol, the response function was formed by summing one-dimensional profiles that were parallel to the radial, tangential, and axial directions. A parabolic fit of the peak point and its two nearest neighboring points was used to determine the maximum value of the response function. Linear interpolation between adjacent pixels was used to determine the position of the half and one tenth of the parabolic curve maximum. The volumetric resolution was calculated on the basis of the FWHMs of the radial, tangential, and axial directions. While the NEMA NU-4 standards indicate that filtered back projection (FBP) should be used for the spatial resolution measurements, this was not possible here, since a FBP algorithm specific for the PETbox4 system with the unconventional geometry has not been developed. The main reason behind this is that the spatial sampling of the lines of response in the projection data, especially in the angular direction is highly non uniform due to the flat panel detector in close proximity geometry. As a result, the interpolations necessary for resampling the data (including the estimated average DOI), would require a hybrid reconstruction based in part on Monte Carlo simulations, in combination with methods to fill in the missing data due to the gaps between the detector heads. Such a data reconstruction would also not comply with the NEMA NU-4 protocol and would be a unique feature to the particular geometry of PETbox4.

2.3.3. Sensitivity. Sensitivity is expressed as the fraction of the actual positron annihilation events that are detected as true coincidence events. A ^{68}Ge point-like source (Eckert & Ziegler Isotope Products, Valencia, CA) embedded in thin steel tubing was placed at the CFOV to measure the peak absolute sensitivity. The thin steel casing ensures annihilation of all the positrons, but does not cause significant attenuation of the 511 keV gamma rays. The activity of the point source was 21 kBq ($0.56 \mu\text{Ci}$) measured in a calibrated well-type gamma counter (Wallac Wizard 1480, Perkin Elmer, Shelton, CT). The activity was low enough so that the counting losses were less than one per cent and the randoms rate was less than 5% of the true event rate, fulfilling the NEMA NU 4-2008 protocol recommendations.

To investigate the sensitivity dependence on the energy threshold, the system peak absolute sensitivity measurements were acquired at the center of the FOV with a fixed upper-level discriminator (ULD) corresponding to 650 keV and a lower-level discriminator (LLD) corresponding to energies from 150 to 350 keV, in 50 keV steps. The axial sensitivity profile was measured with the same source stepped across the scanner from end to end of the axial FOV,

with an energy window of 150–650 keV. The axial positions of the source were determined from the reconstructed images. The number of coincidences was recorded at each acquisition for 30 s. Delayed coincidences were subtracted from prompts before the true coincidences were divided by the actual source activity. This ratio was corrected for the branching ratio of ^{68}Ga (0.89), but the attenuation of the steel material surrounding the source was not compensated. The peak absolute sensitivity measurements were compared with simulated values obtained from GATE (Geant4 Application for Tomographic Emission) (Jan *et al* 2004) simulations with the same configurations. The average sensitivity for a mouse-sized object (with a 7 cm axial length) was calculated from the measured axial sensitivity profile.

2.4. Scatter and count-rate performance

Count-rate performance was evaluated using the NEMA NU-4 mouse-sized phantom, which is a 70 mm long and 25 mm diameter solid cylinder made of high density polyethylene (0.96 g/cm^3), with a 3.2 mm diameter hole drilled parallel to the central axis at a radial offset of 10 mm. A flexible tube filled with ^{18}F solution was inserted into the 3.2 mm hole of the phantom. The initial activity was measured to be 2.52 MBq ($68.2 \mu\text{Ci}$) using a dose calibrator (Atomlab 300; Biodex Medical Systems, Shirley, NY) at the start of the acquisition. The phantom was centered in the FOV and rotated by 45° in order to achieve a more symmetric source distribution that is also a closer representation of the expected typical spatial distribution in mouse studies. An imaging chamber supporting the phantom was included in the FOV for this measurement, creating a realistic scatter environment. Data were acquired until the total activity decayed below 10 kBq, while random coincidences were measured using the delayed window method.

The data was processed as specified by NEMA NU-4, briefly described here: In the prompts sinogram, the profile of direct projections from opposite crystals was shifted so that the peak pixels were aligned with the center pixel of the sinogram. A sum projection was produced by adding up all projections in each slice. All pixel counts outside of a 14-mm centered band were assumed to be due to the random and scatter counts. A linear interpolation between the left and right border of the 14 mm band was used to estimate these non-true counts under the profile peak. Counts above this line were taken as true events, while randoms were estimated from the delayed sinogram.

The SF was measured using a prompt sinogram with an activity of 74 kBq ($2 \mu\text{Ci}$). This low activity frame was chosen to ensure that dead time and randoms did not affect the measurement. The scattered count rate was then calculated by equation (1):

$$R_{\text{scatter}} = R_{\text{prompt}} - R_{\text{true}} - R_{\text{random}}, \quad (1)$$

where R_{scatter} , R_{prompt} , R_{true} and R_{random} are the scatter, prompt, true and random event rates, respectively. The SF was calculated by equation (2):

$$\text{SF} = \frac{R_{\text{scatter}}}{R_{\text{scatter}} + R_{\text{true}}}, \quad (2)$$

The noise equivalent count rate (NECR) for each prompt sinogram was determined using the following equation:

$$\text{NECR} = \frac{R_{\text{true}}^2}{R_{\text{prompt}} + R_{\text{random}}} = \frac{(R_{\text{prompt}} - R_{\text{random}})^2 \times (1 - \text{SF})^2}{R_{\text{prompt}} + R_{\text{random}}} \quad (3)$$

2.5. Imaging studies

2.5.1. NEMA phantom study. Image quality studies were performed using the image quality phantom described in the NEMA NU-4 protocol. The phantom (Data Spectrum Corporation, Hillsborough, NC) consists of the following three regions: a main fillable uniform region chamber allowing the uniformity to be measured; a lid that attaches to the main fillable region, containing two smaller cold region chambers (filled with water and air) that are used to quantify the spillover ratio (SOR); and a solid acrylic glass region with five fillable rods drilled through for measuring the recovery coefficients (RCs) as a function of rod diameter. Since the PETbox4 is intended to be used with a low injection dose, the image-quality phantom was filled with 1.85 MBq (50 μ Ci) ^{18}F solution measured with a dose calibrator (Atomlab 300; Biodex Medical Systems, Shirley, NY). It should be pointed out that this activity is half the activity level recommended by the NEMA NU-4 protocol. The phantom was placed on a mouse imaging chamber to simulate actual mouse imaging and was imaged for 20 min, following the NEMA NU-4 recommendations. Normalization and random corrections were applied, but no scatter correction was applied. For attenuation correction applied in this manuscript, a CT transmission scan of the object and its supporting bed was obtained using a MicroCAT II tomograph (Siemens Preclinical Solutions, Knoxville, TN). The reconstructed CT image was registered with the PET emission image and forward projected through the system response matrix to create an attenuation sinogram. The image was reconstructed by the ML-EM algorithm.

A 22.5-mm-diameter and 10-mm-high cylindrical volume of interest (VOI) was drawn over the center of the uniform region of the image-quality phantom. The average concentration values in this VOI, and standard deviation (SD) were measured to estimate the noise performance as a measure of uniformity. The image slices covering the central 10 mm length of the rods were averaged to obtain a single image slice of lower noise. Circular regions of interest (ROIs) were drawn in this image around each rod, with diameters twice the physical diameters of the rods. The maximum values in each of these ROIs were measured and divided by the mean value obtained in the uniformity test to obtain the RC for each rod size. The transverse image pixel coordinates of the locations with the maximum ROI values were recorded and used to create 10 mm long line profiles along the rods in the axial direction. The SD of the pixel values measured along each line profile was calculated. Although no scatter correction was applied to the acquired dataset, the SOR of the water- and air-filled cold region chamber were calculated as specified in the NEMA NU-4 standard to provide a rough estimation of the scatter effects. The diameter of the VOI was 4 mm and encompassed the central 7.5 mm in length in the axial direction. The ratio of the mean in each cold region to the mean of the hot uniform area was reported as SOR.

2.5.2. Mouse study. A dynamic [^{18}F]-FDG study was performed on a healthy mouse to demonstrate the dynamic imaging capabilities of the PETbox4 system. The mouse was anesthetized with isoflurane, positioned in the imaging chamber, and placed in the PETbox4 system. At the beginning of a tail injection of 1.59 MBq (43 μ Ci) [^{18}F]-FDG, a 1 h list-mode file data acquisition was initiated. The data was sliced into 10 time frames, with lengths of 2, 2, 6, 50, 540, 600, 600, 600, 600 and 600 s. For each frame, volumetric images were reconstructed using the ML-EM method. Normalization and attenuation correction were applied, but no scatter correction was applied. VOIs were manually drawn for the bladder, heart and kidney in the reconstructed images. The mean image value in each VOI was calculated as a representation of the activity distribution in that organ. To validate system performance with isotopes other than ^{18}F , a static study with an antibody fragment radiolabeled with ^{64}Cu was performed. A

Table 2. Energy resolution of the four detector panels in the PETbox4 system.

Detector	Mean	Max	Min
0	19.76	42.25	15.54
1	17.48	48.31	13.81
2	16.91	32.39	13.53
3	17.41	35.96	13.89
Overall	17.89	48.31	13.53

healthy mouse was injected with ^{64}Cu radiolabeled minibody and after an uptake of 4 h, the mouse was scanned for 20 min. The activity was 0.14 MBq ($3.7 \mu\text{Ci}$) in the entire mouse at scan time. To demonstrate the imaging capabilities of the PETbox4/MARS system, MARS scans were performed after the PET acquisition. The x-ray source configuration was set at 40 kVp, $100 \mu\text{A}$, and 3 s exposure. The camera exposure time for the optical photographic image was set to 200 ms.

3. Results

3.1. Energy resolution and flood histograms

Figure 3(a) shows the flood histogram taken from one of the detector panels. In the flood histograms from the four detectors, more than 95% of the individual crystal elements in the 24×50 array are clearly identified. Table 2 summarizes the measured energy resolution for the four detector panels. For the crystals in the four panels, the measured crystal energy resolution ranged from 14% to 48% FWHM, with a mean of 18%. Figure 3(b) shows a vertical profile across one column of crystals in the flood histogram, and figure 3(c) shows a horizontal profile across one row. Although the edge crystals are not very well resolved, most of the other crystals have a good peak to valley separation (average 3.55). Figure 4 shows the non-uniformity of the energy resolution across all crystals in one detector panel and representative energy spectra of two individual crystals at different locations of the detector. It was observed that crystals at the center of each PSPMT tend to yield better energy resolution than edge crystals or crystals at the junction of the two PSPMTs.

In contrast, the prototype PETbox had an average energy resolution of 20%, despite the lower aspect ratio of its individual crystal elements. The improvement of the energy resolution is believed to be largely the result of the high quality reflector film around each pixel in the PETbox4 detector module resulting in better light collection efficiency. The detector blocks on the PETbox were left as cut, without any reflector between the individual pixels. Also, the addition of reflector between the individual pixels helps to reduce the light spread in the PMT, leading to the collection of light from a smaller and more uniform area of the PMT photocathode, potentially leading to improved energy resolution.

3.2. Spatial resolution

3.2.1. Intrinsic spatial resolution. The intrinsic spatial resolution of an opposing detector pair is shown in figure 5. For crystal pairs along the detector short axis, the measured FWHM ranged from 1.40 mm to 1.67 mm, with an average value of 1.51 mm. For crystal pairs along the detector long axis, the measured FWHM ranged from 1.34 mm to 1.64 mm, with an average value of 1.49 mm. In contrast, the previous prototype PETbox had an intrinsic spatial resolution ranging from 1.48 to 2.39 mm, with an average of 1.78 mm.

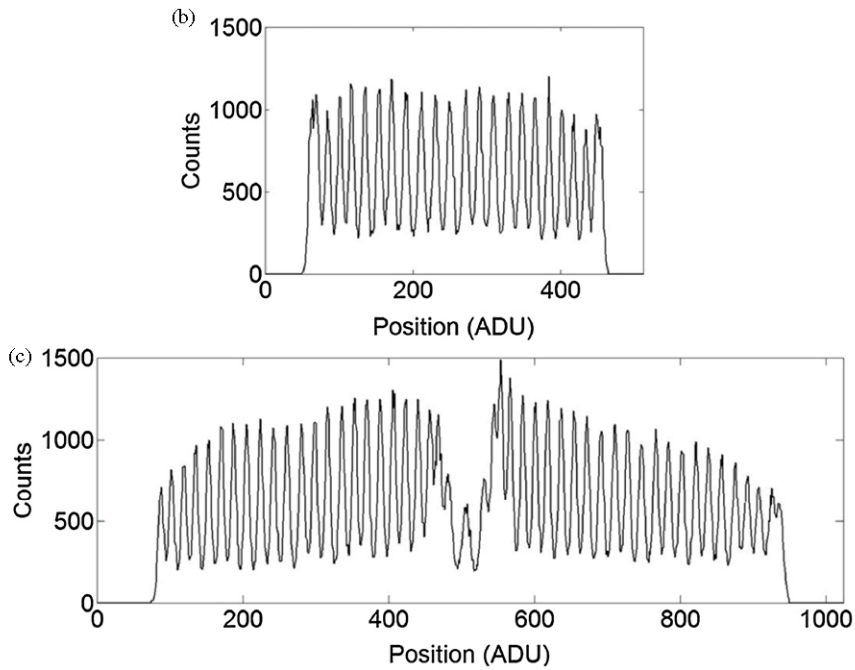
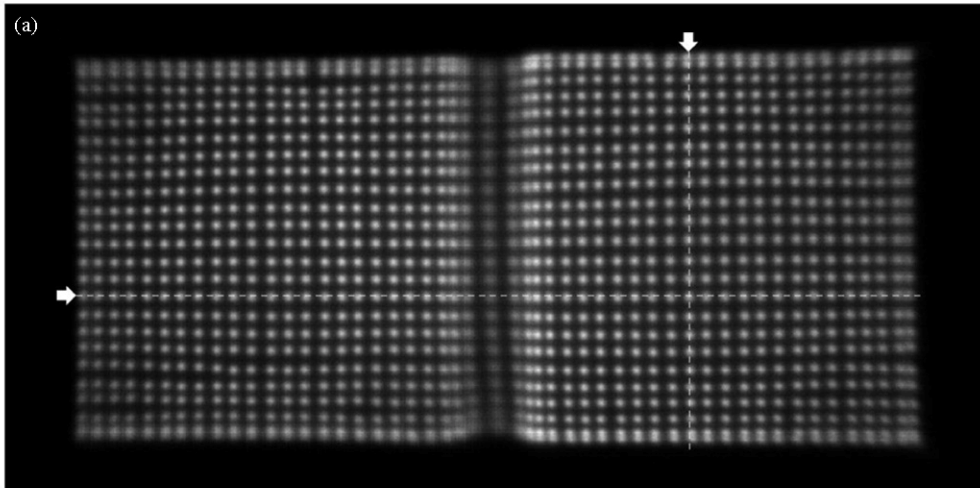


Figure 3. (a) Flood image taken from one of the four detector panels; (b) vertical profile across one column of the flood histogram; (c) horizontal profile across one row of the flood histogram.

3.2.2. Image spatial resolution. Figures 6(a) and (b) show the image spatial resolution in the radial, tangential, and axial directions measured in the central and 1/4 axial transverse plane in compliance with the NEMA NU-4 standard, respectively. The resolution in each of three orthogonal directions is below 2 mm FWHM and rather uniform, with an isotropic mean value of 1.5 mm FWHM.

The volumetric resolution, defined as the product of all three image resolution components of a system, is shown in figure 6(c) and compared with that of the prototype PETbox. The

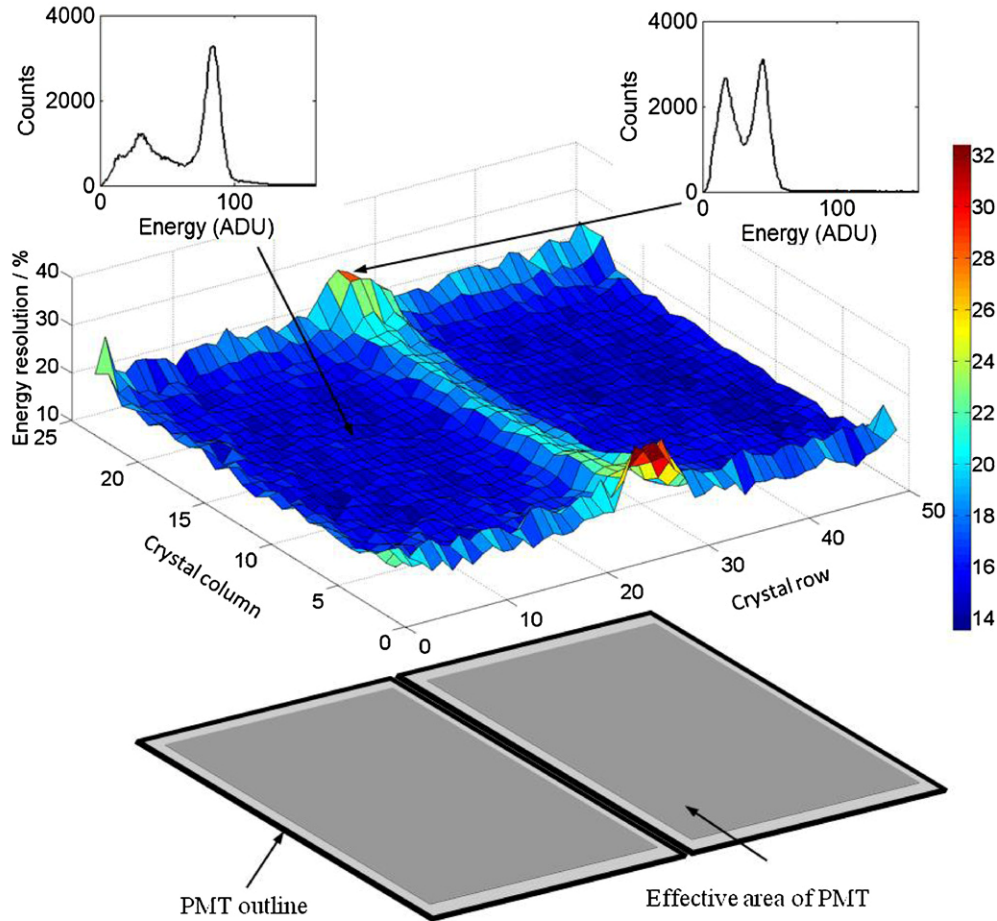


Figure 4. Position dependent energy resolution for one of the detector panels, superimposed on a map of the active areas of the two PSPMTs that make the detector panel. The measured energy spectra for two representative crystals at the center and at the edge of the detector panel are shown here.

improvement of the PETbox4 over the PETbox ranges from 1.2-fold at the CFOV ($3.4 \mu\text{L}$ versus $4.1 \mu\text{L}$) to 2.6-fold at 1.5 cm radial offset ($2.6 \mu\text{L}$ versus $6.7 \mu\text{L}$). At a 23.5-mm axial offset, the improvement ranges from 2-fold at the center of the transverse plane ($2.7 \mu\text{L}$ versus $5.3 \mu\text{L}$) to 2.1-fold at 1.5 cm radial offset ($3.6 \mu\text{L}$ versus $7.4 \mu\text{L}$).

3.3. Sensitivity

Figure 7 summarizes the peak system sensitivity at the CFOV for different energy window settings. As the energy window changes from 350–650 keV to 150–650 keV, the peak system sensitivity varies from 9.3% to 18.1%. With the default energy window of 150–650 keV, the PETbox4 has a peak system sensitivity of 18.1%, a fourfold improvement over the prototype PETbox at the same energy window. The measurements were in close agreement with the sensitivity estimated with the GATE simulation. The axial sensitivity profile is shown

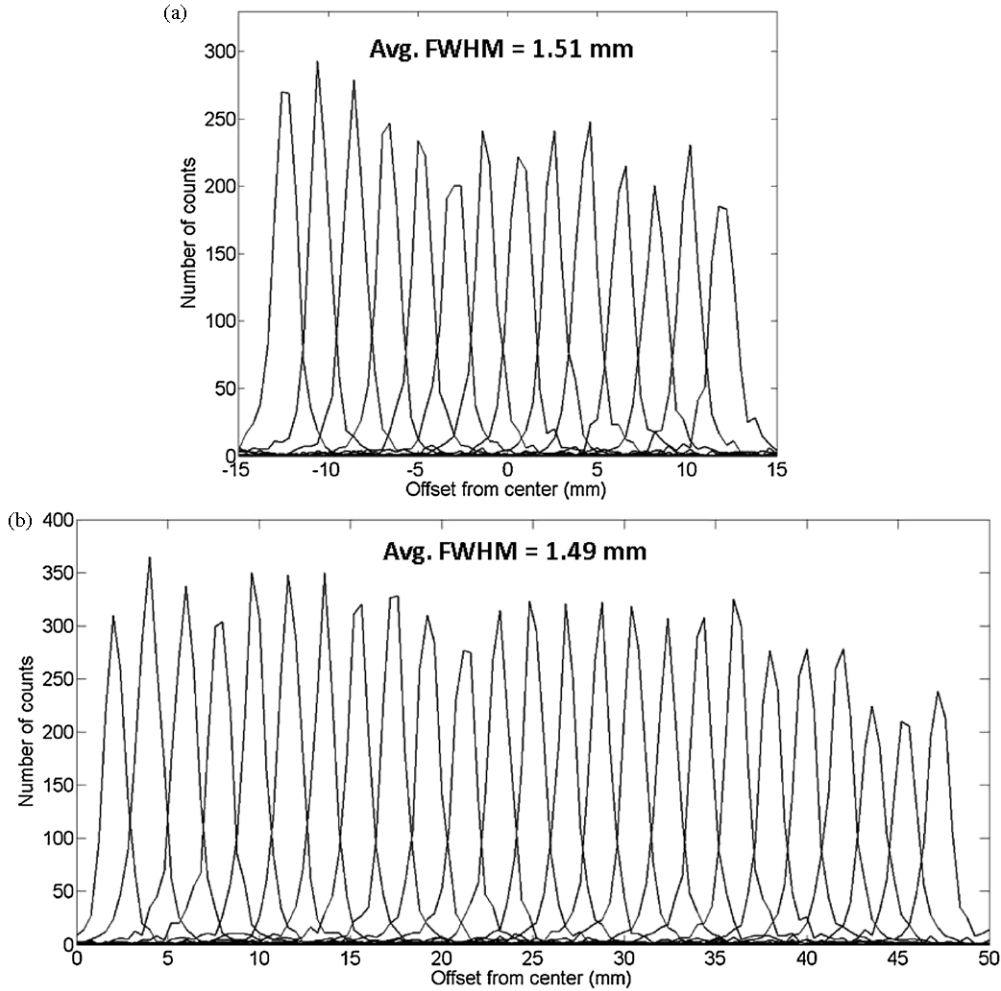


Figure 5. Intrinsic spatial resolution measured with a ^{22}Na point source in the direction (a) along the detector short axis and (b) along the detector long axis.

in figure 8. The PETbox4 system employs a closely packed geometry which leads to an increased fraction of backscatter events included in the coincidence timing window, therefore the sensitivity did not immediately decrease to zero when the source was stepped out of the axial FOV. The average sensitivity for a mouse-sized object (7 cm axial length) is 14% with an energy window of 150–650 keV.

3.4. Scatter and count-rate performance

Figure 9(a) illustrates the experimental setup for the count rate performance measurement. The phantom was centered in the FOV and rotated by 45° . The prompt, random and NEC rates as a function of total activity in the mouse-sized phantom are plotted in figure 9(b). With the default energy window of 150–650 keV and timing window of 20 ns, the prompt rates reach peak values at around 1.7 MBq (45 μCi) total activity. With this activity, the random

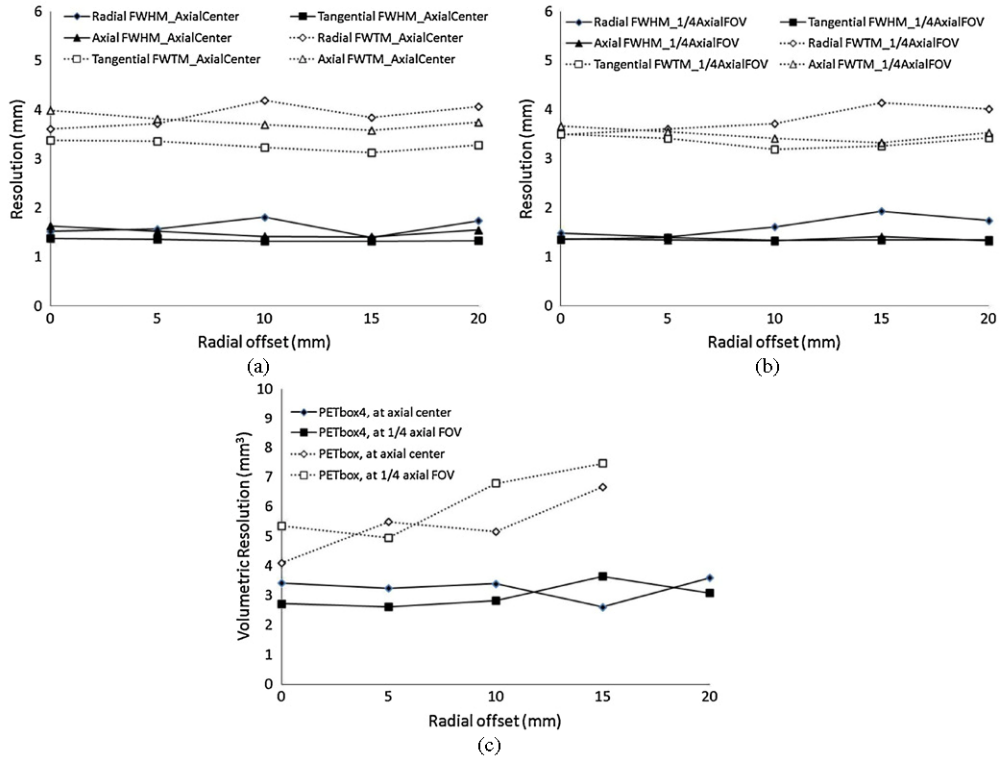


Figure 6. ML-EM reconstructed image spatial resolution of the PETbox4 system plotted per the modified NEMA NU-4 protocol, showing the FWHM and FWTM of the radial, tangential, and axial image resolutions at (a) axial center of the FOV and (b) 23.5 mm from the axial center toward the axial edge of the FOV. (c) The volumetric resolution of the PETbox4 compared with the PETbox.

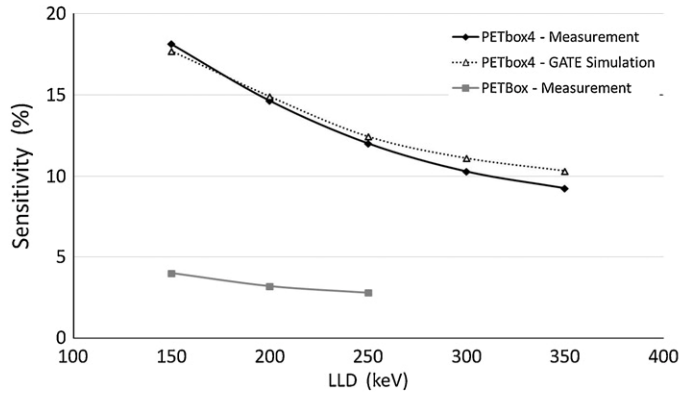


Figure 7. Absolute peak system sensitivity as a function of LLD for the PETbox4, the PETbox and the GATE simulation.

events account for approximately 3% of the total prompt counts. The PETbox4 system has a coincidence timing resolution of 4 ns FWHM, but since the random rate is low, a large timing window of 20 ns is used to increase the system sensitivity. This way, a number of prompt events

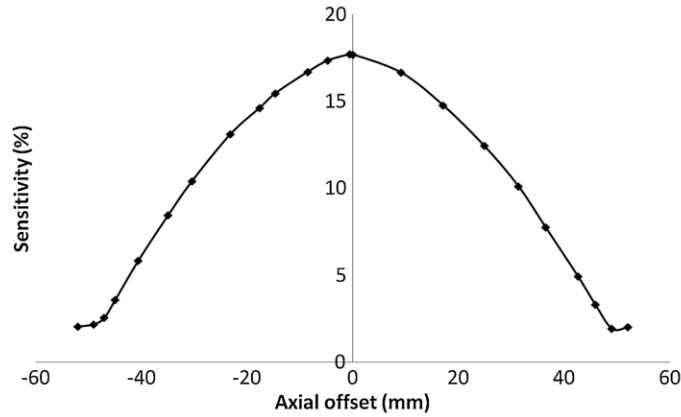


Figure 8. PETbox4 sensitivity profile as a function of axial position. The energy window was 150–650 keV.

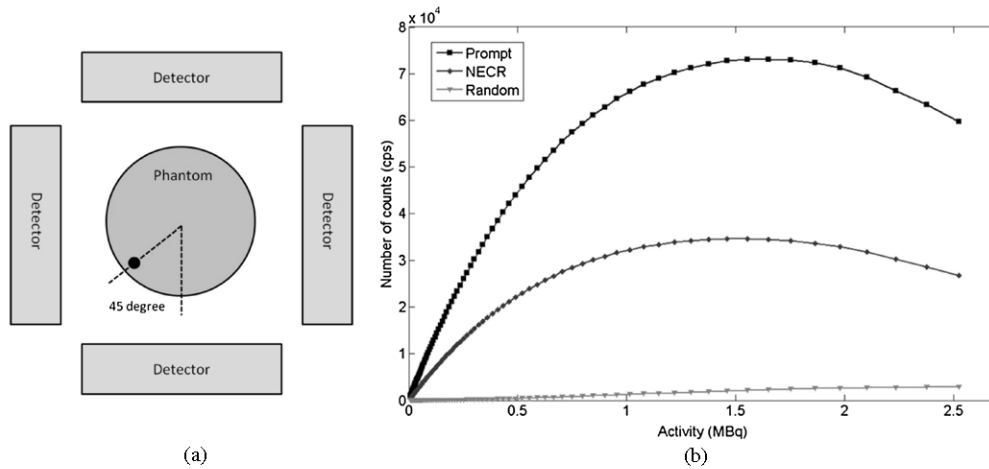


Figure 9. (a) Schematic drawing of the experimental setup for the count rate performance measurement. The phantom was centered in the FOV and rotated by 45°. (b) Count rate capability of the PETbox4 system as a function of the line source activity. Energy window was set at 150–650 keV.

that fall on the coincidence spectrum tails are accepted, and this done for all the measurements presented in this report. The peak NECR is 35 kcps achieved at a total activity of 1.5 MBq (40 μ Ci) in the phantom. The SF at this acquisition setting is 28%, which is mainly due to the bed support, the gantry material around the detectors, as well as the detector material itself.

3.5. Imaging studies

3.5.1. Phantom studies. Figure 10 shows the images of a transverse plane of the uniform region (figure 10(a)), a transverse plane with five rods (figure 10(b)), a coronal plane (figure 10(c)), and a profile across the uniform area (figure 10(d)) of the NEMA NU-4 image-quality phantom. With the ML-EM reconstruction, the SD in the uniform region was

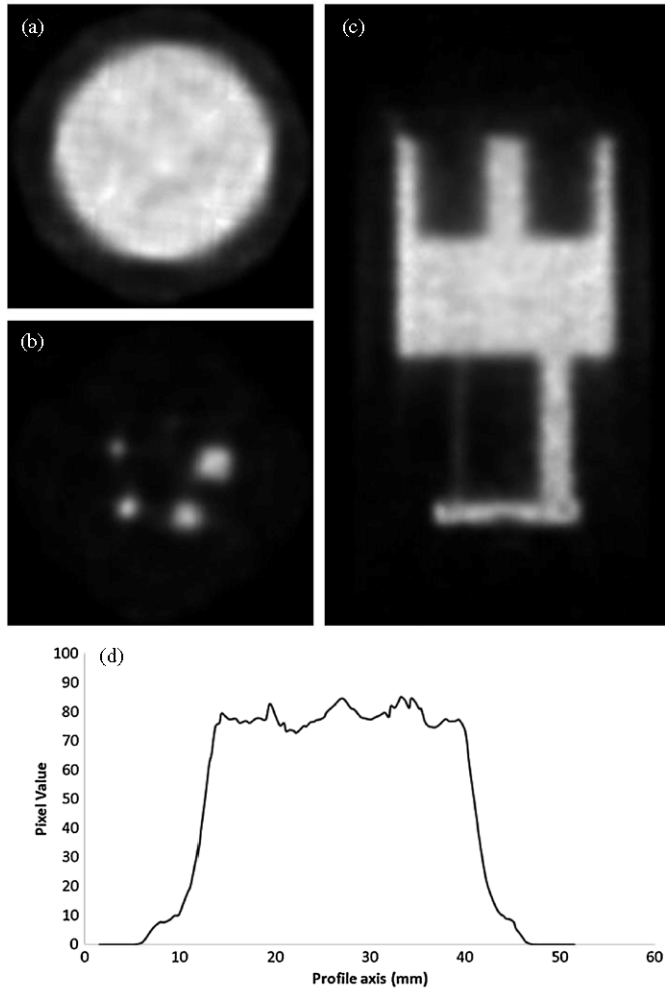


Figure 10. Image reconstruction of the NEMA NU-4 image quality phantom scanned for 20 min with ^{18}F (1.85 MBq). (a) A transverse slice of the uniform region; (b) a transverse slice of the rods region; (c) a coronal slice; (d) a profile across the uniform area.

5.7%. The RCs for five different rod sizes from 1 to 5 mm diameter are shown in figure 11. The RC for the smallest 1 mm rod is 0.10, and for the largest 5 mm rod the RC is 0.87. The RCs measured in the first generation PETbox system (Zhang *et al* 2011) are also shown in figure 11 for comparison.

The SOR measured in the water- and air-filled cold region chamber were calculated to be 14.7% and 13.3%, respectively. Since no scatter correction was applied for the acquired dataset, the SOR are indicative of the effect of scattered radiation on the reconstructed images.

3.5.2. In vivo mouse studies. Figure 12 shows selected reconstructed average intensity projection (AIP) images from eight frames corresponding to the time period: (a) 0–2 s, (b) 2–4 s, (c) 4–10 s, (d) 10–60 s, (e) 1–10 min, (f) 10–20 min, (g) 20–30 min, and (h) 50–60 min following the injection in the dynamic [^{18}F]-FDG study. The reconstructed images

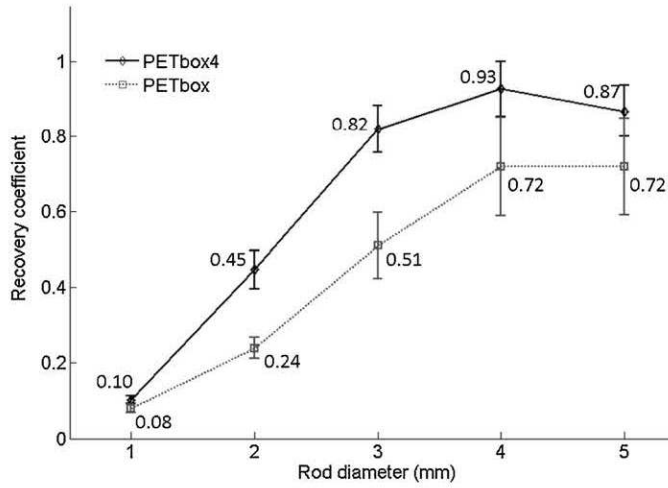


Figure 11. RCs and SDs for five rods of different sizes for the PETbox4 and PETbox systems.

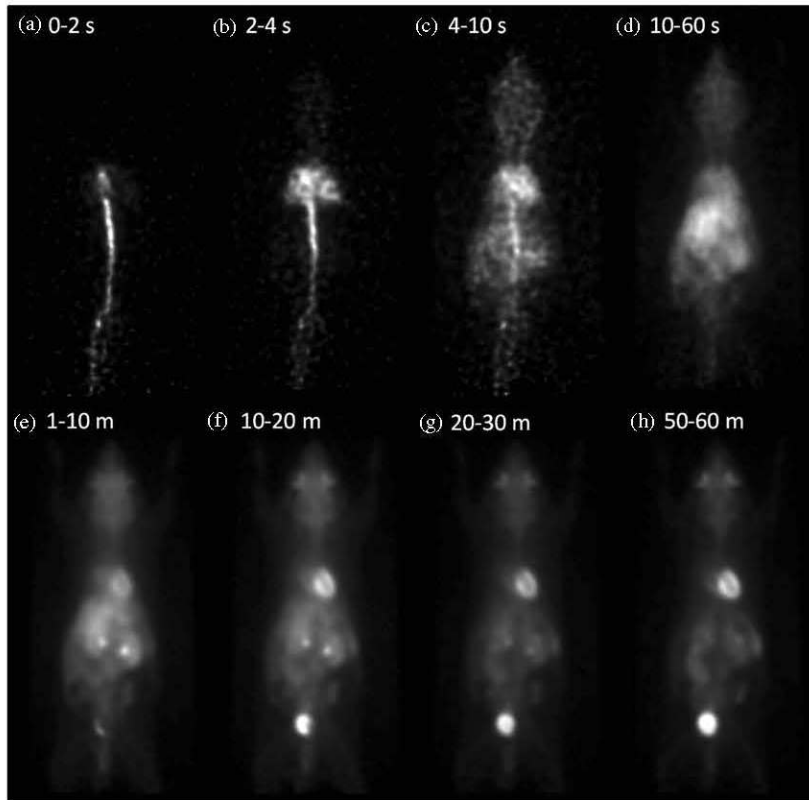


Figure 12. Selected frames from the 1 h dynamic scan of a mouse following a tail injection of 1.59 MBq (43 μ Ci) [18 F]-FDG. Different coronal AIP images are shown for each frame to better reveal the activity distribution for different time periods.

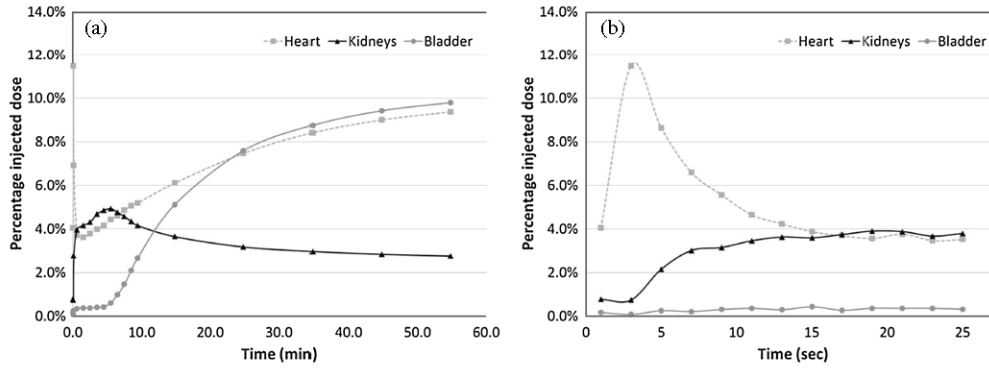


Figure 13. Time activity curves in major organs of a mouse during the 1 h dynamic $[^{18}\text{F}]$ -FDG scan. (a) Organ uptake for the 1 h period. (b) A detailed graph showing the first 26 s following injection. Data was reframed to better display the early changes.

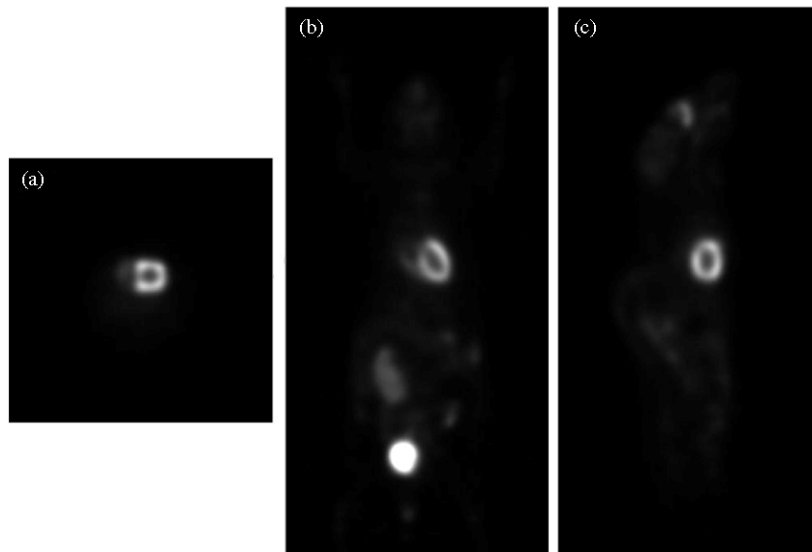


Figure 14. Reconstructed transverse (a), coronal (b) and sagittal (c) slices showing the uptake of $[^{18}\text{F}]$ -FDG in heart and bladder in a healthy mouse during a 10 min scan acquired 50 min after injection. The activity was 0.93 MBq (25 μCi).

show the tail injection in early frames and the activity building up in the lungs, kidney, liver, bladder, and heart in later frames. The measured time–activity curves for the bladder, heart, and kidney are plotted in figure 13, which clearly reveals the trend of activity distribution in these organs as time progresses. Figure 14 shows the reconstructed coronal, sagittal and transverse slices from the last 10 min frame of the same study. The activity in the entire mouse was 0.93 MBq (25 μCi) at scan time. Figure 15 illustrates the capabilities of the PETbox4/MARS combination system. In this static 20 min ^{64}Cu study, a reconstructed three-dimensional volume PET image was registered with the MARS data set to provide an anatomical reference (Wang *et al* 2011, Wang *et al* 2012). The activity in the entire mouse was 0.14 MBq (3.7 μCi) at scan

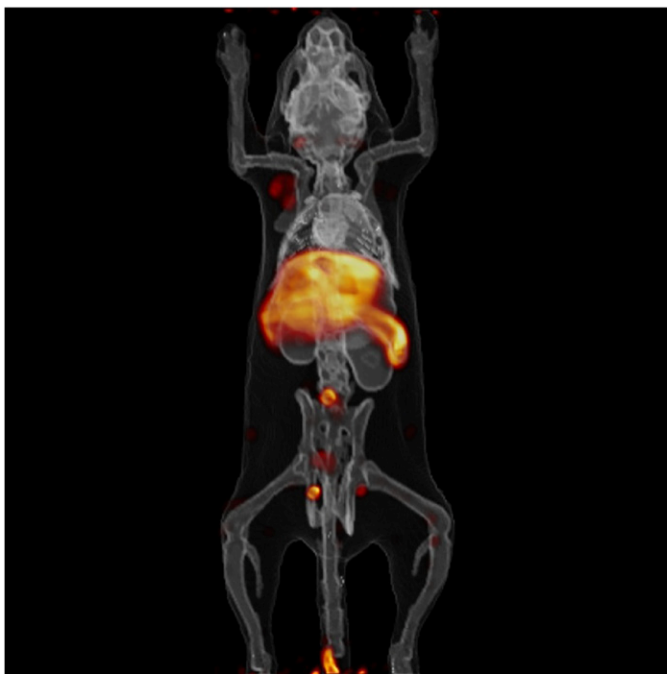


Figure 15. Selected reconstructed three-dimensional volume rendered image with MARS registration showing the uptake of ^{64}Cu radiolabeled minibody in liver in a healthy mouse during a 20 min scan after an uptake of 4 h. The activity was 0.14 MBq (3.7 μCi) in the entire mouse at the scan time.

time. (A video clip can be accessed online as the supplementary data enhancement, available from stacks.iop.org/PMB/58/3791/mmedia.)

4. Discussion

This study has evaluated the overall performance of the PETbox4 system according to NEMA NU-4 standards with some modifications as necessary.

Compared to the first generation PETbox system, PETbox4 employs different crystal-cutting technology that reduces the gaps between adjacent crystals from 200 to 78 μm . The new detector block provides a higher packing fraction of 0.92 compared to 0.83 of the previous generation detectors. With the help of the reflectors between individual pixels used in PETbox4 detectors, the scintillation light collection is improved and the light cross talk between neighbor crystals is suppressed, allowing the use of crystals with smaller cross section and higher aspect ratio. The energy resolution and the average intrinsic spatial resolution of the PETbox4 detector are thus improved to 18% and 1.5 mm FWHM, compared with 20% and 1.8 mm FWHM for that of the PETbox detector, respectively.

With an energy window of 150–650 keV and a timing window of 20 ns, the system peak absolute sensitivity of the PETbox4 reaches 18% at the center of the FOV, a more than four-fold improvement relative to the first generation PETbox system. The significant sensitivity enhancement is due to the more than three-fold detection solid angle increase by doubling the number of detectors modules from 2 to 4, and allowing coincidences between all possible

detector head combinations. Also, the increased thickness of each detector block from 5 mm to 7 mm, and the improved crystal packing fraction from 0.83 to 0.92, contribute further to the sensitivity increase, which should be of benefit in the investigation of biological processes in small animals. The small discrepancy between the Monte Carlo simulations and the measured data is most likely due to differences in the spatial distribution and magnitude of the detector energy resolution. But these results reconfirm the accuracy of the GATE model for estimating the performance parameters of PET systems.

Despite the fact that the detection of coincidences along very oblique angles are allowed owing to the close geometry of the scanner, the ML-EM reconstruction accurately models the physical response of the scanner in the system matrix. As a result, the spatial resolution is fairly homogeneous within the entire FOV and averages at 1.5 mm FWHM with an average volumetric resolution of 3 μ L, allowing the investigation of whole-body biodistribution studies of mice without degradation of the spatial resolution toward the edges of the FOV. The significantly improved uniformity of the image spatial resolution arises mainly from improved data sampling along the anterior-posterior direction by employing two side detectors in the PETbox4 system. The lack of these data was the main source of volumetric resolution degradation at large offsets from the center for the two head PETbox. It is worth to also note here that for the flat panel geometries of the detectors used in both systems, depth of interaction parallax effects for coincidence lines of response are minimal at the edges of the detectors rather than at their center. We also need to stress again that the reconstruction method utilized here deviates significantly from the NEMA NU-4 protocol, because the traditional FBP reconstruction was not available for the PETbox4 geometry. We anticipate that the development of other PET preclinical instruments with geometries that are more radically different from cylindrical ring tradition (Goorden *et al* 2013) for which also FBP is not possible, indicates that the NEMA NU-4 standards need to be revisited. Nevertheless, the absolute measurements of resolution with a point source in air and an iterative reconstruction algorithm need to be taken with an air of caution. *In vivo* images of mouse subjects with distributed sources and background demonstrate that the system is capable of acquiring data and reconstructing high quality images.

Following the NEMA standard, the count rate performance of the PETbox4 has been measured with a mouse-sized cylindrical phantom. The phantom was rotated by 45° to achieve a more symmetric source distribution. However, even with this approach, it is still difficult to compare between PETbox4 and PETbox. For the PETbox, the phantom was placed in the system so that the line source was located at the midway between the two opposing detectors to ensure that the dead time experienced by the two detector heads were similar. For the PETbox4 system, the 1 cm offset line source was much closer to two of the four detector panels. Therefore saturation of the system was dominated by the dead time of these two heads, leading to an underestimated count rate performance compared to a more symmetric activity distribution, such as the image quality phantom study and typical *in-vivo* mouse imaging. With this source geometry, the peak NECR is 35 kcps (achieved at 1.5 MBq). The higher sensitivity of the PETbox4 is such that the peak NECR is reached at lower total activity for this scanner. The overall count rate performance is mainly limited by the highly multiplexed detector readouts (four signals for groups of 1200 crystals) and the slow decay time of the BGO scintillation light. In the future, the count rate performance for the same scintillator can be greatly improved by developing a less multiplexed readout. For the current system, a pulse pile-up rejection and correction method has been implemented for all the data shown here, details of which will be presented elsewhere.

The choice for the 1 cm radial offset of the line source in the NEMA mouse-sized phantom was dictated by Monte Carlo simulations performed to determine the line source

position which gave a SF similar to that found in a uniformly filled cylindrical phantom of the same size (Surti *et al* 2005). For scanners with close geometry, a 1 cm offset of the line source is relatively large difference compared to the radioactivity biodistribution in a typical *in-vivo* mouse acquisition. This difference may cause earlier saturation of detectors closer to the line source and an underestimation of the system count rate performance. The NEMA NU-4 evaluation also strongly depends on the orientation of the phantom, thus making comparisons between systems difficult. Moreover, for scanners with less sensitivity or better count rate performance, high level radioactivity concentration is required to fill the small volume of the line source in order to saturate the system. This approach increases the difficulty of filling the phantom and the dose to the personnel and therefore this is something that we recommend that should be revisited in a possible update to the NEMA standards.

Nevertheless, it is true that the overall peak NEC rate for both PETbox systems is much lower than the peak NEC rate for most other preclinical PET instruments. Even though this performance parameter is interesting, it does not play a significant role under realistic mouse imaging scenarios. The peak NEC rates for most existing preclinical imaging instruments are achieved at mouse phantom activities around (50–200 MBq) (Goertzen *et al* 2012). These total activities at peak NEC are 5–20 times larger than the 7.4 MBq doses typically used today for mouse studies with any preclinical PET system. This typical injected dose is itself 60 times more concentrated than the typical human PET injected dose (296 kBq g⁻¹ versus 5 kBq g⁻¹ respectively). The main reason is that the average 25 g mouse weighs approximately 3000 times less than the average human. Consequently the design goal of the PETbox4 system has been high sensitivity imaging of mice at low dose. The typical injected dose of 1 MBq for studies with the PETbox4 system is seven times smaller than the dose considered standard in the field, a dose established with systems of very different design and capabilities (Chatziaoannou *et al* 1999). For this reason also the NEMA NU-4 mouse image quality phantom in this work was filled with only half the recommended activity, but scanned for the recommended 20 min duration.

Data management can also become an issue in transferring and archiving studies. The PETbox4 system outputs 32-bit list-mode data, half size compared to the previous prototype PETbox system (64-bit) due to the online crystal and energy discriminations implemented in FPGA with the LUT stored in the SDRAM on the VHS-ADC board. This doubles the data transmission bandwidth in the list-mode stream and provides more flexibility for future system development.

The current default energy window is set to be 150–650 keV. Due to the more closely packed system geometry, an increased fraction of backscatter events are included in the coincidence timing window (Goertzen *et al* 2010), which degrade the signal-to-noise ratio of the final image. On the other hand, events that undergo a single Compton interaction in the BGO crystals but still describe the correct line of response should be accepted. Therefore the optimization of energy window in a way that balances these two effects is now under investigation. Scatter correction techniques have not yet been explored or implemented. Future research will also be devoted to implementing adequate scatter correction methodology and evaluations on performing quantitative studies using this system. The MDA, as a combination of the more traditional PET system parameters, represents the performance of a PET scanner at very low activity distributions and is directly related to lesion detection (Bao and Chatziaoannou 2010). Novel molecular imaging applications, such as cell trafficking studies (Adonai *et al* 2002) or gene expression imaging (Blasberg 2002), have brought the need to image small and low activity sources on the order of nano Curies under low contrast conditions. The PETbox4 system, with its high sensitivity and low intrinsic background, should achieve good MDA performance. A comprehensive evaluation of MDA for PETbox4 will be performed and

compared with other systems in future work. Although further improvements are foreseen in the near future for the prototype scanner we have presented in this work, this design has been implemented by Sofie Biosciences (Culver City, CA) into a commercial scanner, GENISYS4.

5. Conclusion

In conclusion, this study has evaluated the basic performance of the PETbox4 system and its improvement over the previous system. Our results indicate a significant improvement in nearly all aspects of typical PET system characteristics compared with the first generation PETbox system. The energy resolution of the PETbox4 system averages 18% for the 511 keV photopeak. The volumetric image resolution remains around 3 μL within the central 4-cm diameter FOV and is uniform along the radial, transverse and axial directions through the whole FOV. The peak sensitivity is 18% with a 150–650 keV energy window and a 20 ns timing window. The peak NEC rate is 35 kcps achieved at a total activity of 1.5 MBq (40 μCi). The selected animal studies show that the system is capable of static and dynamic mouse imaging studies with different radiotracers. The overall performance demonstrates that the PETbox4 scanner is suitable for producing high quality images for molecular imaging based biomedical research, with less administered activity and lower dose delivered to the mice. At the same time, the cost derived from detectors and electronics as well as the system overall footprint is significantly reduced in this design compared with a more conventional ring-based preclinical PET tomographs.

Acknowledgments

The authors would like to thank the staff of the Crump Imaging facility at UCLA including Waldemar Ladno, Darin Williams, and Jeffrey Collins for their assistance with obtaining the ^{18}F solution for this study. This work was supported by the National Institutes of Health under grant no. R24 CA92865, the Department of Energy under contract no. DE-FG02-06ER64249, and the UCLA Foundation from a donation made by Ralph and Marjorie Crump for the UCLA Crump Institute for Molecular Imaging.

The PETbox4 technology presented in this paper has been commercialized by Sofie Biosciences, Inc., Culver City, CA, USA. NTV is currently an employee of Sofie Biosciences, Inc., and NTV, MEP, DBS and AFC are shareholders of Sofie Biosciences, Inc.

References

- Adonai N, Nguyen K N, Walsh J, Iyer M, Toyokuni T, Phelps M E, McCarthy T, McCarthy D W and Gambhir S S 2002 *Ex vivo* cell labeling with Cu-64-pyruvaldehyde-bis(N-4-methylthiosemicarbazone) for imaging cell trafficking in mice with positron-emission tomography *Proc. Natl Acad. Sci. USA* **99** 3030–5
- Amundson S A, Bittner M, Meltzer P, Trent J and Formace A J 2001 Induction of gene expression as a monitor of exposure to ionizing radiation *Radiat. Res.* **156** 657–61
- Bao Q and Chatzioannou A F 2007 GATE simulation of a BGO based high sensitivity small animal PET scanner *Joint Meeting of the 6th Int. Conf. on Noninvasive Functional Source Imaging of the Brain and Heart and the Int. Conf. on Functional Biomedical Imaging* pp 47–50
- Bao Q N and Chatzioannou A F 2010 Estimation of the minimum detectable activity of preclinical PET imaging systems with an analytical method *Med. Phys.* **37** 6070–83
- Bao Q, Newport D, Chen M, Stout D B and Chatzioannou A F 2009 Performance evaluation of the inveon dedicated PET preclinical tomograph based on the NEMA NU-4 standards *J. Nucl. Med.* **50** 401–8
- Bergeron M *et al* 2009 Performance evaluation of the LabPET APD-based digital PET scanner *IEEE Trans. Nucl. Sci.* **56** 10–16
- Blasberg R 2002 PET imaging of gene expression *Eur. J. Cancer* **38** 2137–46

- Bloomfield P M *et al* 1995 The design and physical characteristics of a small animal positron emission tomograph *Phys. Med. Biol.* **40** 1105–26
- Canadas M, Embid M, Lage E, Desco M, Vaquero J J and Perez J M 2011 NEMA NU 4-2008 performance measurements of two commercial small-animal PET scanners: ClearPET and rPET-1 *IEEE Trans. Nucl. Sci.* **58** 58–65
- Chatziioannou A F 2002a Molecular imaging of small animals with dedicated PET tomographs *Eur. J. Nucl. Med.* **29** 98–114
- Chatziioannou A F 2002b PET scanners dedicated to molecular imaging of small animal models *Mol. Imaging Biol.* **4** 47–63
- Chatziioannou A F, Cherry S R, Shao Y P, Silverman R W, Meadors K, Farquhar T H, Pedarsani M and Phelps M E 1999 Performance evaluation of microPET: a high-resolution lutetium oxyorthosilicate PET scanner for animal imaging *J. Nucl. Med.* **40** 1164–75
- Cherry S R *et al* 1997 MicroPET: a high resolution PET scanner for imaging small animals *IEEE Trans. Nucl. Sci.* **44** 1161–6
- Correia J A, Burnham C A, Kaufman D, Brownell A L and Fischman A J 2004 Performance evaluation of MMP-II: a second-generation small animal PET *IEEE Trans. Nucl. Sci.* **51** 21–26
- de Jong H W A M, van Velden F H P, Kloet R W, Buijs F L, Boellaard R and Lammertsma A A 2007 Performance evaluation of the ECAT HRRT: an LSO-LYSO double layer high resolution, high sensitivity scanner *Phys. Med. Biol.* **52** 1505–26
- de Marcillac P, Coron N, Dambier G, Leblanc J and Moalic J P 2003 Experimental detection of alpha-particles from the radioactive decay of natural bismuth *Nature* **422** 876–8
- Di Domenico G *et al* 2003 YAP-(S)PET small animal scanner: quantitative results *IEEE Trans. Nucl. Sci.* **50** 1351–6
- Funk T, Sun M and Hasegawa B H 2004 Radiation dose estimate in small animal SPECT and PET *Med. Phys.* **31** 2680–6
- Gagnon M K J, Hausner S H, Marik J, Abbey C K, Marshall J F and Sutcliffe J L 2009 High-throughput *in vivo* screening of targeted molecular imaging agents *Proc. Natl Acad. Sci. USA* **106** 17904–9
- Gambhir S S 2002 Molecular imaging of cancer with positron emission tomography *Nature Rev. Cancer* **2** 683–93
- Goertzen A L, Stout D B and Thompson C J 2010 A method for measuring the energy spectrum of coincidence events in positron emission tomography *Phys. Med. Biol.* **55** 535–49
- Goertzen A L, Suk J Y and Thompson C J 2007 Imaging of weak-source distributions in LSO-based small-animal PET scanners *J. Nucl. Med.* **48** 1692–8
- Goertzen A L *et al* 2012 NEMA NU 4-2008 comparison of preclinical PET imaging systems *J. Nucl. Med.* **53** 1300–9
- Goorden M C, van der Have F, Kreuger R, Ramakers R M, Vastenhouw B, Burbach J P, Booij J, Molthoff C F and Beekman F J 2013 VECTor: a preclinical imaging system for simultaneous submillimeter SPECT and PET *J. Nucl. Med.* **54** 306–12
- Huisman M C, Reder S, Weber A W, Ziegler S I and Schwaiger M 2007 Performance evaluation of the Philips MOSAIC small animal PET scanner *Eur. J. Nucl. Med. Mol. Imaging* **34** 532–40
- Hume S P, Gunn R N and Jones T 1998 Pharmacological constraints associated with positron emission tomographic scanning of small laboratory animals *Eur. J. Nucl. Med.* **25** 173–6
- Jan S *et al* 2004 GATE: a simulation toolkit for PET and SPECT *Phys. Med. Biol.* **49** 4543–61
- Jeavons A P, Chandler R A and Dettmar C A R 1999 A 3D HIDAC-PET camera with sub-millimetre resolution for imaging small animals *IEEE Trans. Nucl. Sci.* **46** 468–73
- Knoess C *et al* 2003 Performance evaluation of the microPET R4 PET scanner for rodents *Eur. J. Nucl. Med. Mol. Imaging* **30** 737–47
- Laforest R, Longford D, Siegel S, Newport D F and Yap J 2007 Performance evaluation of the microPET (R)-FOCUS-F120 *IEEE Trans. Nucl. Sci.* **54** 42–9
- Lage E, Vaquero J J, Sisniega A, Espana S, Tapias G, Abella M, Rodriguez-Ruano A, Ortuno J E, Udias A and Desco M 2009 Design and performance evaluation of a coplanar multimodality scanner for rodent imaging *Phys. Med. Biol.* **54** 5427–41
- Lecomte R, Cadorette J, Rodrigue S, Lapointe D, Rouleau D, Bentourkia M, Yao R and Msaki P 1996 Initial results from the Sherbrooke avalanche photodiode positron tomograph *IEEE Trans. Nucl. Sci.* **43** 1952–7
- Li H D, Wong W H, Baghaei H, Uribe J, Wang Y, Zhang Y X, Kim S S, Ramirez R, Liu J G and Liu S T 2007 The engineering and initial results of a transformable low-cost high-resolution PET camera *IEEE Trans. Nucl. Sci.* **54** 1583–8
- Malakoff D 2000 The rise of the mouse, biomedicine's model mammal *Science* **288** 248–53
- Marshall E 2001 Genome sequencing—Celera assembles mouse genome; public labs plan new strategy *Science* **292** 822–3
- Miyaoka R S, Janes M L, Lee K, Park B, Kinahan P E and Lewellen T K 2005 Development of a single detector ring micro crystal element scanner: QuickPET II *Mol. Imaging* **4** 117–27

- Mumcuoglu E U, Leahy R, Cherry S R and Zhou Z Y 1994 Fast gradient-based methods for Bayesian reconstruction of transmission and emission PET images *IEEE Trans. Med. Imaging* **13** 687–701
- Myers R 2001 The biological application of small animal PET imaging *Nucl. Med. Biol.* **28** 585–93
- Paigen K 1995 A miracle enough: the power of mice *Nature Med.* **1** 215–20
- Phelps M E 2000 Positron emission tomography provides molecular imaging of biological processes *Proc. Natl Acad. Sci. USA* **97** 9226–33
- Prasad R, Ratib O and Zaidi H 2010 Performance evaluation of the FLEX triumph X-PET scanner using the national electrical manufacturers association NU-4 standards *J. Nucl. Med.* **51** 1608–15
- Prasad R, Ratib O and Zaidi H 2011 NEMA NU-04-based performance characteristics of the LabPET-8 (TM) small animal PET scanner *Phys. Med. Biol.* **56** 6649–64
- Rouze N C, Schmand M, Siegel S and Hutchins G D 2004 Design of a small animal PET imaging system with 1 microliter volume resolution *IEEE Trans. Nucl. Sci.* **51** 757–63
- Sanchez F *et al* 2012 Small animal PET scanner based on monolithic LYSO crystals: performance evaluation *Med. Phys.* **39** 643–53
- Schafers K P, Reader A J, Kriens M, Knoess C, Schober O and Schafers M 2005 Performance evaluation of the 32-module quadHIDAC small-animal PET scanner *J. Nucl. Med.* **46** 996–1004
- Seidel J, Vaquero J J and Green M V 2003 Resolution uniformity and sensitivity of the NIH ATLAS small animal PET scanner: comparison to simulated LSO scanners without depth-of-interaction capability *IEEE Trans. Nucl. Sci.* **50** 1347–50
- Surti S, Karp J S, Perkins A E, Cardi C A, Daube-Witherspoon M E, Kuhn A and Muehllehner G 2005 Imaging performance of A-PET: a small animal PET camera *IEEE Trans. Med. Imaging* **24** 844–52
- Surti S, Karp J S, Perkins A E, Freifelder R and Muehllehner G 2003 Design evaluation of A-PET: A high sensitivity animal PET camera *IEEE Trans. Nucl. Sci.* **50** 1357–63
- Szanda I, Mackewn J, Patay G, Major P, Sunassee K, Mullen G E, Nemeth G, Haemisch Y, Blower P J and Marsden P K 2011 National electrical manufacturers association NU-4 performance evaluation of the PET component of the NanoPET/CT preclinical PET/CT scanner *J. Nucl. Med.* **52** 1741–7
- Tai Y C, Chatziaoannou A, Siegel S, Young J, Newport D, Goble R N, Nutt R E and Cherry S R 2001 Performance evaluation of the microPET P4: a PET system dedicated to animal imaging *Phys. Med. Biol.* **46** 1845–62
- Tai Y C, Chatziaoannou A F, Yang Y F, Silverman R W, Meadors K, Siegel S, Newport D F, Stichel J R and Cherry S R 2003 MicroPET II: design, development and initial performance of an improved microPET scanner for small-animal imaging *Phys. Med. Biol.* **48** 1519–37
- Tai Y C, Ruangma A, Rowland D, Siegel S, Newport D F, Chow P L and Laforest R 2005 Performance evaluation of the microPET focus: a third-generation microPET scanner dedicated to animal imaging *J. Nucl. Med.* **46** 455–63
- Taschereau R and Chatziaoannou A F 2007 Monte Carlo simulations of absorbed dose in a mouse phantom from 18-fluorine compounds *Med. Phys.* **34** 1026–36
- Taschereau R, Rannou F R and Chatziaoannou A F 2011 A modeled point spread function for a noise-free system matrix *IEEE Nucl. Sci. Symp. Conf. Record* pp 4102–5
- Wang G J and Cai L 2000 Induction of cell-proliferation hormesis and cell-survival adaptive response in mouse hematopoietic cells by whole-body low-dose radiation *Toxicol. Sci.* **53** 369–76
- Wang H, Stout D B and Chatziaoannou A F 2011 Mouse atlas registration with non-tomographic imaging modalities—a pilot study based on simulation *Mol. Imaging Biol.* **14** 408–19
- Wang H K, Stout D B, Taschereau R, Gu Z, Vu N T, Prout D L and Chatziaoannou A F 2012 MARS: a mouse atlas registration system based on a planar x-ray projector and an optical camera *Phys. Med. Biol.* **57** 6063–77
- Wang Y C, Seidel J, Tsui B M W, Vaquero J J and Pomper M G 2006 Performance evaluation of the GE healthcare eXplore VISTA dual-ring small-animal PET scanner *J. Nucl. Med.* **47** 1891–900
- Weber S, Bauer A, Herzog H, Kehren F, Muhlensiepen H, Vogelbruch J, Coenen H H, Zilles K and Halling H 2000 Recent results of the TierPET scanner *IEEE Trans. Nucl. Sci.* **47** 1665–9
- Weissleder R and Mahmood U 2001 Molecular imaging *Radiology* **219** 316–33
- Yonezawa M 2006 Induction of radio-resistance by low dose X-irradiation *Yakugaku Zasshi* **126** 833–40
- Zhang H, Bao Q A, Vu N T, Silverman R W, Taschereau R, Berry-Pusey B N, Douraghy A, Rannou F R, Stout D B and Chatziaoannou A F 2011 Performance evaluation of PETbox: a low cost bench top preclinical PET scanner *Mol. Imaging Biol.* **13** 949–61
- Zhang H, Vu N T, Bao Q, Silverman R W, Berry-Pusey B N, Douraghy A, Williams D A, Rannou F R, Stout D B and Chatziaoannou A F 2010 Performance characteristics of BGO detectors for a low cost preclinical PET scanner *IEEE Trans. Nucl. Sci.* **57** 1038–44
- Ziemons K *et al* 2005 The ClearPET (TM) project: development of a 2nd generation high-performance small animal PET scanner *Nucl. Instrum. Methods A* **537** 307–11

Chapter 3

System Optimization: Energy Window Optimization

Optimization of the Energy Window for PETbox4, a Preclinical PET Tomograph With a Small Inner Diameter

Z. Gu, *Student Member, IEEE*, Q. Bao, R. Taschereau, H. Wang, B. Bai, *Member, IEEE*, and A. F. Chatziioannou, *Senior Member, IEEE*

Abstract—Small animal positron emission tomography (PET) systems are often designed by employing close geometry configurations. Due to the different characteristics caused by geometrical factors, these tomographs require data acquisition protocols that differ from those optimized for conventional large diameter ring systems. In this work we optimized the energy window for data acquisitions with PETbox4, a 50 mm detector separation (box-like geometry) pre-clinical PET scanner, using the Geant4 Application for Tomographic Emission (GATE). The fractions of different types of events were estimated using a voxelized phantom including a mouse as well as its supporting chamber, mimicking a realistic mouse imaging environment. Separate code was developed to extract additional information about the gamma interactions for more accurate event type classification. Three types of detector backscatter events were identified in addition to the trues, phantom scatters and randoms. The energy window was optimized based on the noise equivalent count rate (NECR) and scatter fraction (SF) with lower-level discriminators (LLD) corresponding to energies from 150 keV to 450 keV. The results were validated based on the calculated image uniformity, spillover ratio (SOR) and recovery coefficient (RC) from physical measurements using the National Electrical Manufacturers Association (NEMA) NU-4 image quality phantom. These results indicate that when PETbox4 is operated with a more narrow energy window (350–650 keV), detector backscatter rejection is unnecessary. For the NEMA NU-4 image quality phantom, the SOR for the water chamber decreases by about 45% from 15.1% to 8.3%, and the SOR for the air chamber decreases by 31% from 12.0% to 8.3% at the LLDs of 150 and 350 keV, without obvious change in uniformity, further supporting the simulation based optimization. The optimization described in this work is not limited to PETbox4, but also applicable or helpful to other small inner diameter geometry scanners.

Index Terms—Backscatter, energy window, GATE, NECR, optimization, PET, PETbox4, SF.

Manuscript received September 15, 2013; revised February 02, 2014; accepted April 10, 2014. Date of publication June 04, 2014; date of current version June 12, 2014. This work was supported in part by the National Institutes of Health under grant no. R24CA92865, in part by the Department of Energy under Contract no. DE-FG02-06ER64249, and in part by the UCLA Foundation from a donation made by Ralph and Marjorie Crump for the UCLA Crump Institute for Molecular Imaging.

Z. Gu, Q. Bao, R. Taschereau, H. Wang, and A. F. Chatziioannou are with the Crump Institute for Molecular Imaging, David Geffen School of Medicine, University of California at Los Angeles, Los Angeles, CA 90095 USA (e-mail: zhgu@mednet.ucla.edu; archatzioann@mednet.ucla.edu).

B. Bai is with the Keck School of Medicine, University of Southern California, Los Angeles, CA 90033 USA.

Color versions of one or more of the figures in this paper are available online at <http://ieeexplore.ieee.org>.

Digital Object Identifier 10.1109/TNS.2014.2321326

I. INTRODUCTION

SMALL animal positron emission tomography (PET) is a widely used imaging modality for non-invasive, in vivo studies of biochemical and metabolic process [1], [2]. High imaging performance is desired for good lesion localization and quantification for applications in pharmacology, genetics, pathology and oncology [3], [4]. For a specific scanner, the imaging protocol including energy window, multiple event acceptance policy, and timing window, need to be optimized to achieve an overall optimized imaging quality.

In recent years several systems have been built or designed by employing close geometry configurations, with the diameters ranging from 35 mm to 65 mm [5]–[10]. Close geometry has many benefits such as high sensitivity provided by the larger detection solid angle, lower cost and reduced complexity [5]. On the other hand, the system characteristics related to the geometries of those scanners are very different from those of the conventional large diameter preclinical PET scanners [11], [12].

Scatter events degrade image contrast in PET by misplacing events during reconstruction and cause errors in the reconstructed radioactivity concentration [13]. There has been extensive research to investigate the scatter fraction (SF) and optimal energy window for conventional small animal PET systems with large inner diameters, for which the object SF originating from a mouse does not change significantly as the lower-level discriminator (LLD) increases [13], [14]. This is because events that scatter through a small angle result in lines of response that still intersect the FOV of mouse imaging, and most of these photons do not lose enough energy and thus are less sensitive to the increase of LLD. A wide open energy window has been suggested or implemented to increase the sensitivity without significantly increasing the scatter and degrading the spillover ratio (SOR) for mouse imaging [14]–[16].

For a scanner employing a close geometry and wide open energy window, scatter events with a larger angle can now intersect the object. This effect increases the fraction of detected scattered events and leads to degradation of the noise equivalent count rate (NECR) [17], despite the small size of typical imaged subjects. Moreover, due to the large detection solid angle, the 511 keV gamma photons have a higher probability of undergoing a Compton scatter interaction in one detector and then being detected in a second detector, resulting in backscatter coincidence events [18]. Therefore, the optimization of energy

window for conventional large inner diameter ring systems cannot be directly applied to close geometry systems.

PETBox4 is a PET system optimized specifically for imaging mice [5]. The system consists of four bismuth germanate (BGO) detector panels, with the opposite panels placed at a spacing of 50 mm. Such close geometry provides a useful field of view (FOV) that can accommodate the vast majority of mice (18–40 g) and therefore presents a compromise in the target subject size in exchange for low cost and high sensitivity.

In this study, different types of possible events in PETbox4 were investigated using the Geant4 application for tomographic emission (GATE) Monte Carlo simulation [19]. GATE, with the well validated Geant4 libraries [20], [21], allows highly realistic modeling of scanner geometries, and provides detailed information about transport and energy deposition of each particle. The fraction, energy and spatial distribution of different types of events which cannot be directly retrieved from physical measurements, can be studied with the help of this simulation on an event-by-event basis. Based on the simulation results, the multiple event acceptance policy and the need for backscatter rejection were investigated for PETbox4. A new optimized energy window was proposed and validated with physical measurements of the National Electrical Manufacturers Association (NEMA) NU-4 [22] image quality phantom data acquired in PETbox4.

II. METHODS

A. Modeling the System with GATE

The PETbox4 detector module and system configuration are shown in Fig. 1. The basic specifications of the PETbox4 system are summarized in Table I. The GATE Monte Carlo simulation software was used to simulate the data acquired with the PETbox4.

The scanner geometry and associated event handling of the PETbox4 were modeled, with the timing window set to 20 ns. Unless explicitly stated otherwise, all simulations were acquired with an energy resolution of 18%, which is the average measured energy resolution of the PETbox4. The notable exception to this was in one of the NECR and SF simulations described in Section II-D (5), for which the energy resolution was set to 30% as a worst case scenario to evaluate the effect of the poorer energy resolution in a more realistic system on NECR and SF. An energy window of 50-650 keV was applied to the singles processing chain at the stage of initial simulation. The *takeAllGoods* criterion (all the good sub-pairs in multiple coincidences are accepted) was chosen to manage multiple coincidences and the *minSectorDifference* parameter was set to 1, mimicking the system firmware of allowing coincidences in the PETbox4 scanner. Dead time was not modeled, and pile-up events caused by different annihilation events were not considered in this study. Annihilation events were modeled with the emission of opposing pairs of 511 keV photons to speed up the simulation time. The *Root* format output from GATE [23] stores information of particle transportation and interactions on an event-by-event basis, allowing event history to be retrieved.

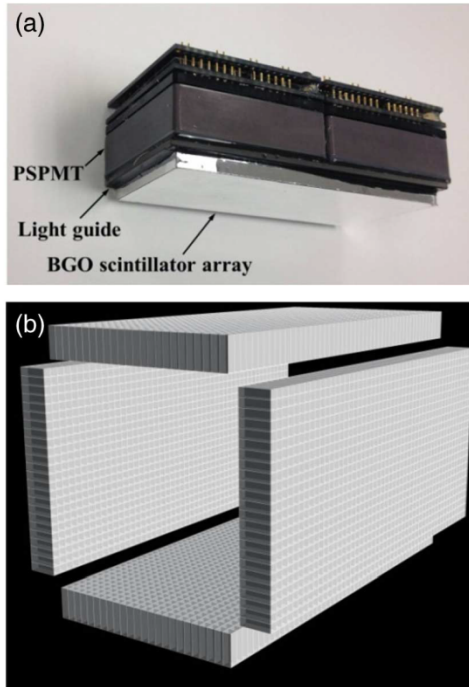


Fig. 1. (a) A photograph of a PETbox4 detector module. The complete detector module employs two H8500 PMTs to detect scintillation light from a 24×50 BGO crystal array. (b) PETbox4 system detector configuration. Four detector modules are arranged in a box-like geometry, with a crystal separation of 5 mm between opposing detector panels.

TABLE I
BASIC SPECIFICATIONS OF THE PETBOX4 SYSTEM

Crystal material	BGO
Photodetector	PSPMT (H8500)
Detector separation	50 mm
Crystal size	$1.825 \times 1.825 \times 7 \text{mm}^3$
Number of crystals	24×50 (per detector panel)
Number of detector panels	4
Transaxial FOV	45 mm
Axial FOV	94 mm
Solid Angle fraction	~87%
Coincidence time window	20 ns
Average energy resolution	18%

This model has been validated in [5] against the system sensitivity measurement, showing an agreement within 10% of the measured value.

B. Voxelized Phantom

One of the most important applications of preclinical PET imaging is the measurement of the whole body biodistribution of a radiolabeled probe. For optimization of realistic mouse imaging, simulations were performed with a voxelized phantom including a mouse as well as its supporting chamber to provide the most accurate scatter estimation in heterogeneous media and complex geometry. Among the mouse data we have, a data set from an 18.2 g mouse was chosen, representing the lower limit of object SF that can be introduced from a mouse subject among the vast majority of mice (18-40 g)

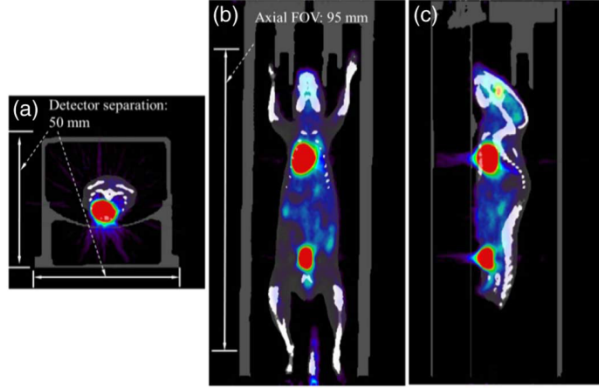


Fig. 2. Three different views (transverse (a), coronal (b) and sagittal (c)) from the voxelized phantom including the mouse anatomical data and imaging chamber data, with emission (colored) data overlaid. Attenuation coefficient values were assigned for the anatomical and imaging chamber data.

[24]. The geometry of the mouse and the chamber was measured using a MicroCAT II tomograph (Siemens Preclinical Solutions, Knoxville, TN). A sample FDG-PET mouse emission image was used to represent realistic radionuclide distribution in the mouse model. The total activity in the mouse was set to be 1.85 MBq (50 μ Ci), which is the recommended injected dose for this scanner [5]. The phantom, including the mouse and the imaging chamber were implemented in a voxelized phantom with a matrix size of $200 \times 182 \times 496$ and voxel size of $0.25 \times 0.25 \times 0.25$ mm³. As an example, three different views from overlaid anatomy and emission slices of the voxelized phantom are shown in Fig. 2.

C. Event Classification

Coincidence events in PETbox4 can be classified into six primary categories (as shown in Fig. 3):

1) *True Coincidences (T)*: Both detected photons are emitted from one annihilation event without Compton interaction in the object. Both photons are detected in the detector panel of first interaction, with the energy deposited in each detector contributed by only one annihilation photon (Fig. 3(1)). A fraction of these events will undergo Compton scatter in the detector. In conventional Anger logic detectors, such as those used in the PETbox4, the center of mass of the primary and scatter photon interactions fall inside the width of the primary events, as defined in the NEMA NU-4 protocol [22]. In line with previous work, these events are categorized as trues [9].

2) *Phantom Scatter (PS)*: At least one annihilation photon is detected after encountering a Compton interaction in the object (Fig. 3(2)).

3) *Single Photon Backscatters (SPB)*: One annihilation photon is not detected by any detector, while the other is detected by two detectors through backscattering ((Fig. 3(3)).

4) *Backscattered Multiples (BM)*: Both photons emitted from one annihilation event are detected and at least one photon is detected by two detectors through backscattering, leading to multiple coincidence events (Fig. 3(4)). The mis-positioned line of response (LOR) in the multiples will be classified

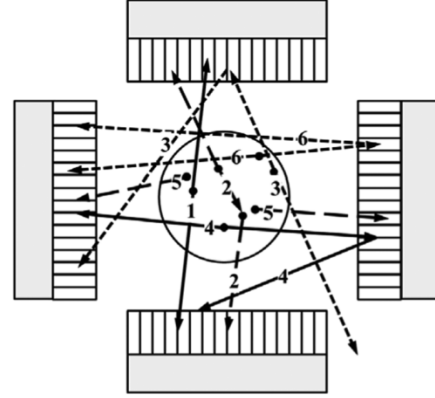


Fig. 3. Illustration of different types of coincidence events: (1) Trues, (2) phantom scatters, (3) single photon backscatters, (4) backscattered multiples, (5) randoms, (6) pile-ups.

into backscatter multiples (For example, two coincidences in a triple event or four coincidences in a quadruple event are mis-positioned and identified as backscatter multiples, corresponding to the coincidence between the backscattered photon with its originating Compton scatter, or with other annihilation photons).

5) *Randoms (R)*: Two photons detected are emitted from different annihilation events (Fig. 3(5)).

6) *Pile-Ups (PU)*: The energy deposited in one detector panel is contributed by both annihilation photons through backscattering (Fig. 3(6)).

To retrieve the characteristics of coincidence events for appropriate event classification, customized software was developed in C++ to analyze the *Root* output file from GATE. The interaction history of each particle in each coincidence event was investigated by the algorithm at eight steps, as shown in Fig. 4. The detailed instructions for each step are included in the Appendix section.

The energy spectrum for different types of events was plotted with an open energy window of 150-650 keV. Then the counts for each event type were sorted with the LLD increasing from 150 keV to 450 keV at 50 keV steps and an upper-level threshold (ULD) fixed at 650 keV. The numbers of counts as a function of event type and LLD were extracted.

D. Energy Window Optimization Based on NECR and SF

1) *NECR and SF Calculation*: The count rates of different event types were extracted from the voxelized mouse phantom simulation, and the corresponding NECR and SF were calculated as below:

$$NECR = T^2 / (P + R) \quad (1)$$

$$SF = S_{tot} / (S_{tot} + T) \quad (2)$$

$$P = T + PU + BM + SPB + PS + R \quad (3)$$

$$S_{tot} = PU + BM + SPB + PS \quad (4)$$

T , PU , BM , SPB , PS and R are the count rates for different types of events as defined in Section II-C. S_{tot} is the

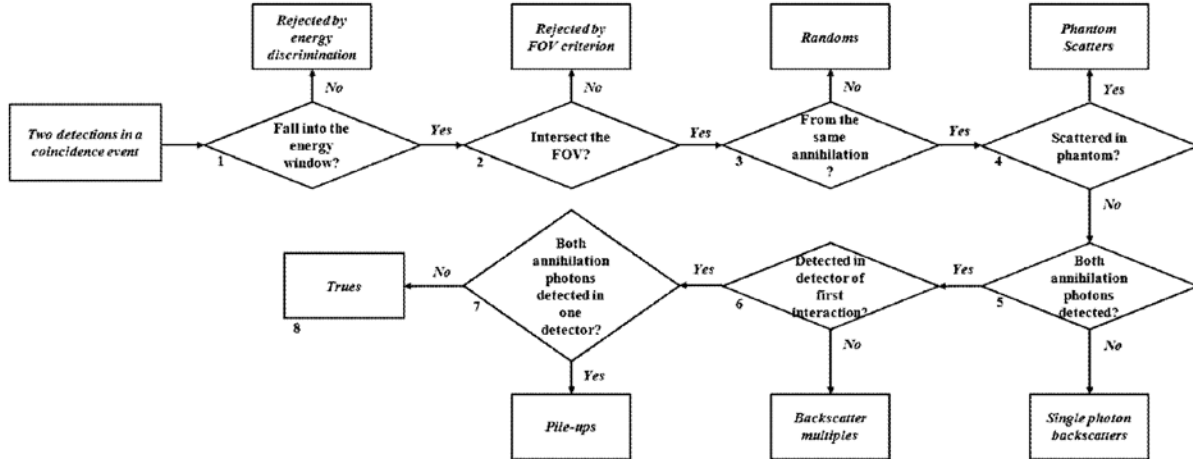


Fig. 4. Detection scheme for different types of coincidence events.

count rate of the total scatter events and P is the count rate of the prompt events. NECR and SF are plotted as a function of the energy window, with the LLD increasing from 150 keV to 450 keV at 50 keV increments.

2) *Identification of Backscatter Events*: For event classification in previous studies performed by other groups [9], [14], [25], events were most commonly categorized into trues, phantom scatters and randoms. To illustrate the importance of appropriate classification of the backscatter events (including backscatter multiples, single photon backscatters and pile-ups) for our study, the NECR and SF were calculated without identifying backscatter events (excluding steps 5, 6 and 7 in Fig. 4). In that case, all the backscatter events were wrongly identified as trues.

3) *Backscatter Rejection*: Although backscatter events cannot be rejected by traditional energy discrimination if a wide open energy window is used via the lower level discriminator, other methods might be applicable for eliminating or suppressing backscatters. For example, the sum of energy deposited from a backscattered photon and its original Compton scatter will have a high probability of falling into a 511 keV peak, making it possible to eliminate a large fraction of single photon backscatters by applying energy discrimination on the sum of the energies from the two detections in a coincidence event. Backscatter multiple events can be suppressed by employing a multiple event policy based on *takeWinnerOfGoods* (only the sub-pair with the highest energy in multiple coincidences is accepted), or *killAll* (no multiple coincidences are accepted, no matter how many sub-pairs are present) as defined in GATE. Alternatively, one could use geometry criteria to extract true LORs and reject mis-positioned LORs from multiple coincidences as reported in [26]. To investigate the necessity of implementing backscatter rejection, the NECR and SF were derived assuming a perfect backscatter rejection by arbitrarily setting the backscatter events to zero, representing the upper limit of what can be achieved with the rejection methods described above.

4) *Effect of the Imaging Chamber*: To examine the contribution from the attenuation and scatter introduced by the

imaging chamber to the total SF, a simulation without the imaging chamber was performed, from which NECR and SF were derived.

5) *Effect of the Energy Resolution*: In the previous simulations, an 18% energy resolution was used based on the measured average energy resolution of PETBox4. However in a realistic system, the energy resolution ranges from 13.5% to 48.3% due to the poorer light collection efficiency for edge crystals or crystals at the junction of the two position-sensitive photomultiplier tubes (PSPMT). About 21% of the crystals have energy resolution worse than 20%. To evaluate the effect of the poorer energy resolution on imaging performance in a more realistic system, a simulation with an energy resolution of 30% was performed as a worst case scenario, from which NECR and SF were derived.

The optimized energy window was proposed based on the NECR and SF results. The event fraction within the open energy window of 150-650 keV utilized in [5] and the proposed optimized energy window were plotted to show the improvement on data quality.

E. NEMA NU-4 Image Quality Phantom

A physical measurement was performed using the image quality phantom described in the NEMA NU-4 protocol [22] to validate the simulation based optimization. Since the PETbox4 is intended to be used with a low injected dose, the image-quality phantom (Data Spectrum Corporation, Hillsborough, NC) was filled with 1.85 MBq (50 μ Ci) ^{18}F solution measured with a dose calibrator (Atomlab 300; Biodex Medical Systems, Shirley, NY). The phantom was placed on a mouse imaging chamber to simulate actual mouse imaging and was scanned for 20 min, following the NEMA NU-4 recommendations. For this acquisition, specialized software was utilized on the system electronics, recording the energy of each event into the list-mode data. After the acquisition, energy discrimination with the LLD increasing from 150 keV to 350 keV at 50 keV steps and a ULD fixed at 650 keV was applied to the list mode data in MATLAB (MathWorks, Natick, MA) before data histogramming. Energy window

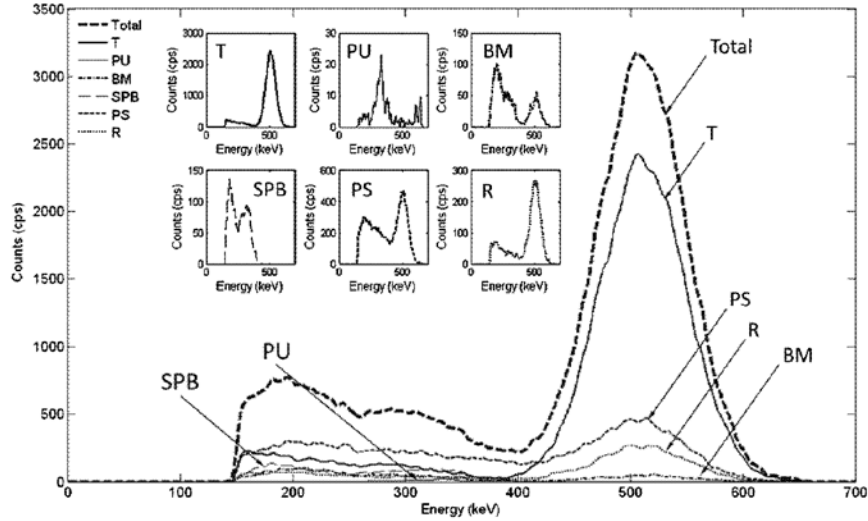


Fig. 5. Energy spectrums of different event types in a simulated mouse scan (including the imaging chamber). The energy spectrum for each event type was magnified in the inset, with the y axis rescaled respectively for better visualization of the distribution characteristics: trues (T), pile-ups (PU), backscattered multiples (BM), single photon backscatters (SPB), phantom scatters (PS) and randoms (R).

specific normalizations were applied to compensate for the differences in individual detector efficiencies, estimated from measurements of a cylindrical source filled with ^{18}F . Random event correction was applied using a delayed coincidence window method, but no scatter correction was applied. For attenuation correction, a CT transmission scan of the object and its supporting chamber was obtained using a MicroCAT II tomograph (Siemens Preclinical Solutions, Knoxville, TN). The reconstructed CT image was registered with the PET emission image and forward projected through the system response matrix to create an attenuation sinogram. The image was reconstructed by a maximum likelihood and expectation maximization (ML-EM) algorithm with 60 iterations [27]. The uniformity, SOR and recovery coefficient (RC) were calculated from the reconstructed images following the NEMA NU-4 protocol.

III. RESULTS

A. Event Classification

Fig. 5 shows the contributions of different types of events to the coincidence energy spectrum. Between 400 and 650 keV, trues from photoelectric interactions dominate. Between 150 and 400 keV, scatter events including phantom scatter and crystal backscatter are higher than true events.

The energy spectrum for each event type was magnified in the inset in Fig. 5, with the y axis rescaled respectively for better visualization of the distribution characteristics. The phantom scatter spectrum (PS in Fig. 5) occupies the second largest fraction of the total prompt events, from which a larger fraction below the photopeak can be observed compared to the energy spectrum of the trues. This is because at least one annihilation photon from each coincidence lost part of its energy through Compton interaction in the object.

For the single photon backscatter energy spectrum (SPB in Fig. 5), two peaks can be clearly observed. The first corresponds to the energy deposited due to Compton scatter of annihilation photons in the detector of first interaction (around 340 keV), while the second (around 170 keV) corresponds to the energy deposited from the backscattered photons in a different detector.

For the backscatter multiples energy spectrum (BM in Fig. 5), besides a similar energy distribution contributed from the annihilation photon encountering crystal backscatter as described in the single photon backscatters (SPB in Fig. 5), coincidence events can also be formed between the backscattered photon and the other annihilation photon. As a result, a 511 keV peak is obtained.

For the pile-up energy spectrum (PU in Fig. 5), a peak around 340 keV can be clearly observed, corresponding to the energy deposited by the Compton interaction from one of the two annihilation photons. The backscattered photon escapes from the detector that it first interacts and deposits its energy in a second detector, together with the other annihilation photon. The energy deposited by pile-up events will form a peak around 680 keV corresponding to the full energy deposited from the backscattered photon and the other annihilation photon, part of which is cut off by the ULD of 650 keV.

The shape of the energy spectrum for random events (R in Fig. 5) is similar to that of the total prompt events. With a total radioactivity of 1.85 MBq ($50\ \mu\text{Ci}$) recommended as the default activity level for mouse imaging using the PETbox4, the fraction of random events is around 8%.

Fig. 6 shows the count rate as a function of event type and LLD. With a LLD of 150 keV, a large fraction of backscattered multiples, single photon backscatters and phantom scatters are included. As the LLD increases from 150 keV to 350 keV, almost all the backscattered multiples and single photon backscatters events are rejected. The phantom scatter events decrease by

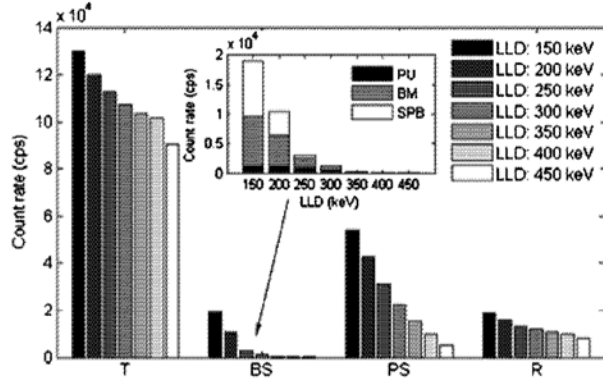


Fig. 6. Count rate as a function of event type and LLD: trues (T), backscatters (BS), phantom scatters (PS) and randoms (R). The composition of the backscatters was shown in the inset: pile-ups (PU), backscattered multiples (BM) and single photon backscatters (SPB).

71% and the random events decrease by 44%. As a tradeoff, trues also decrease by 21%. With a LLD of 450 keV, trues decrease significantly due to the exclusion of photopeak events.

B. Energy Window Optimization

1) *NECR and SF Calculation:* The curve represented by the diamond symbols “ \diamond ” in Fig. 7 shows the PETbox4 mouse imaging conditions, including the imaging chamber, with an energy resolution of 18% and with no backscatter rejection implemented. The NECR increases by 13% as the LLD increases from 150 keV to 400 keV, primarily due to the reduced SF. The NECR decreases as the LLD increases from 400 keV to 450 keV due to the exclusion of trues in the photopeak. The SF decreases by 85% as the LLD increases from 150 to 450 keV.

2) *Identification of Backscatter Events:* The curve represented by the cross sign symbols “ \times ” in Fig. 7 shows the simple event classification as most commonly used [9], [14], [25] based on the same data set, which excludes step 5, 6 and 7 in Fig. 4 and does not identify backscatters.

Without the appropriate classification in the simulation, backscatter events (including backscatter multiples, single photon backscatters and pile-up events) are inaccurately categorized as trues. Although the total count rate of these backscatter events is much lower than the count rate of the trues (for a LLD of 150 keV, the backscatter events are about 14.6% of the trues), the NECR is proportional to the square of the trues count rate. Therefore, a 14.6% overestimation of trues count rate leads to a 31% overestimation of the NECR. As a result, the NECR calculated at 150 keV LLD based on this misclassification is 17% higher than that at a LLD of 400 keV, leading to a different (and inaccurate) optimization. This result highlights the importance of the methodology described in this work regarding the treatment of event interactions in simulations.

3) *Backscatter Rejection:* The curve represented by the square box symbols “ \square ” in Fig. 7 shows the NECR and SF derived from the same dataset as for the diamond “ \diamond ” data based on a perfect backscatter rejection assumption by arbitrarily setting all the backscatter events to zero. This represents an

idealized performance that can be achieved with the rejection. With the perfect backscatter rejection, the NECR and SF are improved for LLDs lower than 300 keV due to suppressed SF. However, object scatter still dominates the degradation of image quality when employing a wide open energy window. At a LLD of 400 keV, the NECR still reaches its maximum value and the SF decreased by 71% from that at a LLD of 150 keV. The result with the perfect backscatter rejection leads to the same optimized LLD of 400 keV as for the result with no backscatter rejection implemented (diamond “ \diamond ” data). Moreover, the backscatter rejection shows almost no improvement on NECR and SF at the optimized LLD of 400 keV, as almost all the backscatter events have already been eliminated through the energy discrimination. As a conclusion, the backscatter rejection is not helpful and will not be developed for the PETbox4 system.

We need to point out here that the simulations and experiments performed throughout this work focused on pure positron emitting sources. In situations where high energy gammas are emitted simultaneously with the positrons, this conclusion regarding backscatter rejection will likely need to be revisited.

4) *Effect of the Imaging Chamber:* The curve represented by the circle symbols “ \circ ” in Fig. 7 shows the simulation excluding the imaging chamber and with an energy resolution of 18%. Backscatter events were identified and included. Compared to the diamond “ \diamond ” data, the NECR increases by 21% and 10%, and the SF decreases by about 17% and 26% respectively for the circle “ \circ ” data at the LLDs of 150 and 400 keV. The optimized LLD is still 400 keV. Therefore, future efforts are desired to reduce the attenuation introduced by the imaging chamber if possible. The circle “ \circ ” data representing the lower limit for the chamber scatters also indicates that decreasing imaging chamber material will not change our conclusion on optimized energy window.

5) *Effect of the Energy Resolution:* The curve represented by the triangle symbols “ Δ ” in Fig. 7 shows the simulation with an energy resolution of 30% as a worst case scenario to evaluate the effect of the poorer energy resolution in a more realistic scanner on imaging performance. Backscatter events were identified and included, and the imaging chamber was simulated. The NECR decreases significantly when the LLD is raised from 350 keV to 450 keV, because in a poorer energy resolution system, a large fraction of true photopeak events is detected between 350 and 450 keV. Under this scenario, these photoelectric events are discarded as falling outside the appropriate energy window when the LLD is raised above 350 keV. As a result, the optimal LLD with the maximum NECR for this poorer energy resolution system decreased to 350 keV, instead of the 400 keV optimal LLD when an 18% energy resolution is available. In the PETbox4 system described in [5], the energy resolution ranges from 13.5% to 48.3%, therefore the implemented threshold needs to provide tolerance for variance of different components such as PMT, scintillation block positioning and coupling. Therefore, 350 keV was proposed as the optimized LLD for the current PETbox4 system. The triangle “ Δ ” data also indicates that a more uniform energy resolution which can improve both NECR and SF is desired for the PETbox4 system in the future if possible.

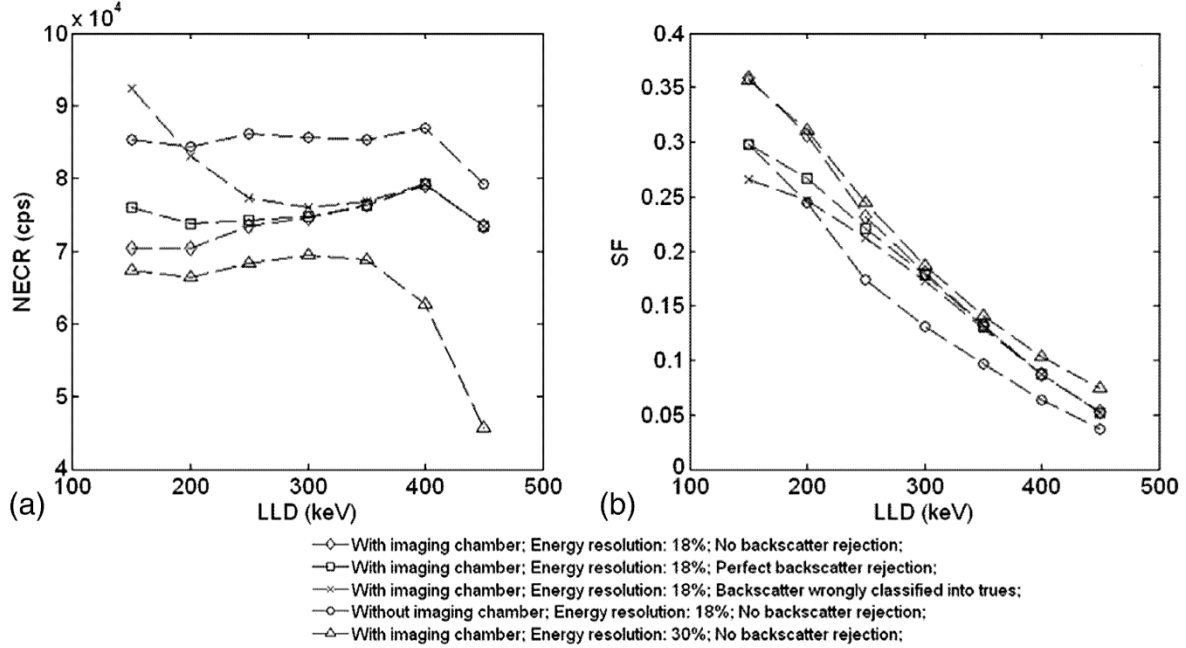


Fig. 7. NECR (a) and SF (b) as a function of LLD for five different configurations: “◇”, “□” and “×” data were calculated from the same simulation dataset with different analysis on the backscatter events. “○” represents a different simulation excluding the imaging chamber. “△” represents a different simulation assuming an energy resolution of 30%.

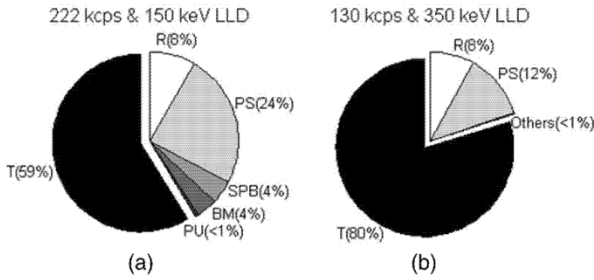


Fig. 8. The fraction occupied by different types of events in prompts for the open energy window of 150-650 keV (a) and the optimized energy window of 350-650 keV (b): trues (T), pile-ups (PU), backscattered multiples (BM), single photon backscatters (SPB), phantom scatters (PS) and randoms (R). Detector backscatter events are virtually eliminated at a LLD of 350 keV.

The fraction occupied by different types of events in prompt coincidences for the open energy window of 150-650 keV (the previous default energy window used in [5]) and the optimized energy window of 350-650 keV are shown in Fig. 8.

C. NEMA NU-4 Image Quality Phantom

Table II summarizes the uniformity and SOR measured from the image quality phantom images with the LLD increasing from 150 keV to 350 keV in 50 keV steps. Fig. 9 shows the profiles across the cold chamber region of the reconstructed NEMA NU-4 image quality phantom images at a LLD of 150 keV and 350 keV. With the ML-EM reconstruction, the percent standard deviation (SD) in the uniform region is 6.0% and 5.8%, the SOR for the water chamber decreases by about 45% from 15.1% to 8.3%, and the SOR for the air chamber decreases by 31% from

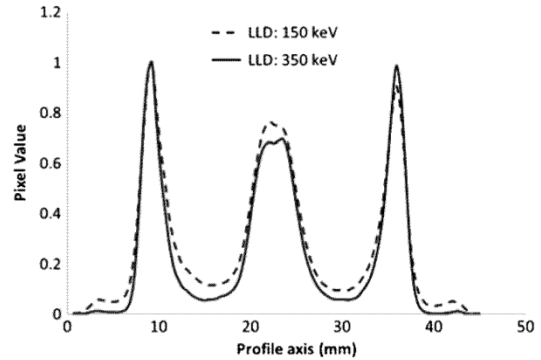


Fig. 9. Profiles across the cold chamber region of the reconstructed NEMA NU-4 image quality phantom images at a LLD of 150 keV and 350 keV.

TABLE II
UNIFORMITY AND SOR FOR THE COLD CHAMBERS FILLED WITH AIR AND WATER OF THE NEMA NU-4 IMAGE QUALITY PHANTOM IMAGES ACQUIRED WITH DIFFERENT LLDs

LLD (keV)	Uniformity	SOR (air)	SOR (water)
150	6.0%	0.120 ± 0.020	0.151 ± 0.031
200	5.9%	0.105 ± 0.019	0.126 ± 0.028
250	5.9%	0.101 ± 0.018	0.115 ± 0.026
300	5.7%	0.094 ± 0.018	0.101 ± 0.022
350	5.8%	0.083 ± 0.016	0.083 ± 0.019

12.0% to 8.3% for the LLD of 150 and 350 keV, respectively. Furthermore, the water and air chamber have identical SORs

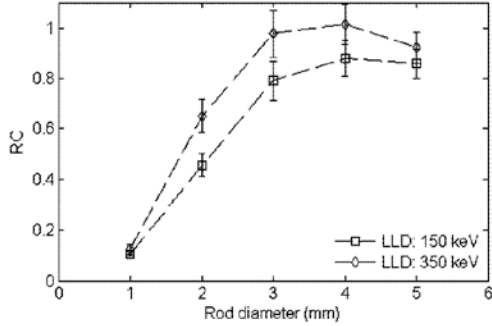


Fig. 10. RCs and SDs for five rods of different sizes with the open energy window of 150-650 keV and the optimized energy window of 350-650 keV.

at the optimized LLD of 350 keV. The RCs for five different rod sizes from 1 to 5 mm diameter at a LLD of 150 keV and 350 keV are shown in Fig. 10. The overall RC at the LLD of 350 keV is better than that at the LLD of 150 keV. Results from the physical measurement further support the simulation based optimization. No scatter correction was applied for the image quality phantom images.

IV. DISCUSSION

Decreasing the inner diameter and increasing the axial FOV of the scanner provides larger detectable solid angle and higher sensitivity for PET systems. The compromise of the spatial resolution due to depth of interaction (DOI) effects introduced by crystal penetration when employing close geometry has been significantly improved with DOI detector techniques [28]–[32] and iterative image reconstruction with more accurate system response modeling [33], [34]. This has led to an increased popularity of systems with close geometry and large solid detection angle [5]–[10], [35]. Even for clinical systems, longer axial FOV scanners are currently in the design stage [36]. Therefore, accurate investigation and understanding of the system characteristics introduced by the close geometry are of great importance to guide system design and optimize data acquisition protocols.

In this work, a system that utilizes BGO as a scintillator is described. The choice of scintillator material is beyond the scope of this effort, but it has been shown previously [5], [37] that this high effective atomic number scintillator offers some advantages in system sensitivity and reduced intercrystal scatter. Nevertheless, the results of this work are applicable to other closed geometry imaging systems made from different scintillator materials.

In this study, an 18.2 g mouse was selected to generate the voxelized phantom in GATE, representing the lower limit of the object scatter originated from the mouse. The simulation which excludes the imaging chamber (shown by the circle “o” data in Fig. 7) thus represents the lower limit of the overall object scatter in PETbox4. Even in such an extreme case, the NECR and SF degrade as the LLD decreases mainly due to the large fraction of object scatter events included. Therefore, the proposed optimized energy window of 350-650 keV should be applicable for imaging any mouse with a larger size or using dif-

ferent imaging chambers in PETbox4. As only attenuation material inside the FOV was modeled in this study, and the detector material employed by the PETbox4 is BGO, a non-intrinsic radioactive scintillator, the studies in this paper represent the lower limit of the influence from environment scatter and intrinsic activity. The more narrow optimized energy window will also be valid if surrounding gantry material is included or detectors with intrinsic activity such as lutetium oxyorthosilicate (LSO) are used, both of which further degrade the NECR and SF [13]. The NEMA NU-4 count rate phantom and its associated methodology are not used in this study, because traditional sinograms are not generated from the PETbox4 that employs an unconventional system geometry [27].

Our conclusion is different from the results reported for mouse imaging in conventional large diameter systems, in which the optimized NECR can be achieved at a wide open energy window, and the object SF is much less sensitive to the change of the LLD [13], [14]. This difference emphasizes the strong dependence of the SF on scanner geometry: the larger distance between the location for scattering and detection in a scanner with a larger diameter, results in a more significant misplacement of the LOR for the same scattering angle. As a result, a larger fraction of mis-positioned LORs falls out of the FOV and will not contribute to the degradation of the image. For a close geometry system, most of the scatter LORs intersect the FOV leading to a dominant factor of the degradation of NECR and SF when employing an open energy window. Therefore, optimization of the imaging protocol in accordance to the specific scanner is necessary.

This study also highlights that crystal backscatter events cannot be neglected for a large detection solid angle system such as PETbox4. As shown in Fig. 8, the backscatter events occupy about 9% of the total prompts at a LLD of 150 keV, compared with 24% for phantom SF and a random events fraction of 8%. In most of the previous studies involving event classification in GATE [9], [14], [25], only phantom scatter and random events were identified based on *eventID* and *ComptonPhantom* provided by *Root* output from GATE. Ignoring backscatter events results in overestimation of the NECR and underestimation of the SF derived from the simulation (as shown by the cross sign “x” data in Fig. 7), which may bias the conclusion in system design.

In this study, NECR and SF were examined as the criteria for optimization. While correlation between NECR and signal-to-noise ratio (SNR) has been experimentally demonstrated for 3D PET, such work has, to date, been performed only on systems with conventional geometries [38]. Direct correlation between NECR and image SNR has not been validated for longer axial FOV and box like geometry scanners such as PETbox4. Nevertheless, the results from the reconstructed images lead to satisfactory agreement with our simulation based optimization. SF is also an important measure of overall error in PET due to the misplacement of the LORs. A higher SF leads to degradation of SOR, RC and target-to-background ratio (TBR) as the spill-out of counts cannot be compensated by the spill-in of counts, and decrease of the NECR and SNR of the reconstructed images. Contrast-to-noise ratio (CNR), as a more comprehensive figure of merit accounting for the influence from both NECR and SF,

is strongly related to the lesion detectability, target localization and quantification accuracy of a system [39]–[41] and could perhaps be considered as part of protocol optimization and system design. While the choice of the LLD on NECR and SF have been discussed separately in this work, it is essential to understand the simultaneous effects and tradeoff of the changes of NECR and SF on CNR, as future investigation.

V. CONCLUSION

In this work, the energy window of PETbox4 for whole body mouse scans has been optimized using GATE simulations. The event type classification described in this paper provides a more accurate methodology and is important for imaging protocol optimization and system evaluation. For the pure positron emitting source investigated here, backscatter rejection did not prove useful and therefore was not developed for the PETbox4 system. An LLD of 350 keV was proposed as the optimized energy threshold. Analysis of the NEMA image quality phantom images further support the simulation based optimization. Due to the importance of object scatter and the significant differences of NECR and SF from the simulation with and without imaging chamber, it is concluded that reduction in attenuation introduced by the imaging chamber should be pursued. Furthermore, decreasing imaging chamber material will not change our conclusion on optimized energy window. The optimization in this study is not limited to PETbox4, but should also be applicable or helpful to other close geometry scanners [6]–[10].

APPENDIX

The interaction history of each particle in each coincidence event is investigated by the event classification algorithm at eight steps, as shown below:

- 1) *Energy discrimination*: The *energy* variable for each detection in a coincidence event is extracted from the coincidence tree of the *Root* output. Events will be rejected if any of the recorded *energies* fall out of the predefined energy window.
- 2) *Check if the LOR intersects the FOV*: The distance from projection of the LOR on the transaxial plane to the center of the transaxial FOV is calculated based on the *rsectorID* and *crystalID* of each detection from the coincidence tree. LORs falling out of the FOV will be rejected.
- 3) *Randoms*: The *eventID* of the two detections from the coincidence tree are compared. Coincidence events with different *eventID* will be classified into randoms.
- 4) *Phantom scatter*: If any of the two detections has a *comptonPhantom* (from the coincidence tree) higher than zero, the coincidence event will be classified into phantom scatter.
- 5) *Single photon backscatter*: Based on the *eventID* retrieved from the coincidence tree, all the hits with the same *eventID* in the hits tree of the *Root* output are examined for *photonID*. If only one *photonID* is recorded, the event will be classified into single photon backscatters.
- 6) *Backscattered multiples*: Based on the *eventID* retrieved from the coincidence tree, all the hits with the same *eventID* in the hits tree of the *Root* output are examined for *rsectorID* and *photonID* to determine the detector (*rsectorID*) that each of annihilation photon first hits. If the two *rsectorIDs* extracted from the coincidence tree for a coincidence event are different from the *rsectorIDs* of the first hits, the coincidence event will be classified into backscatter multiples.
- 7) *Pile-ups*: The *rsectorID* and *eventID* for each of the two detections in the coincidence event can be extracted from the coincidence tree, based on which the *photonID* of all the hits with the same *rsectorID* and *eventID* from the hits tree are examined. If more than one *photonID* are found for certain *rsectorID* and *eventID*, the coincidence event will be classified into pile-up events.
- 8) *Trues*: The coincidence events that pass through the previous seven steps will be identified as trues.

ACKNOWLEDGMENT

The authors would like to thank the staff of the Crump Imaging facility at UCLA including W. Ladno, D. Williams, and J. Collins for their assistance with obtaining the ^{18}F solution for this study.

REFERENCES

- [1] M. E. Phelps, "Positron emission tomography provides molecular imaging of biological processes," *Proc. Natl. Acad. Sci. USA*, vol. 97, pp. 9226–33, Aug. 1, 2000.
- [2] R. Myers, "The biological application of small animal PET imaging," *Nucl. Med. Biol.*, vol. 28, pp. 585–593, Jul. 2001.
- [3] S. S. Gambhir, H. R. Herschman, S. R. Cherry, J. R. Barrio, N. Satyamurthy, and T. Toyokuni *et al.*, "Imaging transgene expression with radionuclide imaging technologies," *Neoplasia*, vol. 2, pp. 118–138, Jan.-Apr. 2000.
- [4] A. F. Chatzioannou, "Molecular imaging of small animals with dedicated PET tomographs," *Eur. J. Nucl. Med.*, vol. 29, pp. 98–114, Jan. 2002.
- [5] Z. Gu, R. Taschereau, N. T. Vu, H. Wang, D. L. Prout, and R. W. Silverman *et al.*, "NEMA NU-4 performance evaluation of PETbox4, a high sensitivity dedicated PET preclinical tomograph," *Phys. Med. Biol.*, vol. 58, pp. 3791–3814, Jun. 7, 2013.
- [6] H. Zhang, Q. Bao, N. T. Vu, R. W. Silverman, R. Taschereau, and B. N. Berry-Pusey *et al.*, "Performance evaluation of PETbox: A low cost bench top preclinical PET scanner," *Mol. Imaging Biol.*, vol. 13, pp. 949–61, Oct. 2011.
- [7] G. Alexandrakis, F. R. Rannou, and A. F. Chatzioannou, "Tomographic bioluminescence imaging by use of a combined optical-PET (OPET) system: A computer simulation feasibility study," *Phys. Med. Biol.*, vol. 50, pp. 4225–41, Sep. 7, 2005.
- [8] M. Rodriguez-Villafuerte, Y. Yang, and S. R. Cherry, "A Monte Carlo investigation of the spatial resolution performance of a small-animal PET scanner designed for mouse brain imaging studies," *Phys. Med.*, vol. 30, pp. 76–85, Feb. 2014.
- [9] G. Stortz, M. D. Walker, C. J. Thompson, A. L. Goertzen, F. Retiere, and X. Zhang *et al.*, "Characterization of a New MR compatible small animal PET scanner using Monte-Carlo simulations," *IEEE Trans. Nucl. Sci.*, vol. 60, no. 3, pp. 1637–1644, Jun. 2013.
- [10] P. Vaska, C. L. Woody, D. J. Schlyer, S. Shokouhi, S. P. Stoll, and J. F. Pratte *et al.*, "RatCAP: Miniaturized head-mounted PET for conscious rodent brain imaging," *IEEE Trans. Nucl. Sci.*, vol. 51, no. 5, pp. 2718–2722, Oct. 2004.
- [11] S. R. Cherry, Y. Shao, R. W. Silverman, K. Meadors, S. Siegel, and A. Chatzioannou *et al.*, "MicroPET: A high resolution PET scanner for imaging small animals," *IEEE Trans. Nucl. Sci.*, vol. 44, no. 3, pp. 1161–1166, Jun. 1997.
- [12] Y. C. Tai, A. Ruangma, D. Rowland, S. Siegel, D. F. Newport, and P. L. Chow *et al.*, "Performance evaluation of the microPET focus: A third-generation microPET scanner dedicated to animal imaging," *J. Nucl. Med.*, vol. 46, pp. 455–463, Mar. 2005.
- [13] Y. F. Yang and S. R. Cherry, "Observations regarding scatter fraction and NEC measurements for small animal PET," *IEEE Trans. Nucl. Sci.*, vol. 53, no. 1, pp. 127–132, Feb. 2006.

- [14] A. Konik, M. T. Madsen, and J. J. Sunderland, "GATE simulations of human and small animal PET for determination of scatter fraction as a function of object size," *IEEE Trans. Nucl. Sci.*, vol. 57, no. 5, pp. 2558–2563, Oct. 2010.
- [15] F. Zagni, D. D'Ambrosio, A. E. Spinelli, G. Ciorica, S. Fanti, and M. Marengo, "Accurate modeling of a DOI capable small animal PET scanner using GATE," *Appl. Radiat. Isot.*, vol. 75, pp. 105–114, May 2013.
- [16] Y. F. Yang, Y. C. Tai, S. Siegel, D. F. Newport, B. Bai, and Q. Z. Li *et al.*, "Optimization and performance evaluation of the microPET II scanner sensitivity: Relating countrates to image signal-to-noise ratios using noise equivalent counts," *IEEE Trans. Nucl. Sci.*, vol. 37, no. 4, pp. 783–788, Apr. 1990.
- [17] A. L. Goertzen, "Coincidences originating from a single photon: An unrecognized and potentially significant source of scatter in small animal PET?," in *Proc. IEEE Nucl. Sci. Symp. Conf. Rec.*, Oct. 2009, pp. 2888–91.
- [18] S. Jan, G. Santin, D. Strul, S. Staelens, K. Assie, and D. Autret *et al.*, "GATE: A simulation toolkit for PET and SPECT," *Phys. Med. Biol.*, vol. 49, pp. 4543–4561, Oct. 7, 2004.
- [19] S. Agostinelli, J. Allison, K. Amako, J. Apostolakis, H. Araujo, and P. Arce *et al.*, "GEANT4-a simulation toolkit," *Nucl. Instrum. Meth. A*, vol. 506, pp. 250–303, Jul. 1, 2003.
- [20] J. Allison, K. Amako, J. Apostolakis, H. Araujo, P. A. Dubois, and M. Asai *et al.*, "Geant4 developments and applications," *IEEE Trans. Nucl. Sci.*, vol. 53, no. 1, pp. 270–278, Feb. 2006.
- [21] "Performance measurements of small animal positron emission tomographs," Rosslyn, VA: Standards Publication NU 4-2008 2008, National Electrical Manufacturers Association.
- [22] R. Brun and F. Rademakers, "ROOT - An object oriented data analysis framework," *Nucl. Instrum. Meth. A*, vol. 389, pp. 81–86, Apr. 11, 1997.
- [23] H. K. Wang, D. B. Stout, R. Taschereau, Z. Gu, N. T. Vu, and D. L. Prout *et al.*, "MARS: A mouse atlas registration system based on a planar x-ray projector and an optical camera," *Phys. Med. Biol.*, vol. 57, pp. 6063–6077, Oct. 7, 2012.
- [24] G. Santin, D. Strul, D. Lazaro, L. Simon, M. Krieguer, and M. V. Martins *et al.*, "GATE: A Geant4-based simulation platform for PET and SPECT integrating movement and time management," *IEEE Trans. Nucl. Sci.*, vol. 50, no. 5, pp. 1516–1521, Oct. 2003.
- [25] G. Delso, M. J. Martinez, I. Torres, R. Ladebeck, C. Michel, and S. Nekolla *et al.*, "Monte Carlo simulations of the count rate performance of a clinical whole-body MR/PET scanner," *Med. Phys.*, vol. 36, pp. 4126–35, Sep. 2009.
- [26] R. Taschereau, F. R. Rannou, and A. F. Chatzioannou, "A modeled point spread function for a noise-free system matrix," in *Proc. IEEE Nucl. Science Symp. Med. Imag. Conf.*, Oct. 2011, pp. 4102–5.
- [27] N. Zhang, C. J. Thompson, F. Cayouette, D. Jolly, and S. Kecani, "A prototype modular detector design for high resolution positron emission mammography imaging," *IEEE Trans. Nucl. Sci.*, vol. 50, pp. 1624–1629, Oct. 2003.
- [28] T. Tsuda, H. Murayama, K. Kitamura, T. Yamaya, E. Yoshida, and T. Omura *et al.*, "A four-layer depth of interaction detector block for small animal PET," *IEEE Trans. Nucl. Sci.*, vol. 51, pp. 2537–2542, Oct. 2004.
- [29] Y. F. Yang, P. A. Dokhale, R. W. Silverman, K. S. Shah, M. A. McClish, and R. Farrell *et al.*, "Depth of interaction resolution measurements for a high resolution PET detector using position sensitive avalanche photodiodes," *Phys. Med. Biol.*, vol. 51, pp. 2131–2142, May 7, 2006.
- [30] Y. H. Chung, Y. Choi, G. Cho, Y. S. Choe, K. H. Lee, and B. T. Kim, "Optimization of dual layer phoswich detector consisting of LSO and LuYAP for small animal PET," *IEEE Trans. Nucl. Sci.*, vol. 52, pp. 217–221, Feb. 2005.
- [31] M. C. Maas, D. R. Schaart, D. J. van der Laan, P. Bruyndonckx, C. Lemaire, and F. J. Beekman *et al.*, "Monolithic scintillator PET detectors with intrinsic depth-of-interaction correction," *Phys. Med. Biol.*, vol. 54, pp. 1893–1908, Apr. 7, 2009.
- [32] T. Yamaya, N. Hagiwara, T. Obi, M. Yamaguchi, K. Kita, and N. Ohyama *et al.*, "DOI-PET image reconstruction with accurate system modeling that reduces redundancy of the imaging system," *IEEE Trans. Nucl. Sci.*, vol. 50, pp. 1404–1409, Oct. 2003.
- [33] K. M. Champley, L. R. MacDonald, T. K. Lewellen, R. S. Miyaoka, and P. E. Kinahan, "DOI-based reconstruction algorithms for a compact breast PET scanner," *Med. Phys.*, vol. 38, pp. 1660–1671, Mar. 2011.
- [34] A. L. Goertzen, Q. N. Bao, M. Bergeron, E. Blankemeyer, S. Blinder, and M. Canadas *et al.*, "NEMA NU 4-2008 Comparison of Preclinical PET Imaging Systems," *J. Nucl. Med.*, vol. 53, pp. 1300–1309, Aug. 2012.
- [35] J. K. Poon, M. L. Dahlbom, W. W. Moses, K. Balakrishnan, W. Wang, and S. R. Cherry *et al.*, "Optimal whole-body PET scanner configurations for different volumes of LSO scintillator: A simulation study," *Phys. Med. Biol.*, vol. 57, pp. 4077–94, Jul. 7, 2012.
- [36] Q. Bao and A. F. Chatzioannou, "GATE simulation of a BGO based high sensitivity small animal PET scanner," in *Proc. Noninvasive Functional Source Imaging of the Brain and Heart & Int. Conf. Functional Biomedical Imaging*, Oct. 2007, pp. 47–50.
- [37] M. Dahlbom, C. Schiepers, and J. Czernin, "Comparison of noise equivalent count rates and image noise," *IEEE Trans. Nucl. Sci.*, vol. 52, no. 5, pp. 1386–1390, Oct. 2005.
- [38] C. Lartzien, P. E. Kinahan, R. Swensson, C. Comtat, N. Lin, and V. Villemagne *et al.*, "Evaluating image reconstruction methods for tumor detection in 3-dimensional whole-body PET oncology imaging," *J. Nucl. Med.*, vol. 44, pp. 276–290, Feb. 2003.
- [39] C. Lartzien, P. E. Kinahan, and C. Comtat, "Volumetric model and human observer comparisons of tumor detection for whole-body positron emission tomography," *Acad. Radiol.*, vol. 11, pp. 637–648, Jun. 2004.
- [40] M. Brambilla, R. Matheoud, C. Secco, G. Sacchetti, S. Comi, and M. Rudoni *et al.*, "Impact of target-to-background ratio, target size, emission scan duration, and activity on physical figures of merit for a 3D LSO-based whole body PET/CT scanner," *Med. Phys.*, vol. 34, pp. 3854–65, Oct. 2007.

Chapter 4

System Optimization:

A New Pileup Rejection Method based on Position Shift Identification

Chapter 4 System Optimization: Pileup Rejection

4.1 Introduction

Pulse pileup is a common problem in multiplexed scintillator detectors readout by resistor divider networks. Pileup events cause event loss and mis-positioning [1], energy spectrum distortion [2] and reduced timing resolution [3], leading to a deterioration of signal-to-noise ratio (SNR), a loss of resolution and contrast and introduction of image artifacts in PET images. Many efforts have been devoted to pileup event correction [2, 4-6]. Most of these methods focus on identifying and recovering the information of each single event in a multi-event pileup by pulse-tail extrapolation [2, 5] or pulse waveform reconstruction [6]. These methods have been demonstrated to maintain a much better linear relationship between activity and count rate, and extend the dynamic range of the detector. The first step of these methods is to identify the pileup events. Leading edge discriminator was commonly used to monitor the incoming signal and detect pileup events before the pileup event recovery [5, 6].

PETbox4 is a bench top PET scanner dedicated to high sensitivity and high resolution imaging of mice designed and built at our institute [7]. The high absolute sensitivity of PETbox4, together with the long decay time of BGO used as the detector material and the highly multiplexed electronics lead to a significant fraction of pileup, reached at lower total activity for this scanner, than for comparable instruments. Therefore, it is important to implement pileup event correction for PETbox4. For conventional scintillator based PET detectors, the signal intensity output from a detector is related to the number of the scintillation light photons (signal information carrier) detected per unit time. Due to the low light output and long decay time of BGO, the signal intensity of the PETbox4 detector is much lower than those using higher light output and faster scintillators such as LSO, resulting in larger statistical variations in the signal

waveforms of the PETbox4 detectors. Because the conventional leading edge rejection (LER) method identifies and rejects the pileup events by monitoring the shape of individual pulse waveforms, the higher level noise in the PETbox4 detector pulse leads to erroneous rejection and loss of sensitivity when LER is used.

In this manuscript, a novel pileup rejection method named position shift rejection (PSR) is introduced. The PSR method is aimed at accurate discrimination of pileup events for rejection. The performance of PSR is compared with the results acquired by the conventional LER method and with no pileup rejection implemented (NoPR). A comprehensive digital pulse library was developed for objective evaluation and optimization of the PSR and LER methods.

4.2 Methods

4.2.1 Pileup in PETbox4

PETbox4 is a dedicated preclinical PET tomograph developed at the Crump Institute for Molecular Imaging, at UCLA [8]. Each PETbox4 detector panel consists of a 24×50 pixelated BGO scintillator array with individual crystals measuring $1.82 \times 1.82 \times 7$ mm and a pitch of 1.90 mm (Proteus, Chagrin Falls, OH). The BGO array is coupled to two H8500 position-sensitive photomultiplier tubes (PSPMT; Hamamatsu Photonics, Bridgewater, NJ) for scintillation light detection. A charge division resistor network [9] is used to convert the 128 anode outputs from the two PSPMTs into two position encoding signals, denoted as x and y , and the sum of the PSPMT outputs, denoted as sum .

The x , y position signals and the sum energy signal are digitized by free running analogue-to-digital converters (ADC) and accumulated in an field programmable gate array (FPGA) with an integration period of 3τ for collecting about 95% of the scintillation light, where τ is the decay time constant of the scintillation pulse. Event positions are calculated as $X=x/sum$

and $Y=y/sum$ by the event position logic. Figure 4.1 shows a simplified block diagram of the event positioning scheme in PETbox4.

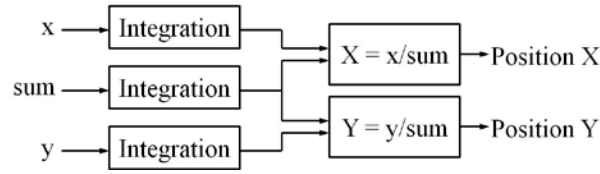


Figure 4.1. Block diagram of the PETbox4 event positioning algorithm.

A typical scintillation pulse (*sum*) from the PETbox4 detector is shown in Figure 4.2 (a). When two or more annihilation photons hit a detector within one integration period, a pileup event is formed by involving the superposition of the new pulses on the long duration tail from a preceding pulse, as shown in Figure 4.2 (b). In this work, a pulse is defined as a pileup event, if the adjacent events are separated by less than 0.9 μsec (due to the 0.3 μsec decay time for BGO). These pileup events lead to event mispositioning, contributing to loss of contrast and image artifacts at high count rates.

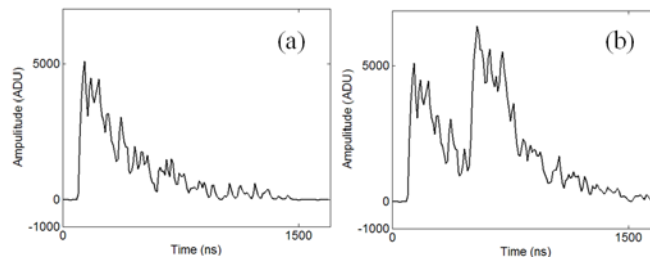


Figure 4.2. Signal waveform (sum): (a) a typical scintillation pulse; (b) a typical pileup event.

PETbox4 reaches a significant fraction of pileup at lower total activity than that for comparable instruments, mainly due to its high absolute sensitivity, together with the long decay time of BGO and the highly multiplexed detector readout. The Geant4 application for tomographic emission (GATE) Monte Carlo simulation software [10] was used to simulate the data acquired with a PETbox4 detector. A point source with isotropic emission of back-to-back

511 keV gamma photons was positioned 2.5 cm from the front surface of the PETbox4 detector, mimicking the emission from the center of the field of view (FOV) of the PETbox4 system. The time stamps for individual events were extracted, based on which the fractions of pileup events at different activity levels were calculated, as shown in Table 4.1.

Table 4.1. Fractions of pileup events at different activity levels

Activity	0.2 μ Ci	10 μ Ci	30 μ Ci	50 μ Ci
% of pileup	0.22	11.46	31.75	47.42

4.2.2 Pulse leading edge rejection (LER) method

LER is a conventional pileup rejection method that detects pileup events by continuously taking the derivative of the incoming signal waveform for identifying the pulse leading edge. The derivative of the pulses shown in Figure 4.2 (a) and (b) are shown in Figure 4.3 (a) and (b), respectively. In Figure 4.3 (a), the value of the derivative remains below the preset threshold within the 3τ event processing time (0.9 μ sec), and this event is identified as a non-pileup event. Due to the leading edge of the second pulse which superimposes on the tail from the preceding pulse as shown in Figure 4.2(b), the value of the derivative in Figure 4.3 (b) exceeds the threshold within the event processing time, thus these events are identified as pileup events.

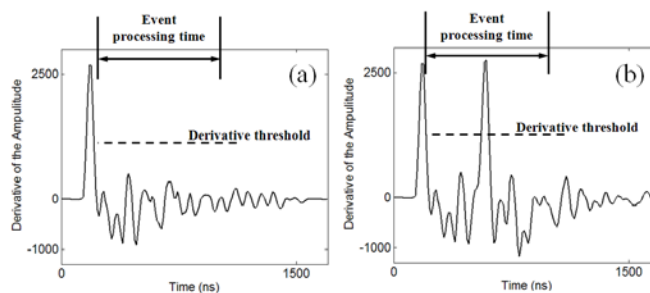


Figure 4.3. (a): the derivative of the scintillation pulse shown in Figure 4.2 (a); (b): the derivative of the pileup pulse shown in Figure 4.2 (b).

4.2.3 Position shift rejection (PSR) method

Our new pileup rejection method PSR is based on the detection of position shifts on event location as the signal is being integrated by comparing positions obtained with different integration times, as shown in Figure 4.4, where I_t corresponds to the position obtained with an integration time of t ns. Figure 4.5 (a) and (b) shows the X position as a function of the integration time derived from the pulses shown in Figure 4.2 (a) and (b). In Figure 4.5 (a), the X position value converges quickly to a relative stable value within the 3τ event processing time (0.9 μsec), and this event is identified as a non-pileup event. In contrast, an obvious position shift can be observed in Figure 4.5 (b) due to the event pileup shown in Figure 4.2(b). As a result, the difference between the values of I_{200} and I_{600} shown in Figure 4.4 exceeds the threshold 2, thus these events are correctly identified as pileup events.

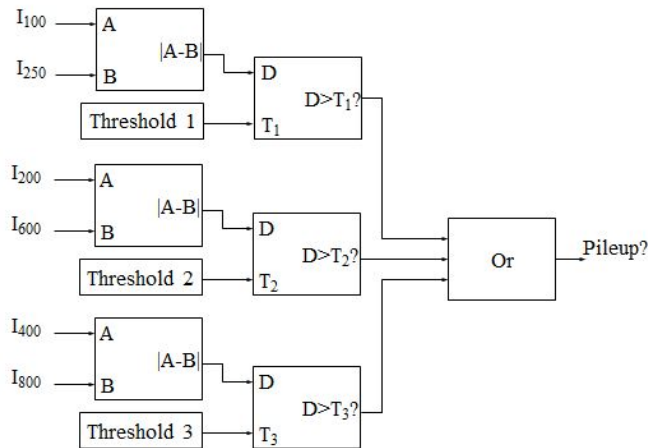


Figure 4.4. Position shift identification based pileup rejection scheme.

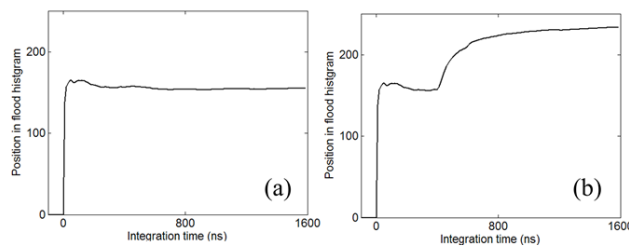


Figure 4.5. Position in arbitrary units obtained with different integration time: (a) a typical scintillation pulse; (b) a typical pileup pulse.

4.2.4 Synthetic pulse train evaluation

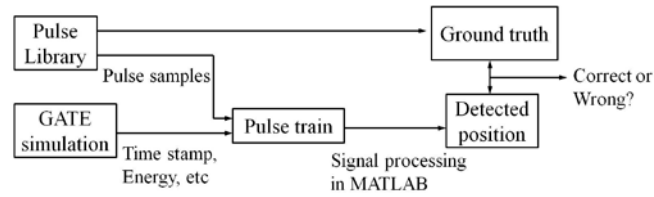


Figure 4.6. Synthetic pulse train evaluation flow chart

The PETbox4 system employs a free running ADC and FPGA based digital signal processing board (VHS-ADC, Nutaq, Quebec City, Quebec), which makes it possible to digitize and acquire the entire pulse waveform with adequate resolution in both time and amplitude, and compute pulse parameters of interest in real time. To develop digital signal processing algorithms for the PETbox4 system, a comprehensive digital pulse library was generated from physical measurements by directly triggering and recording raw pulse signals from the PETbox4 detectors, at the same precision as the signals to be processed in the FPGA. As a result, the use of these recorded pulses for offline evaluation of signal processing algorithms should lead to equivalent results as those yielded from real-time, online FPGA processing. The pulse library should be composed by a series of single pulses without pileup. As shown in Table 4.1, singles measured with a 0.2 μCi point source only include 0.22% pileup events. Therefore, a 7.4 kBq (0.2 μCi) ^{68}Ge point-like source (Eckert & Ziegler Isotope Products, Valencia, CA) was used to acquire the data for establishing the pulse library. The pulse library used in this work contained 62500 events, with 3 pulses per event including the x , y position encoding signals and the *sum* signal output from a PETbox4 detector multiplexed by a resistor divider network. The sample size of the pulse library can be easily enlarged.

The effectiveness of the LER and PSR methods was evaluated and compared with the help of the pulse library. 1000 single events including the *sum*, x and y signals were randomly

selected from the pulse library and placed into a synthetic pulse train based on timestamps and energy obtained from the GATE simulation, as shown in Figure 4.6. The simulation was performed with the NEMA NU-4 scatter fraction phantom (mouse size) [11] filled with 50 μCi of F^{18} . The synthetic pulse train was fed into the signal processing algorithms in MATLAB, and the positions of detected events were extracted and compared with the known position information from the pulse library as the ground truth reference. The average area for one crystal in the flood histogram was the tolerance criterion for the identification of a detected position as accurate.

4.2.5 Measurement verification

1) *Flood image and energy spectra:* To validate the synthetic pulse train results, physical measurements were performed in the PETbox4 system. Flood images for one detector panel were acquired with a cylinder source which was filled with 50 μCi of ^{18}F measured with a dose calibrator (Atomlab 300; Biodex Medical Systems, Shirley, NY) and placed at the center of the FOV. Pileup events detected by the LER and PSR methods were labeled and included in the list mode files. Flood histograms for the entire detector, as well as energy spectra from selected crystals consisting of identified pileup events and non-pileup events were extracted for comparison.

2) *System peak sensitivity:* To evaluate the potential sensitivity loss caused by either the LER or the PSR methods, the system peak absolute sensitivity of the PETbox4 was measured with NoPR, LER or PSR applied. Pileup events detected by LER and PSR were rejected. A ^{68}Ge point-like source (Eckert & Ziegler Isotope Products, Valencia, CA) was placed at the center of the FOV. The activity of the point source was 21 kBq (0.56 μCi) measured in a calibrated well-type gamma counter (Wallac Wizard 1480, Perkin Elmer, Shelton, CT). The activity was low

enough so that the fraction of the pileup events could be ignored (less than one percent). Delayed coincidences were subtracted from prompt events before the true coincidences were divided by the actual source activity. This ratio was corrected for the branching ratio of ^{68}Ga (0.89). The peak absolute sensitivity measurements were compared to simulated values obtained from GATE simulations with the same configurations.

3) *NEMA NU-4 image quality phantom*: To evaluate the effects of pileup rejection on reconstructed image quality, studies were performed using the NEMA NU-4 image quality phantom (Data Spectrum Corporation, Hillsborough, NC) filled with 50 μCi of ^{18}F , measured with a dose calibrator (Atomlab 300; Biodex Medical Systems, Shirley, NY). NoPR, LER and PSR methods were applied. The pileup events detected by LER and PSR were rejected. For each method, two scans were acquired, with the starting activities of 50 μCi and 4 μCi . The acquisition time was 20 minutes each. Random corrections were applied by subtracting the delayed coincidences from the prompt events. Dependent on the method and activity used to calculate and correct for the detector efficiencies and system geometry, normalization also affects image artifacts that are caused by pileup events. Therefore, and to focus on evaluating the image effects exclusively from the NoPR, LER and PSR methods, no normalization was applied. Finally, to demonstrate the imaging performance that can be achieved with the PETbox4 when the PSR method is applied at both high and low activity levels, count rate dependent normalizations, which were estimated from measurements of a cylindrical source filled with ^{18}F at 50 μCi and 4 μCi , were applied to the data acquired with PSR. The images were reconstructed by the ML-EM algorithm [12]. A 22.5-mm-diameter and 10-mm-high cylindrical volume of interest (VOI) was drawn over the center of the uniform region of the image-quality phantom.

The average concentration values in this VOI, and standard deviation (SD) were measured to estimate the noise performance and evaluate the image artifacts caused by the pileup events.

4.3 Results

4.3.1 Synthetic pulse train evaluation

Table 4.2 shows the synthetic pulse train evaluation results applied with NoPR, LER or PSR methods, for the 50 μCi source of F^{18} . With NoPR, 29% of the total detected events (141 in 487) are pileup caused mispositioned events. When using LER, the pileup caused mispositioned events decreases to 7.4% of the total detected events (24 in 324). As a tradeoff, the number of correct detections also decreases by 13% compared to that with NoPR (300 versus 346). This sensitivity loss is mainly due to the inaccurate identification of the fluctuations along the tails of the scintillation pulses as the leading edge of a pileup event. These large fluctuations result from the large statistical variations of the scintillation light signal due to the low light output and long decay time of BGO. When using PSR the fraction of mispositioned events due to event pileup decrease to 3.1% of the total detected events (11 in 348). Besides, the number of correct detections remains the same to that with NoPR (346 versus 346). Compared to LER, the new PSR yields a more effective suppression of mispositioned events, with no compromise in the fraction of correct detections.

Table 4.2. Pulse train evaluation using different methods

Methods	NoPR	LER	PSR
No. of Wrong	141	24	11
No. of Correct	346	300	346

4.3.2 Measurement verification

1) *Flood image and energy spectra*: Figures 4.7-4.9 show the measured flood images and selected crystal energy spectra acquired by NoPR, LER and PSR.

Figure 4.7 shows the results with NoPR applied. A cluster of blurred events merges towards the central area of the flood image as shown in Figure 4.7 (a). This blurred background underneath the events originating in single crystals corresponds to events mispositioned by pileup. In addition, in the crystal energy spectra at the central area of the flood image (Figure 4.7 (b)), a large fraction of counts with the energy higher than the photopeak energy can be observed, corresponding to the energy deposited from pileup events and therefore from multiple gamma interactions. These results demonstrate experimentally that a large fraction of pileup events is collected at this activity level (50 μ Ci).

Figure 4.8 shows the results with LER applied. Figure 4.8 (a) and (b) show the measured flood image and the energy spectra from one crystal, when including only the rejected events. The majority of the rejected events appear as a cluster of blurred events merging towards the central area of the flood image (Figure 4.8 (a)), corresponding to the mispositioned events caused by event pileup. In addition, a distinct pattern of events resolved by crystals is also obtained in Figure 4.8 (a), and a small photopeak is observed in Figure 4.8 (b). These events are non-pileup events that are erroneously rejected by LER. Figure 4.8 (c) and (d) shows the measured flood image and selected crystal energy spectra excluding the rejected events using LER. No obvious effect caused by pileup events is observed.

Figure 4.9 shows the results with PSR applied. In the flood image including only the pileup events identified by PSR (Figure 4.9 (a)), a blurred cluster towards the central area of the flood image can be observed with no crystals resolved. No photopeak is obtained in the crystal energy spectra including only rejected events in Figure 4.9 (b). This result demonstrates that

PSR performs more accurate rejection and avoids erroneous rejection and loss of sensitivity compared to LER in singles detection mode.

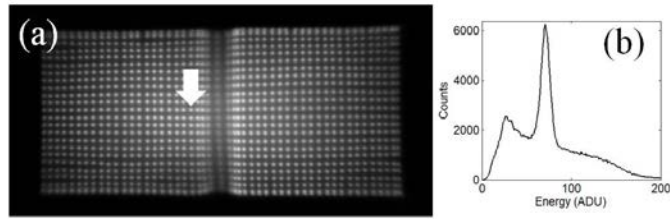


Figure 4.7. Data acquired by NoPR: (a) flood image; (b) selected crystal energy spectra. The location of the selected crystal is indicated by the arrow in the corresponding flood image.

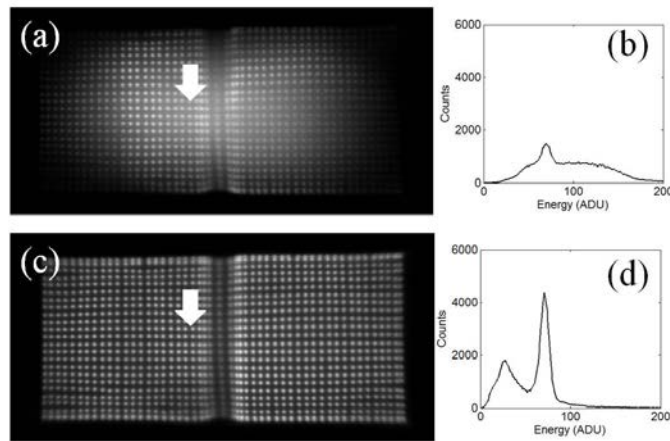


Figure 4.8. Data acquired by LER: (a) flood image and (b) selected crystal energy spectra including only rejected events; (c) flood image and (d) selected crystal energy spectra including only detected events. The location of the selected crystal is indicated by the arrow in the corresponding flood image.

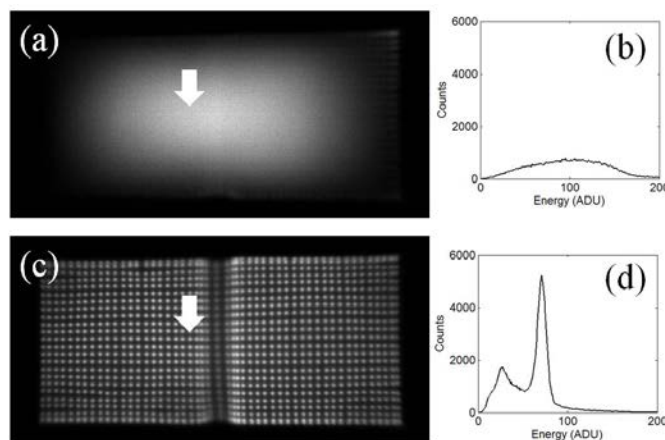


Figure 4.9. Data acquired by PSR: (a) flood image and (b) crystal energy spectra including only rejected events; (c) flood image and (d) crystal energy spectra including only detected events. The location of the selected crystal is indicated by the arrow in the corresponding flood image.

2) *System peak sensitivity*: Table 4.3 summarizes the system peak sensitivity measured using NoPR, LER and PSR methods, as well as the sensitivity estimated from the GATE simulation. The NoPR result agrees well with the GATE result, validating the simulation model. Because the activity of the measured point source was low enough so that the fraction of the pileup events can be ignored, any large decrease in sensitivity at this activity level results from the erroneous rejection of non-pileup events. Compared to about 26% sensitivity loss when the LER is applied, the sensitivity measured using PSR is in close agreement with that estimated from the GATE simulation, indicating almost no loss of sensitivity in coincidence detection mode when PSR is used.

Table 4.3. System peak sensitivity using different methods

Methods	NoPR	LER	PSR	GATE
Sensitivity (%)	17.9	13.1	17.3	17.7

3) *NEMA NU-4 image quality phantom*: Figure 4.10 illustrates the NEMA NU-4 image quality phantom measurements acquired at 50 μCi using NoPR, LER and PSR. Obvious artifacts and spatial distortion can be observed in the NoPR images (Figure 4.10 (a)). For LER (Figure 4.10 (b)) and PSR (Figure 4.10 (c)), the artifacts and spatial distortion are significantly reduced. The uniformity improves from 15.3% (NoPR) to 10.9% (LER) and 10.2% (PSR), respectively. This result agrees with the synthetic pulse train simulation results shown in Table 4.2 and the measured flood image results shown in Figure 4.7 – 4.9, demonstrating that both LER and PSR can effectively suppress pileup caused mispositioned events.

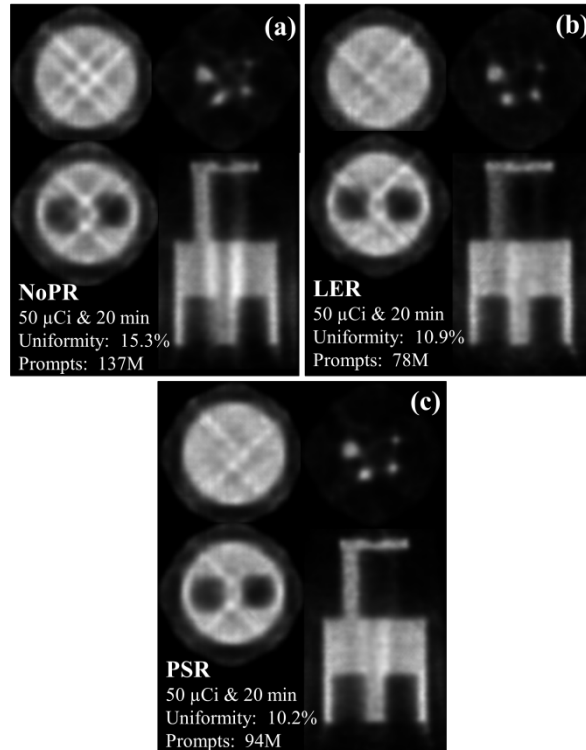


Figure 4.10 Image quality phantom images acquired at 50 μCi by (a) NoPR, (b) LER and (c) PSR.

Figure 4.11 illustrates the NEMA NU-4 image quality phantom measurements acquired at 4 μCi using NoPR, LER and PSR. For NoPR (Figure 4.11 (a)) and PSR (Figure 4.11 (c)), similar number of prompt counts (22 Million (M) for NoPR and 21 M for PSR) are obtained and similar uniformity (12.2% for NoPR and 12.1% for PSR) is measured. For LER (Figure 4.11 (b)), the uniformity deteriorates to 15.2% due to the 23 % prompt counts loss (17 M for LER versus 22 M for NoPR). This result agrees with the synthetic pulse train simulation results shown in Table 4.2 and the system peak sensitivity results shown in Table 4.3, indicating that LER trades off against sensitivity loss, while PSR performs more accurate rejection and avoids erroneous rejection and loss of sensitivity compared to LER.

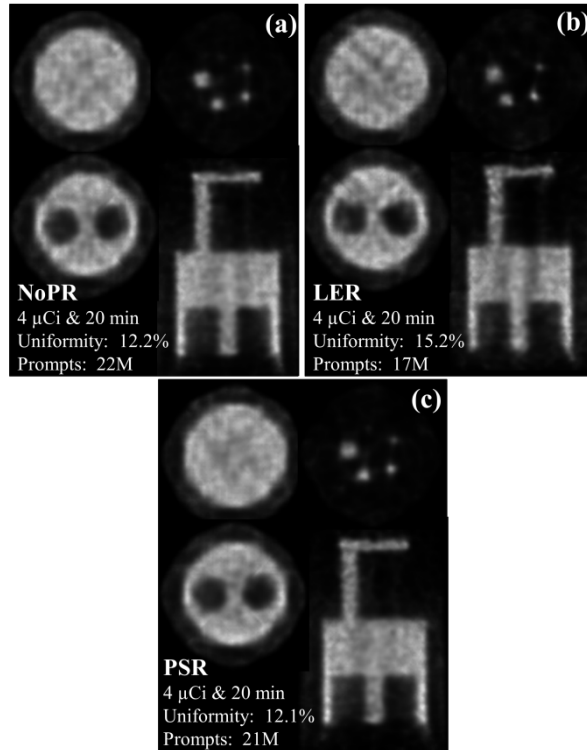


Figure 4.11 Image quality phantom images acquired at 4 μCi by (a) NoPR, (b) LER and (c) PSR.

Figure 4.12 illustrates the NEMA NU-4 image quality phantom measurements acquired at 50 μCi (Figure 4.12 (a)) and 4 μCi (Figure 4.12 (b)) using PSR and with the activity dependent normalizations applied. The uniformity further improves to 7% (50 μCi) and 11% (4 μCi), and the artifacts and spatial distortion are effectively suppressed. The activity at the NECR curve peak is around 40 μCi as reported in the PETbox4 count rate performance measurement in [8]. The NECR curve peak of the PETbox4 is reached primarily due to the detector saturation, caused by pileup events. The result shown in Figure 4.12 (a) demonstrates that with appropriate pileup rejection and normalization applied, optimal imaging performance can be achieved near the NECR peak activity.

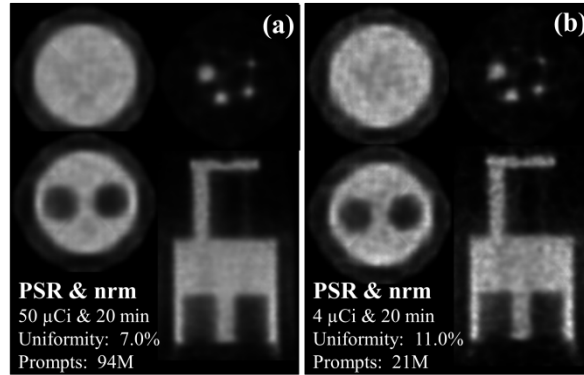


Figure 4.12 Image quality phantom images acquired by PSR at (a) 50 μCi and (b) 4 μCi . Activity dependent normalizations were applied respectively.

4.4 Discussion and conclusions

In this work, PSR, a novel pileup rejection method, is introduced and compared with the conventional LER method.

Conventional LER identifies pileup events based on the shape of the individual pulse waveform. As shown in Figure 4.2, the scintillation pulse output from the PETbox4 detector shows large statistical variations due to the low light output and long decay time of the BGO detector material. As a result, identification of pileup events superimposed on the tails of preceding events is challenging and therefore a fraction of pileup events might not be effectively identified. At the same time, statistical variations in the pulse of a non-pileup event might be inaccurately identified as the leading edge of a pileup event, leading to erroneous rejection and loss of sensitivity.

Both simulated and measured results in this work demonstrate that PSR achieves high accuracy in pileup rejection, maintaining no significant compromise in sensitivity at low activity levels. The better performance of PSR is mainly due to its identification scheme that takes into account the correlation of all the position encoding and energy pulses readout from a multiplexed detector. When a gamma photon interacts with a PETbox4 detector, the output x and y pulses

appear as their corresponding *sum* pulse scaled by factors that are proportional to the coordinates of that interaction point. In other words, the shapes of the *x*, *y* and *sum* signal waveforms are identical or similar, with the difference mainly on signal amplitudes. Due to the similar (correlated) statistical variations in the *x*, *y* position encoding signals and the *sum* signal, the effects of the pulse noise on calculated position values are cancelled out through the division, and the calculated positions for a non-pileup event converge rapidly and stay stable during the integration time, as shown in Figure 4.5 (a). This indicates that the noise in the pulse shape is less likely to lead to variation of the calculated position value. As a result, the erroneous rejection of non-pileup events and sensitivity loss can be avoided or suppressed. If a pileup event happens with two gamma photons detected at different locations of the detector within an integration time, the *x* and *y* position encoding signals will be contributed by different percentages from the first and the second interactions due to the location difference of the two interactions. This will break the correlation between the pulse shapes of the *x*, *y* position encoding signals and the *sum* signal. As a result, a clear shift in calculated event position values as a function of integration time can be obtained as the indication of the event pileup, as shown in Figure 4.5 (b).

The identification of event pileup acts as the first step of various pileup event recovery methods [2, 5, 6]. It might be possible to incorporate the proposed position shift based pileup identification scheme with other existing pileup recovery methods to further decrease the count rate loss and extend the dynamic range of the system. On the other hand, pileup event recovery is challenging as it will inevitably introduce additional noise on recovered events, leading to degradation on spatial and energy resolution and loss of image contrast. Pileup event recovery is currently under investigation and will be discussed somewhere else.

The application of PSR is not restricted to PET scanners. It is applicable to cameras that use multiple correlated signals to decode the location of interaction, such as conventional SPECT detectors and gamma cameras. The limitation of PSR is that it might not be applicable to counting (non-imaging) systems such as nuclear spectrometers or PET detectors with individual crystal readout, in which only one signal can be derived from individual detection. PSR can be implemented by employing integrators, comparators and registers, which can be easily achieved in most digital and analog systems without adding much to the complexity and production cost.

A comprehensive digital pulse library was developed in this work, in which pulses were directly recorded from real measurements. This method can incorporate events that better represent systematic variations of detection sensitivity for multiplexed detector panels due to differences in light sharing, light collection and crystal scatter among other effects. The pulse library bridges the gap between Monte Carlo simulations of the gamma interactions and pure electronics simulations of the data acquisition system. A synthetic pulse train generated from the digital pulse library was used to develop and evaluate the PSR method. The physical measurements were consistent with the simulated synthetic pulse train results, illustrating the theoretic validity, practical feasibility, and performance capability of the PSR method. It also demonstrated that the proposed evaluation mode based on synthetic pulses could contribute to the evaluation and optimization of the signal processing algorithm in PET.

4.5 References

- [1] G. Germano and E. J. Hoffman, "A Study of Data Loss and Mispositioning Due to Pileup in 2-D Detectors in Pet," *Ieee Transactions on Nuclear Science*, vol. 37, pp. 671-675, Apr 1990.
- [2] W. H. Wong and H. Li, "A scintillation detector signal processing technique with active pileup prevention for extending scintillation count rates," *Ieee Transactions on Nuclear Science*, vol. 45, pp. 838-842, Jun 1998.
- [3] A. Kuhn, S. Surti, J. S. Karp, G. Muehllehner, F. M. Newcomer, and R. VanBerg, "Performance assessment of pixelated LaBr3 detector modules for time-of-flight PET," *Ieee Transactions on Nuclear Science*, vol. 53, pp. 1090-1095, Jun 2006.
- [4] J. S. Karp, G. Muehllehner, D. Beerbohm, and D. Mankoff, "Event Localization in a Continuous Scintillation Detector Using Digital Processing," *Ieee Transactions on Nuclear Science*, vol. 33, pp. 550-555, Feb 1986.
- [5] T. K. Lewellen, A. N. Bice, K. R. Pollard, J. B. Zhu, and M. E. Plunkett, "Evaluation of a Clinical Scintillation Camera with Pulse Tail Extrapolation Electronics," *Journal of Nuclear Medicine*, vol. 30, pp. 1554-1558, Sep 1989.
- [6] X. Wang, Q. G. Xie, Y. B. Chen, M. Niu, and P. Xiao, "Advantages of Digitally Sampling Scintillation Pulses in Pileup Processing in PET," *Ieee Transactions on Nuclear Science*, vol. 59, pp. 498-506, Jun 2012.
- [7] Z. Gu, R. Taschereau, N. T. Vu, H. Wang, D. L. Prout, R. W. Silverman, *et al.*, "NEMA NU-4 performance evaluation of PETbox4, a high sensitivity dedicated PET preclinical tomograph," *Physics in Medicine and Biology*, vol. in press, 2013.
- [8] Z. Gu, R. Taschereau, N. T. Vu, H. Wang, D. L. Prout, R. W. Silverman, *et al.*, "NEMA NU-4 performance evaluation of PETbox4, a high sensitivity dedicated PET preclinical tomograph," *Phys Med Biol*, vol. 58, pp. 3791-3814, Jun 7 2013.
- [9] S. Siegel, R. W. Silverman, Y. P. Shao, and S. R. Cherry, "Simple charge division readouts for imaging scintillator arrays using a multi-channel PMT," *Ieee Transactions on Nuclear Science*, vol. 43, pp. 1634-1641, Jun 1996.

- [10] S. Jan, G. Santin, D. Strul, S. Staelens, K. Assie, D. Autret, *et al.*, "GATE: a simulation toolkit for PET and SPECT," *Physics in Medicine and Biology*, vol. 49, pp. 4543-4561, Oct 7 2004.

- [11] "Performance measurements of small animal positron emission tomographs," *Rosslyn, VA: Standards Publication NU 4-2008*, 2008, National Electrical Manufacturers Association.

- [12] R. Taschereau, F. R. Rannou, and A. F. Chatziioannou, "A modeled point spread function for a noise-free system matrix," in *IEEE Nuclear Science Symp. and Medical Imaging Conf.*, Oct. 2011, pp. 4102-5.

Chapter 5

The Next Generation:

A DOI Detector with Crystal Scatter Identification Capability for High Sensitivity and High Spatial Resolution PET Imaging

Chapter 5 The Next Generation

5.1 *Introduction*

Small animal PET has been a driving force behind the advances of molecular imaging that allows characterization and understanding of biological processes at the molecular level [1-3]. The use of mice as animal models for applications in pharmacology, genetics, pathology and oncology, demands preclinical PET scanners featuring high resolution and high sensitivity, to visualize subtle distribution and quantify low concentrations of PET probes [4]. Advances in spatial resolution and sensitivity performance of imaging systems can open up applications currently out of the range of PET because of resolution limitations, such as mouse brain imaging and early lesion and metastasis detection in mouse models of cancer [5]. Therefore, high sensitivity and high resolution have been pursued as some of the most important research goals for preclinical PET imaging [6]. For conventional pixelated scintillator detectors, the spatial resolution is determined by the cross section of the scintillator crystal elements [7]. The sensitivity can be increased by employing a compact system geometry to maximize the solid angle coverage, and by using long crystals for higher 511 keV gamma photon detection efficiency.

Unfortunately, long and narrow crystals in a small diameter gantry lead to increased penetration of oblique incident gamma rays before interaction. This causes event mispositioning also called parallax error, degrading the spatial resolution uniformity and distorting the appearance of the source [8]. Therefore, detectors with the capability of encoding the depth of annihilation photon interaction (DOI) are necessary. Much effort has been devoted to develop DOI PET detectors over the past several years [9-26]. Among those designs, phoswich detector

approaches [24-26] obtain DOI information by measuring differences in light decay time between multiple layers of different scintillators. The phoswich detector design has attracted considerable interest and has been employed in several prototype scanners and commercial systems [27-29]. Improved spatial resolution uniformity has been achieved in these phoswich DOI scanners compared to scanners of single layer design with equivalent scintillator volume and no DOI capability [30].

Inter-crystal scatter (ICS) events, for which the incoming annihilation photons interact with more than one detection element within the same block detector, is another cause of event mispositioning in addition to the parallax error. As the detection elements become narrower and longer, the fraction of these ICS events increases [31]. With conventional PET detector designs that employ Anger logic positioning schemes [32], such ICS events appear as inaccurate detections. The spatial coordinates corresponding to the energy weighted mean of the multiple interaction sites are different from the location of first interaction. This error in determining the initial interaction location reduces image contrast and degrades spatial resolution. This leads to degradation of the lesion detectability and quantitative characteristics of an imaging system [33, 34]. Therefore, appropriate ICS event identification and correction methods should be pursued if possible. Studies have shown that the capability of rejecting ICS events, or estimating the first interaction site of an ICS event using selection criteria [31, 35, 36], or maximum likelihood based on Compton kinematics [34, 37], yields improved image quality and quantification. However, those approaches require complicated and costly data acquisition systems for measuring individual interactions of the ICS events [22] and significant computational efforts for determining the location of first interaction [37], neither of which are available for conventional Anger logic detectors.

In this work, a phoswich depth of interaction (DOI) detector design composed by two layers of scintillator array made from cerium doped lutetium-yttrium oxyorthosilicate (LYSO) and bismuth germanate (BGO) is proposed. The aim of the detector design is to achieve high sensitivity and high spatial resolution PET imaging. The two layer detector configuration is designed to retrieve DOI information that will improve spatial resolution uniformity across the FOV. Furthermore, this detector allows identification of the majority of the cross layer crystal scatter (CLCS) events (the ICS events that deposit their energy in both layers), allowing a great reduction of this source of error. This new design is expected to be implemented in the next generation small animal PET tomograph being developed at the Crump Institute for Molecular Imaging, at UCLA.

5.2 Methods

5.2.1 Detector Description

The prototype detector configuration in this study was comprised of two layers of pixelated scintillator crystal arrays, a multi-element glass lightguide and a PSPMT.

The top (gamma ray entrance) layer was a 48 x 48 array of 1.01 x 1.01 x 7 mm³ LYSO crystals (1.09 mm pitch). The bottom (facing the PMT) layer was a 32 x 32 array of 1.55 x 1.55 x 9 mm³ BGO crystals (1.63 mm pitch). LYSO scintillator array elements were 9:4 (3×3 : 2×2) multiplexed coupled onto the corresponding BGO scintillator array elements. The LYSO and BGO crystal elements were mechanically polished on all sides with the exception of the exit ends which were diffusely ground. The four long sides of each individual crystal were bonded with a specular optical reflector (3M, St Paul, MN). The entrance surface of the LYSO array was

covered with four layers of Teflon tape to enhance reflection of the scintillation light onto the PSPMT.

To build a system capable of complete coverage of the whole body of the vast majority of laboratory mice in a single view without any bed motions, an axial FOV around 10 cm is required. In our previous PETbox4 system [38], a 1 mm thick glass lightguide was used to couple a 46 x 96 mm² scintillator array to two axially tiled PSPMTs to obtain a 96 mm axial FOV. Although all crystal pixels were successfully resolved, this simple lightguide suffered from degraded position decoding accuracy and energy resolution for edge crystals and crystals at the junction of the two PSPMTs due to the poorer light collection. Moreover, the transverse dimension of the scintillator array (46 mm) was limited by the effective area of the PSPMT, leading to incomplete angular data sampling and sensitivity loss in the PETbox4 system. In this work, a tapered, multiple-element glass lightguide was used to couple the exit end of the BGO crystal array (52x52 mm²) to the photosensitive area of the PSPMT (46x46 mm²). The complete individual detector module offers an overall dimension of 52x52 mm² that matches the external dimensions of the PSPMT package, which allows continuous positioning of the scintillator arrays for creating flat panel detectors without introducing gaps between detector modules.

The Hamamatsu H12700 PSPMT is used in this study. Compared to the H8500 PSPMT used in our previous PETbox4 system [38], the H12700 offers 45% higher photoelectron collection efficiency (boosted from 60% to 87%). The H12700 can be used as a direct replacement for the H8500 since its external dimensions and anode output characteristics are identical. Optical grease (BC-630, Saint-Gobain Crystals, Hiram, OH) was used for coupling between the two layers of scintillator arrays, the exit face of the BGO scintillator array to the entrance face of the lightguide, and the exit face of the lightguide to the PSPMT.

5.2.2 Simulation

To evaluate the characteristics and benefits of the proposed LYSO/BGO phoswich configuration, the Geant4 application for tomographic emission (GATE) Monte Carlo simulation software [39] was used to simulate the data acquired with a prototype two layer detector panel. The detector panel was comprised of a 48 x 96 array of LYSO crystals coupled to a 32 x 64 array of BGO crystals (created by continuously positioning two detector modules described in section II.A). A 10 μCi point source with isotropic emission of single 511 keV gamma photons was positioned 2.5 cm from the LYSO front layer surface, mimicking the emission from center of the FOV of our previous PETbox4 system [38]. An energy window of 50-650 keV was applied to the singles processing chain at the stage of initial simulation. To confine the investigation to the intrinsic detector characteristics of crystal scatter on positioning accuracy, no attenuation material was included between the source and the detector, and the phantom scatter was not considered. The lightguide and the scintillation light collection were not simulated. The Root format output from GATE [40] was used, which stores information of particle transportation and interactions on an event-by-event basis, allowing event history to be retrieved.

The detected singles events can be classified into six primary categories (as shown in Figure 5.1):

- (1) L: The energy deposited in the detector panel is contributed only from the interaction with the LYSO layer.
- (2) B: The energy deposited in the detector panel is contributed only from the interaction with the BGO layer.

- (3) C_1 : The gamma photon deposits its energy in both layers, with its first interaction at the LYSO layer. The energy deposited in the LYSO layer is smaller than that deposited in the BGO layer.
- (4) C_2 : The gamma photon deposits its energy in both layers, with its first interaction at the LYSO layer. The energy deposited in the LYSO layer is larger than that deposited in the BGO layer.
- (5) C_3 : The gamma photon deposits its energy in both layers, with its first interaction at the BGO layer. The energy deposited in the LYSO layer is smaller than that deposited in the BGO layer.
- (6) C_4 : The gamma photon deposits its energy in both layers, with its first interaction at the BGO layer. The energy deposited in the LYSO layer is larger than that deposited in the BGO layer.

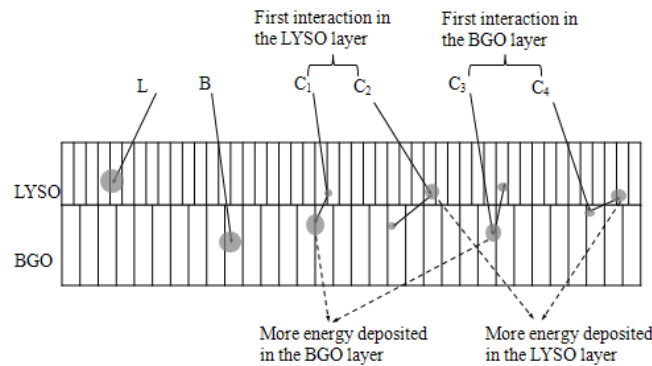


Figure 5.1. Illustration of different types of events: L: LYSO events, B: BGO events; C_1 ~ C_4 represent four types of cross layer crystal scatter (CLCS) events.

To retrieve the characteristics of the detected single events for appropriate event classification, customized software was developed in C++ to analyze the Root output file from

GATE. The interaction history of each detected event was investigated and the fraction representing each event type from the total number of interacting gammas was calculated.

5.2.3 Measurement

1) Readout

The 64 anode outputs from the PSPMT were multiplexed using a charge division resistor network [41] to four position encoding signals read out from four corner amplifiers. Due to the large difference in scintillation light output and decay time between LYSO and BGO (35000 photons/MeV vs 8000 photons/MeV; 42 ns vs 300 ns), the amplitude of the LYSO signal is 20~30 times higher than that of the BGO signal. To fit the LYSO signal within the dynamic range of the analogue-to-digital converters (ADC) (VHS-ADC, Nutaq, Quebec City, Quebec) without saturation, overall signal amplification is reduced. As a result, the BGO signal becomes too weak to overcome electronic noise, degrading the position decoding accuracy of the BGO events. In order to simultaneously retrieve accurate information from both the LYSO and BGO signals, a readout circuit was designed and constructed to amplify the detector response by two different factors, as shown in Figure 5.2: the signals from the route amplified with higher gain (x6) were used to detect BGO events, and the signals from the route with lower gain (x1) were used to detect the LYSO and CLCS events. The eight amplified analog signals from these two routes (four signals from each route) were applied with a low pass filter with a cut-off of -3 dB at 6 MHz to permit accurate subsequent digital conversion of the signals by eight 104 MHz free running ADCs on a signal processing card (VHS-ADC, Nutaq, Quebec City, Quebec). The digital samples are processed in a Xilinx Virtex-4 field programmable gate array (FPGA)

(Xilinx, San Jose, CA) in real time, including event triggering, pulse shape discrimination, and event energy and position calculation.

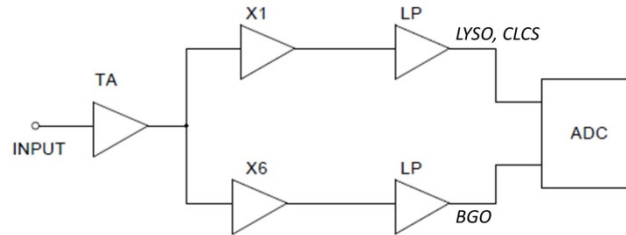


Figure 5.2. One of four identical signal processing circuits used for simultaneously acquiring LYSO, CLCS and BGO scintillation events. The input is from one corner of the charge division resistor network. TA is a transimpedance amplifier with a conversion gain of 750 mV/mA. LP is a low pass filter with a cut-off of -3 dB at 6 MHz.

2) *Pulse shape discrimination*

The four digitized position encoding signals in each route were summed in the FPGA, producing an energy pulse for pulse shape discrimination. The delayed charge integration (DCI) technique, an algorithm measuring the different light decay constants of two scintillators (LYSO = 42 ns, BGO = 300 ns) to identify event types was applied [24]. For each triggered event, the sum pulse was partially integrated with two intervals: 0-190 ns and 190-800 ns. The ratio of the 190-800 ns integration to the 0-190 ns integration, which depends on the characteristic light decay time of the scintillators, is defined as the DCI ratio in this study. The LYSO, BGO and CLCS events were identified based on the DCI ratio: detections with a DCI ratio less than 0.2 were identified as LYSO events; detections with a DCI ratio larger than 0.8 were assigned as BGO events; detections with a DCI ratio between 0.2 and 0.8 were classified as CLCS events. Based on the event type identified, the FPGA integrates BGO pulses for 800 ns and integrates LYSO and CLCS pulses for 190 ns, for subsequent event energy and position calculations that are recorded to the list-mode file.

3) Flood image and energy spectrum

A 0.25 MBq (6.9 μ Ci) ^{22}Na point source (Eckert & Ziegler Isotope Products, Valencia, CA) was placed approximately 3 cm from the top face of the LYSO array. For each detected event, the X and Y coordinates were calculated according to Anger logic [32]. Two-dimensional flood images for LYSO, BGO and CLCS events were acquired. The boundaries were determined for the BGO and LYSO flood images using a semi-automated program to define the crystal LUT that classifies regions in the flood image into the proper crystal of the scintillator arrays. Energy spectra for individual crystals were extracted based on the LUTs and a Gaussian function was fitted to the photopeak of each energy spectra. Energy resolution was measured for every crystal in the detector as the full width at half-maximum (FWHM) of the Gaussian function divided by the energy corresponding to the center of the photopeak, expressed as a percentage resolution. One dimensional profiles were extracted from the LYSO and BGO flood images and the average peak-to-valley ratios (PVR) for the selected profiles were reported.

5.3 Results

5.3.1 Simulation

Table 5.1. Fraction of different types of events illustrated in Figure 5.1

Type	L	B	C ₁	C ₂	C ₃	C ₄
fraction	54.2%	32.6%	9.8%	1.9%	1.2%	0.3%

The fractions of different types of events illustrated in Figure 5.1 are summarized in Table 5.1. In singles detection mode, the fractions of L (LYSO) and B (BGO) events are 54.2% and 32.6% respectively. The total fraction of singles CLCS events including C₁, C₂, C₃ and C₄ is

13.2%. Considering the coincidence events, the fraction of CLCS events will increase to around 25%, because a line of response (LOR) will be considered as a CLCS event as long as any one of the two single detections is a CLCS event.

Among the four types of the CLCS events, C_1 is the dominant component. This is consistent with the Compton kinetics that gamma rays preferentially scatter in the direction of the incident gamma ray, depositing a relatively smaller amount of energy in the crystal of first interaction, as also observed in [42]. The C_1 and C_4 types of events, corresponding to 77% of the total CLCS (10.1% out of 13.2%), deposit most of their energy in a scintillator layer different from the layer of first interaction. If a traditional anger logic positioning scheme is applied, those events will yield inaccurate position and DOI information. If these mispositioned events are included, they will degrade image contrast and spatial resolution. Identification of those events for rejection or correction may lead to significant improvements in imaging performance.

5.3.2 Measurement

Flood images and energy spectra of different event types are shown in Figure 5.3. The LYSO (Figure 5.3(a)) and BGO (Figure 5.3(b)) flood images were acquired with an energy window of 250-700 keV, as shown by the gray shaded areas in the energy spectra of LYSO (Figure 5.3(d)) and BGO (Figure 5.3(e)) events. More than 95 % of the LYSO and BGO crystals, including the majority of the edge crystals, were clearly resolved.

The CLCS events were acquired from the path with lower gain (x1) (Figure 5.2), which was also used to acquire the LYSO events. Therefore, the CLCS events use the same energy scale as that for the LYSO events. The CLCS flood image (Figure 5.3(c)) was acquired with an open energy window of 100-700 keV, as shown by the gray area in the energy spectra of CLCS

events (Figure 5.3(f)). A distinct pattern can be observed in the CLCS flood image, appearing as a blurred LYSO flood image. This is because the positions of the CLCS events are primarily determined by their LYSO signal component. As mentioned in section II.C.(2), the CLCS pulses were integrated for 190 ns to calculate the event position. Because LYSO has much higher light output and shorter decay time than BGO (35000 photons/MeV vs 8000 photons/MeV; 42 ns vs 300 ns), most of the CLCS event signal within the first 190 ns is contributed from the LYSO signal. In the CLCS energy spectra shown in Figure 5.3 (f), the energies of most CLCS events fall below 250 keV, which agrees with our simulation result that most CLCS events deposit less energy in the LYSO layer (C_1 and C_3 in Table 5.1, corresponding to 83% of the total CLCS events).

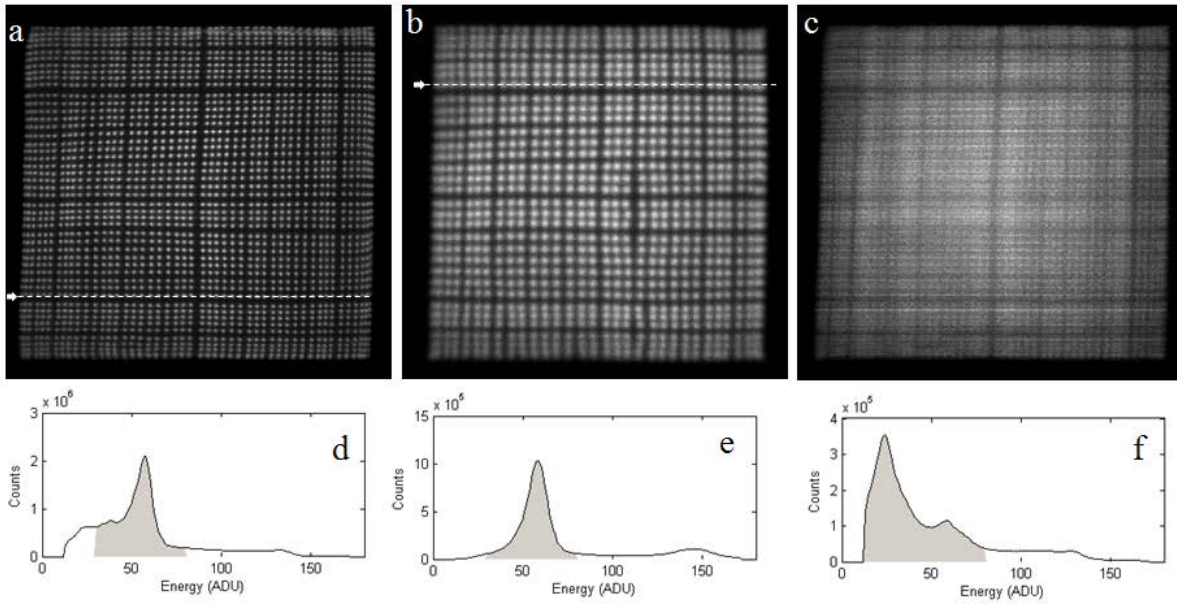


Figure 5.3. Flood images and energy spectra of the three types of events: LYSO flood image (a) and energy spectra (d); BGO flood image (b) and energy spectra (e); CLCS flood image (c) and energy spectra (f). The gray areas in energy spectra represent the events used to plot the flood images.

One-dimensional profiles across one row of the flood images are shown in Figure 5.4. The average PVR of these selected profiles were 3.5 for LYSO (Figure 5.4(a)) and 2.0 for BGO (Figure 5.4(b)).

The energy resolutions calculated from individual crystals are shown in Table 5.2. The average detector energy resolution derived by averaging those of the individual crystal spectra was $13.4 \pm 4.8\%$ for LYSO and $18.6 \pm 3.2\%$ for BGO (FWHM ± 1 SD). Crystal energy spectra representing the average, best, and worst energy resolution are shown in Figure 5.5 (LYSO) and Figure 5.6 (BGO). It is worth to note that these spectra include the 511 keV as well as the 1275 keV photopeaks present in ^{22}Na . The two peaks visible in a single photopeak in the worst LYSO and BGO energy spectra were due to the poorer spatial separation for the events detected in the edge crystals. Future improvement on energy resolution is possible if this edge crystal compression effect can be reduced.

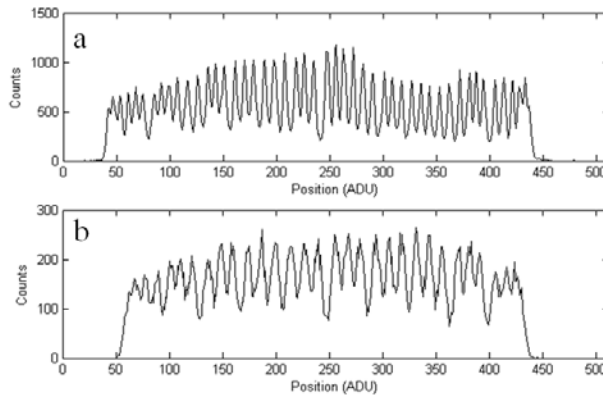


Figure 5.4. (a) Horizontal profile across one row of the LYSO flood histogram shown in Figure 5.3 (a); (b) Horizontal profile across one row of the BGO flood histogram shown in Figure 5.3 (b).

Table 5.2. Energy resolution of the LYSO/BGO phoswich detector

Scintillator	Mean (%)	Best (%)	Worst (%)
LYSO	13.4 ± 4.8	9.7	37.0
BGO	18.6 ± 3.2	16.0	33.9

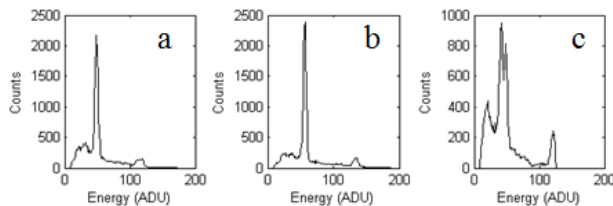


Figure 5.5. Energy spectrums of LYSO events representing the average (a), best (b) and worst (c) energy resolution.

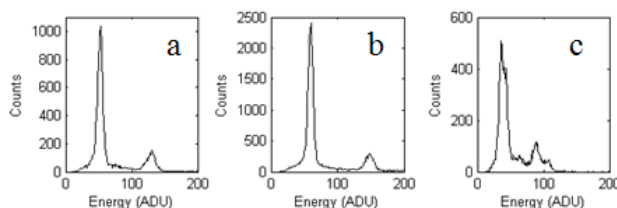


Figure 5.6. Energy spectrums of BGO events representing the average (a), best (b) and worst (c) energy resolution.

5.4 Discussion

A new phoswich detector is being developed, aiming to improve the sensitivity and spatial resolution for preclinical PET. BGO and LYSO, the most common scintillator materials for PET detectors, are employed in the phoswich detector configuration in this work. Both BGO and LYSO have high stopping power, resulting from their high effective atomic Z (75 and 62) and high density (7.13 g/cm^3 and 7.3 g/cm^3). Compared to equivalent size of detectors made from lower stopping power scintillators such as GSO, the detector made from BGO or LYSO yields higher sensitivity, reduced DOI effect resulting from the reduced crystal penetration, and reduced ICS events. The reduction of ICS events might lead to improvements in local image contrast.

In this work, the LYSO/BGO phoswich design has several particular advantages. Due to the large difference on light output and decay time of LYSO and BGO signals, three different

types of events (LYSO, BGO and CLCS) can be identified with high accuracy. As a result, the DOI information can be retrieved accurately for parallax error correction, leading to improved spatial resolution uniformity. In addition, the capability of identifying the majority of the CLCS events should lead to improved event positioning accuracy and local contrast resolution. Furthermore, this design is cost effective, as it only requires traditional anger logic and single end readout of the scintillation light. The delayed charge integration method for event type discrimination is simple and robust, and can be easily implemented in most digital or analog electronic systems.

Although rejecting ICS events increases the event positioning accuracy, it will inevitably lead to significant sensitivity loss [43]. Alternatively, estimating the first interaction site for ICS events has been proved to yield improved image quality and quantification [31, 34-37]. In this work, our simulation and measurement results indicate that the proposed detector design might enable the identification of the first interaction sites of the CLCS events. The simulations show that the first interaction sites for most CLCS events could be obtained if the LYSO signal component from a CLCS event can be extracted separately for event position calculation. As shown in Table 5.1, the C_1 and C_2 types of events, corresponding to 89% of the total CLCS (11.7% in 13.2%), encounter their first interactions in the LYSO layer. Our simulation results are also consistent with the studies of other groups showing that the “minimum DOI” [36] or “maximum Z” [31] crystal positioning scheme yields higher position detection accuracy for ICS events. In addition, our physical measurement indicates the potential to extract the LYSO signal component from the CLCS signal, due to the large difference of light output and decay time between BGO and LYSO. As shown in Figure 5.3(c), even without correcting the BGO signal component, a distinct pattern is observed in the CLCS flood image, appearing as a blurred LYSO

flood image. This pattern indicates that the BGO signal has relatively small effect on mispositioning CLCS events (with the integration time for CLCS events set to be 190 ns). On the other hand, accurately utilizing the LYSO signal component in a CLCS event might be challenging, as it requires the capability of resolving very low energy LYSO events (<250 keV) and appropriate modeling and correcting the weak BGO signal component. The first interaction identification algorithm for CLCS events is currently under investigation.

To provide whole-body mouse imaging with about the same volume resolution as obtained in human body scans, submillimeter spatial resolution should be pursued [4, 6]. In the proposed detector, two layers of the scintillator arrays with different crystal size were used, with the LYSO crystal (1.08 mm pitch) smaller than the BGO crystal (1.63 mm pitch). This approach fully takes advantage of the higher light output of the LYSO scintillator. Utilizing finer pixelated detector as an accessory for a coarse pixelated scintillator scanner has been proved to significantly improve the spatial resolution of the overall images, as shown in insert applications [44, 45]. Therefore, we expect the proposed detector in this work would also benefit from the finer pitch of the LYSO layer and potentially achieve submillimeter spatial resolution, should the detector and system response be appropriately modeled for image reconstruction.

The preliminary results presented in this work are meant to demonstrate the feasibility of the proposed approach. Important detector parameters such as crystal thickness and imaging system geometry configuration need to be determined with further investigation of how well the image reconstruction algorithm can compensate for the non-ideal detector response. The current readout of the proposed detector utilizes eight channels for simultaneously acquiring all three types of events from two routes of the signals as shown in Figure 5.2. A readout circuit is currently under construction in which the front end readout will be multiplexed by factor of two

before digitization to allow operation with only four channel readout per detector. This concept will be similar to the circuit design described in the OPET application [46].

5.5 Conclusion

In conclusion, this paper reports on the design and initial feasibility study of a new DOI detector for implementation in a next generation small animal PET system at UCLA. Both simulations and physical measurements demonstrate that the proposed detector is feasible and can potentially lead to a high spatial and contrast resolution, high sensitivity, and DOI PET system.

The individual modular detector design also provides flexibility in the configuration of large area detector plates and multiple-detector systems. Besides preclinical PET imaging, the proposed detector may also be used in neuro-imaging and other specialized imaging system like PEM where high spatial resolution and high sensitivity are also desired [6].

5.6 References

- [1] M. E. Phelps, "Positron emission tomography provides molecular imaging of biological processes," *Proc. Natl. Acad. Sci. U. S. A.*, vol. 97, pp. 9226-33, Aug 1 2000.
- [2] A. F. Chatziioannou, "Molecular imaging of small animals with dedicated PET tomographs," *Eur. J. Nucl. Med.*, vol. 29, pp. 98-114, Jan 2002.
- [3] R. Weissleder and U. Mahmood, "Molecular imaging," *Radiology*, vol. 219, pp. 316-333, May 2001.
- [4] S. R. Cherry, "In vivo molecular and genomic imaging: new challenges for imaging physics," *Phys. Med. Biol.*, vol. 49, pp. R13-R48, Feb 7 2004.
- [5] S. R. Cherry, "The 2006 Henry N.Wagner lecture: Of mice and men (and positrons) - Advances in PET imaging technology," *J. Nucl. Med.*, vol. 47, pp. 1735-1745, Nov 2006.
- [6] T. K. Lewellen, "Recent developments in PET detector technology," *Phys. Med. Biol.*, vol. 53, pp. R287-R317, Sep 7 2008.
- [7] J. R. Stickel and S. R. Cherry, "High-resolution PET detector design: modelling components of intrinsic spatial resolution," *Phys. Med. Biol.*, vol. 50, pp. 179-195, Jan 21 2005.
- [8] E. J. Hoffman, T. M. Guerrero, G. Germano, W. M. Digby, and M. Dahlbom, "Pet System Calibrations and Corrections for Quantitative and Spatially Accurate Images," *IEEE Trans. Nucl. Sci.*, vol. 36, pp. 1108-1112, Feb 1989.
- [9] W. H. Wong, "Designing a Stratified Detection System for Pet Cameras," *IEEE Trans. Nucl. Sci.*, vol. 33, pp. 591-596, Feb 1986.
- [10] N. Zhang, C. J. Thompson, F. Cayouette, D. Jolly, and S. Kecani, "A prototype modular detector design for high resolution positron emission mammography imaging," *IEEE Trans. Nucl. Sci.*, vol. 50, pp. 1624-1629, Oct 2003.
- [11] W. W. Moses and S. E. Derenzo, "Design Studies for a Pet Detector Module Using a Pin Photodiode to Measure Depth of Interaction," *IEEE Trans. Nucl. Sci.*, vol. 41, pp. 1441-1445, Aug 1994.

- [12] Y. F. Yang, P. A. Dokhale, R. W. Silverman, K. S. Shah, M. A. McClish, R. Farrell, *et al.*, "Depth of interaction resolution measurements for a high resolution PET detector using position sensitive avalanche photodiodes," *Phys. Med. Biol.*, vol. 51, pp. 2131-2142, May 7 2006.
- [13] T. Tsuda, H. Murayama, K. Kitamura, T. Yamaya, E. Yoshida, T. Omura, *et al.*, "A four-layer depth of interaction detector block for small animal PET," *IEEE Trans. Nucl. Sci.*, vol. 51, pp. 2537-2542, Oct 2004.
- [14] H. Murayama, H. Ishibashi, H. Uchida, T. Omura, and T. Yamashita, "Depth encoding multicrystal detectors for PET," *IEEE Trans. Nucl. Sci.*, vol. 45, pp. 1152-1157, Jun 1998.
- [15] N. Inadama, H. Murayama, M. Hamamoto, T. Tsuda, Y. Ono, T. Yamaya, *et al.*, "8-Layer DOI encoding of 3-dimensional crystal array," *IEEE Trans. Nucl. Sci.*, vol. 53, pp. 2523-2528, Oct 2006.
- [16] S. Yamamoto and H. Ishibashi, "A GSO depth of interaction detector for PET," *IEEE Trans. Nucl. Sci.*, vol. 45, pp. 1078-1082, Jun 1998.
- [17] Y. Yazaki, N. Inadama, F. Nishikido, T. Mitsuhashi, M. Suga, K. Shibuya, *et al.*, "Development of the X'tal Cube: A 3D Position-Sensitive Radiation Detector With All-Surface MPPC Readout," *IEEE Trans. Nucl. Sci.*, vol. 59, pp. 462-468, Apr 2012.
- [18] Y. P. Shao, X. S. Sun, K. J. A. Lan, C. Bircher, K. Lou, and Z. Deng, "Development of a prototype PET scanner with depth-of-interaction measurement using solid-state photomultiplier arrays and parallel readout electronics," *Phys. Med. Biol.*, vol. 59, Mar 7 2014.
- [19] H. N. Du, Y. F. Yang, J. Glodo, Y. B. Wu, K. Shah, and S. R. Cherry, "Continuous depth-of-interaction encoding using phosphor-coated scintillators," *Phys. Med. Biol.*, vol. 54, pp. 1757-1771, Mar 2009.
- [20] T. Ling, T. K. Lewellen, and R. S. Miyaoka, "Depth of interaction decoding of a continuous crystal detector module," *Phys. Med. Biol.*, vol. 52, pp. 2213-2228, Apr 21 2007.
- [21] Y. Gu, J. L. Matteson, R. T. Skelton, A. C. Deal, E. A. Stephan, F. Duttweiler, *et al.*, "Study of a high-resolution, 3D positioning cadmium zinc telluride detector for PET," *Phys. Med. Biol.*, vol. 56, pp. 1563-84, Mar 21 2011.

- [22] A. Vandembroucke, A. M. K. Foudray, P. D. Olcott, and C. S. Levin, "Performance characterization of a new high resolution PET scintillation detector," *Phys. Med. Biol.*, vol. 55, pp. 5895-5911, Oct 7 2010.
- [23] D. P. McElroy, W. Pimpl, B. J. Pichler, M. Rafecas, T. Schuler, and S. I. Ziegler, "Characterization and readout of MADPET-II detector modules: Validation of a unique design concept for high resolution small animal PET," *IEEE Trans. Nucl. Sci.*, vol. 52, pp. 199-204, Feb 2005.
- [24] J. Seidel, J. J. Vaquero, S. Siegel, W. R. Gandler, and M. V. Green, "Depth identification accuracy of a three layer phoswich PET detector module," *IEEE Trans. Nucl. Sci.*, vol. 46, pp. 485-490, Jun 1999.
- [25] A. Saoudi, C. M. Pepin, F. Dion, M. Bentourkia, R. Lecomte, M. Andreaco, *et al.*, "Investigation of depth-of-interaction by pulse shape discrimination in multicrystal detectors read out by avalanche photodiodes," *IEEE Trans. Nucl. Sci.*, vol. 46, pp. 462-467, Jun 1999.
- [26] J. B. Mosset, O. Devroede, M. Krieguer, M. Rey, J. M. Vieira, J. H. Jung, *et al.*, "Development of an optimized LSO/LuYAP phoswich detector head for the Lausanne ClearPET demonstrator," *IEEE Trans. Nucl. Sci.*, vol. 53, pp. 25-29, Feb 2006.
- [27] Y. C. Wang, J. Seidel, B. M. W. Tsui, J. J. Vaquero, and M. G. Pomper, "Performance evaluation of the GE healthcare eXplore VISTA dual-ring small-animal PET scanner," *J. Nucl. Med.*, vol. 47, pp. 1891-1900, Nov 2006.
- [28] P. S. Roldan, E. Chereul, O. Dietzel, L. Magnier, C. Pautrot, L. Rbah, *et al.*, "Raytest ClearPET (TM), a new generation small animal PET scanner," *Nucl Instrum Meth A*, vol. 571, pp. 498-501, Feb 1 2007.
- [29] H. W. A. M. de Jong, F. H. P. van Velden, R. W. Kloet, F. L. Buijs, R. Boellaard, and A. A. Lammertsma, "Performance evaluation of the ECAT HRRT: an LSO-LYSO double layer high resolution, high sensitivity scanner," *Phys. Med. Biol.*, vol. 52, pp. 1505-1526, Mar 7 2007.
- [30] J. Seidel, J. J. Vaquero, and M. V. Green, "Resolution uniformity and sensitivity of the NIH ATLAS small animal PET scanner: Comparison to simulated LSO scanners without depth-of-interaction capability," *IEEE Trans. Nucl. Sci.*, vol. 50, pp. 1347-1350, Oct 2003.

- [31] Y. P. Shao, S. R. Cherry, S. Siegel, and R. W. Silverman, "Study of inter-crystal scatter in small scintillator arrays designed for high resolution PET imaging," *IEEE Trans. Nucl. Sci.*, vol. 43, pp. 1938-1944, Jun 1996.
- [32] H. O. Anger, "Scintillation Camera," *Rev. Sci. Instrum.*, vol. 29, pp. 27-33, 1958.
- [33] C. S. Levin, M. P. Tornai, S. R. Cherry, L. R. MacDonald, and E. J. Hoffman, "Compton scatter and X-ray crosstalk and the use of very thin intercrystal septa in high-resolution PET detectors," *IEEE Trans. Nucl. Sci.*, vol. 44, pp. 218-224, Apr 1997.
- [34] Y. Gu, G. Pratx, F. W. Y. Lau, and C. S. Levin, "Effects of multiple-interaction photon events in a high-resolution PET system that uses 3-D positioning detectors," *Med. Phys.*, vol. 37, pp. 5494-5508, Oct 2010.
- [35] K. A. Comanor, P. R. G. Virador, and W. W. Moses, "Algorithms to identify detector Compton scatter in PET modules," *IEEE Trans. Nucl. Sci.*, vol. 43, pp. 2213-2218, Aug 1996.
- [36] R. S. Miyaoka and T. K. Lewellen, "Effect of detector scatter on the decoding accuracy of a DOT detector module," *IEEE Trans. Nucl. Sci.*, vol. 47, pp. 1614-1619, Aug 2000.
- [37] G. Pratx and C. S. Levin, "Bayesian reconstruction of photon interaction sequences for high-resolution PET detectors," *Phys. Med. Biol.*, vol. 54, pp. 5073-5094, Sep 7 2009.
- [38] Z. Gu, R. Taschereau, N. T. Vu, H. Wang, D. L. Prout, R. W. Silverman, *et al.*, "NEMA NU-4 performance evaluation of PETbox4, a high sensitivity dedicated PET preclinical tomograph," *Phys. Med. Biol.*, vol. 58, pp. 3791-3814, Jun 7 2013.
- [39] S. Jan, G. Santin, D. Strul, S. Staelens, K. Assie, D. Autret, *et al.*, "GATE: a simulation toolkit for PET and SPECT," *Phys. Med. Biol.*, vol. 49, pp. 4543-4561, Oct 7 2004.
- [40] R. Brun and F. Rademakers, "ROOT - An object oriented data analysis framework," *Nucl Instrum Meth A*, vol. 389, pp. 81-86, Apr 11 1997.
- [41] S. Siegel, R. W. Silverman, Y. P. Shao, and S. R. Cherry, "Simple charge division readouts for imaging scintillator arrays using a multi-channel PMT," *IEEE Trans. Nucl. Sci.*, vol. 43, pp. 1634-1641, Jun 1996.

- [42] P. Vaska, S. P. Stoll, C. L. Woody, D. J. Schlyer, and S. Shokouhi, "Effects of intercrystal crosstalk on multielement LSO/APD PET detectors," *IEEE Trans. Nucl. Sci.*, vol. 50, pp. 362-366, Jun 2003.

- [43] J. J. Vaquero, J. Seidel, S. Siegel, W. R. Gandler, and M. V. Green, "Performance characteristics of a compact position-sensitive LSO detector module," *IEEE Trans. Med. Imaging*, vol. 17, pp. 967-978, Dec 1998.

- [44] H. Y. Wu, D. Pal, T. Y. Song, J. A. O'Sullivan, and Y. C. Tai, "Micro Insert: A Prototype Full-Ring PET Device for Improving the Image Resolution of a Small-Animal PET Scanner," *J. Nucl. Med.*, vol. 49, pp. 1668-1676, Oct 2008.

- [45] D. Pal, J. A. O'Sullivan, H. Y. Wu, M. Janecek, and Y. C. Tai, "2D linear and iterative reconstruction algorithms for a PET-insert scanner," *Phys. Med. Biol.*, vol. 52, pp. 4293-4310, Jul 21 2007.

- [46] D. L. Prout, R. W. Silverman, and A. Chatziioannou, "Readout of the Optical PET (OPET) Detector," *IEEE Trans. Nucl. Sci.*, vol. 52, pp. 28-32, Feb 2005.

Chapter 6

Conclusions and Future Work

Chapter 6 Conclusions and Future Work

This chapter discusses the conclusions and future work of the studies presented in Chapters 2 through 5.

6.1 System development

Chapter 2 evaluates the basic performance of the PETbox4 system and its improvement over the previous system. Our results indicate a significant improvement in nearly all aspects of typical PET system characteristics compared with the first generation PETbox system. The energy resolution of the PETbox4 system averages 18% for the 511 keV photopeak. The volumetric image resolution remains around 3 μ L within the central 4-cm diameter FOV and is uniform along the radial, transverse and axial directions through the whole FOV. The peak sensitivity is 18% with a 150–650 keV energy window and a 20 ns timing window. The peak NEC rate is 35 kcps achieved at a total activity of 1.5MBq (40 μ Ci). The selected animal studies show that the system is capable of static and dynamic mouse imaging studies with different radiotracers. The overall performance demonstrates that the PETbox4 scanner is suitable for producing high quality images for molecular imaging based biomedical research, with less administered activity and lower dose delivered to the mice. At the same time, the cost derived from detectors and electronics as well as the system overall footprint is significantly reduced in this design compared with a more conventional ring-based preclinical PET tomographs.

Scatter correction techniques have not yet been explored or implemented for PETbox4. Future research will also be devoted to implementing adequate scatter correction methodology and evaluations on performing quantitative studies using this system. The MDA, as a combination of the more traditional PET system parameters, represents the performance of a

PET scanner at very low activity distributions and is directly related to lesion detection [1]. Novel molecular imaging applications, such as cell trafficking studies [2] or gene expression imaging [3], have brought the need to image small and low activity sources on the order of nano Curies under low contrast conditions. The PETbox4 system, with its high sensitivity and low intrinsic background, should achieve good MDA performance. A comprehensive evaluation of MDA for PETbox4 will be performed and compared with other systems in future work.

6.2 System optimization

6.2.1 Energy window optimization

In Chapter 3, the energy window of PETbox4 for whole body mouse scans has been optimized using GATE simulations. The event type classification described in this chapter provides a more accurate methodology and is important for imaging protocol optimization and system evaluation. For the pure positron emitting source investigated here, backscatter rejection did not prove useful and therefore was not developed for the PETbox4 system. An LLD of 350 keV was proposed as the optimized energy threshold. Analysis of the NEMA image quality phantom images further support the simulation based optimization. Due to the importance of object scatter and the significant differences of NECR and SF from the simulation with and without imaging chamber, it is concluded that reduction in attenuation introduced by the imaging chamber should be pursued. Furthermore, decreasing imaging chamber material will not change our conclusion on optimized energy window. The optimization in this study is not limited to PETbox4, but should also be applicable or helpful to other close geometry scanners [4-8].

In this study, NECR and SF were examined as the criteria for optimization. Contrast-to-noise ratio (CNR), as a more comprehensive figure of merit accounting for the influence from both NECR and SF, is strongly related to the lesion detectability, target localization and quantification accuracy of a system [9-11] and could perhaps be considered as part of protocol optimization and system design. While the choice of the LLD on NECR and SF have been discussed separately in this study, it is essential to understand the simultaneous effects and tradeoff of the changes of NECR and SF on CNR, as future investigation.

6.2.2 Pileup rejection

In chapter 4, PSR, a novel pileup rejection method, is introduced and compared with the conventional LER method. Both pulse train evaluation and physical measurements show that PSR performs more accurate rejection and avoids erroneous rejection and loss of sensitivity compared to about 26% sensitivity loss with the LER method. Optimal image quality can be achieved near the NECR peak activity with the help of PSR. The application of PSR is not restricted to PET scanners. It is applicable to cameras that use multiple correlated signals to decode the location of interaction, such as conventional SPECT detectors and gamma cameras. PSR can be implemented by employing integrators, comparators and registers, which can be easily achieved in most digital and analog systems without adding much to the complexity and production cost. A comprehensive digital pulse library was developed in this work, in which pulses were directly recorded from real measurements. The pulse library bridges the gap between Monte Carlo simulations of the gamma interactions and pure electronics simulations of the data acquisition system. A synthetic pulse train generated from the digital pulse library was used to develop and evaluate the PSR method. The physical measurements were consistent with the simulated synthetic pulse train results, illustrating the theoretic validity, practical feasibility, and

performance capability of the PSR method. It also demonstrated that the proposed evaluation method based on synthetic pulses significantly reduces the time and effort invested in the development and optimization of signal processing algorithms.

The identification of event pileup acts as the first step of various pileup event recovery methods [12-14]. It might be possible to incorporate the proposed position shift based pileup identification scheme with other existing pileup recovery methods to further decrease the count rate loss and extend the dynamic range of the system. On the other hand, pileup event recovery is challenging as it will inevitably introduce additional noise on recovered events, leading to degradation on spatial and energy resolution and loss of image contrast. Pileup event recovery is currently under investigation and will be discussed somewhere else. The overall count rate performance for the PETbox4 is mainly limited by the highly multiplexed detector readouts (four signals for groups of 1200 crystals) and the slow decay time of the BGO scintillation light. In the future, the count rate performance for the next generation system can be greatly improved by developing a less multiplexed readout, or employing a faster scintillator such as LYSO described in the phoswich DOI detector design in chapter 5.

6.3 The next generation

Chapter 5 reports on the design and initial feasibility study of a new DOI detector for implementation in a next generation small animal PET system at UCLA. Both simulations and physical measurements demonstrate that the proposed detector is feasible and can potentially lead to a high spatial and contrast resolution, high sensitivity, and DOI PET system. The individual modular detector design also provides flexibility in the configuration of large area detector plates and multiple-detector systems. Besides preclinical PET imaging, the proposed

detector may also be used in neuro-imaging and other specialized imaging system like PEM where high spatial resolution and high sensitivity are also desired [15].

Important detector parameters such as crystal thickness and imaging system geometry configuration need to be determined with further investigation of how well the image reconstruction algorithm can compensate for the non-ideal detector response. The current readout of the proposed detector utilizes eight channels for simultaneously acquiring all three types of events from two routes of the signal. A readout circuit is currently under construction in which the front end readout will be multiplexed by factor of two before digitization to allow operation with only four channel readout per detector. This concept will be similar to the circuit design described in the OPET application [16]. As discussed in this chapter, the proposed detector design might enable the identification of the first interaction sites of the CLCS events by accurately utilizing the LYSO signal component in a CLCS event. On the other hand, this first interaction sites estimation might be challenging, as it requires the capability of resolving very low energy LYSO events (<250 keV) and appropriate modeling and correcting the weak BGO signal component. The first interaction identification algorithm for CLCS events is currently under investigation.

References

- [1] Q. N. Bao and A. F. Chatziioannou, "Estimation of the minimum detectable activity of preclinical PET imaging systems with an analytical method," *Medical Physics*, vol. 37, pp. 6070-6083, Nov 2010.
- [2] N. Adonai, K. N. Nguyen, J. Walsh, M. Iyer, T. Toyokuni, M. E. Phelps, et al., "Ex vivo cell labeling with Cu-64-pyruvaldehyde-bis(N-4-methylthiosemicarbazone) for imaging cell trafficking in mice with positron-emission tomography," *Proceedings of the National Academy of Sciences of the United States of America*, vol. 99, pp. 3030-3035, Mar 5 2002.
- [3] R. Blasberg, "PET imaging of gene expression," *European Journal of Cancer*, vol. 38, pp. 2137-2146, Nov 2002.
- [4] H. Zhang, Q. Bao, N. T. Vu, R. W. Silverman, R. Taschereau, B. N. Berry-Pusey, et al., "Performance evaluation of PETbox: a low cost bench top preclinical PET scanner," *Mol Imaging Biol*, vol. 13, pp. 949-61, Oct 2011.
- [5] G. Alexandrakis, F. R. Rannou, and A. F. Chatziioannou, "Tomographic bioluminescence imaging by use of a combined optical-PET (OPET) system: a computer simulation feasibility study," *Phys Med Biol*, vol. 50, pp. 4225-41, Sep 7 2005.
- [6] M. Rodriguez-Villafuerte, Y. Yang, and S. R. Cherry, "A Monte Carlo investigation of the spatial resolution performance of a small-animal PET scanner designed for mouse brain imaging studies," *Phys Med*, vol. 30, pp. 76-85, Feb 2014.
- [7] G. Stortz, M. D. Walker, C. J. Thompson, A. L. Goertzen, F. Retiere, X. Zhang, et al., "Characterization of a New MR Compatible Small Animal PET Scanner Using Monte-Carlo Simulations," *Ieee Transactions on Nuclear Science*, vol. 60, pp. 1637-1644, Jun 2013.
- [8] P. Vaska, C. L. Woody, D. J. Schlyer, S. Shokouhi, S. P. Stoll, J. F. Pratte, et al., "RatCAP: Miniaturized head-mounted PET for conscious rodent brain imaging," *Ieee Transactions on Nuclear Science*, vol. 51, pp. 2718-2722, Oct 2004.
- [9] C. Lartizien, P. E. Kinahan, R. Swensson, C. Comtat, N. Lin, V. Villemagne, et al., "Evaluating image reconstruction methods for tumor detection in 3-dimensional whole-body PET oncology imaging," *Journal of Nuclear Medicine*, vol. 44, pp. 276-290, Feb 2003.
- [10] C. Lartizien, P. E. Kinahan, and C. Comtat, "Volumetric model and human observer comparisons of tumor detection for whole-body positron emission tomography," *Academic Radiology*, vol. 11, pp. 637-648, Jun 2004.
- [11] M. Brambilla, R. Matheoud, C. Secco, G. Sacchetti, S. Comi, M. Rudoni, et al., "Impact of target-to-background ratio, target size, emission scan duration, and activity on physical

- figures of merit for a 3D LSO-based whole body PET/CT scanner," *Med Phys*, vol. 34, pp. 3854-65, Oct 2007.
- [12] T. K. Lewellen, A. N. Bice, K. R. Pollard, J. B. Zhu, and M. E. Plunkett, "Evaluation of a Clinical Scintillation Camera with Pulse Tail Extrapolation Electronics," *Journal of Nuclear Medicine*, vol. 30, pp. 1554-1558, Sep 1989.
- [13] W. H. Wong and H. Li, "A scintillation detector signal processing technique with active pileup prevention for extending scintillation count rates," *Ieee Transactions on Nuclear Science*, vol. 45, pp. 838-842, Jun 1998.
- [14] X. Wang, Q. G. Xie, Y. B. Chen, M. Niu, and P. Xiao, "Advantages of Digitally Sampling Scintillation Pulses in Pileup Processing in PET," *Ieee Transactions on Nuclear Science*, vol. 59, pp. 498-506, Jun 2012.
- [15] T. K. Lewellen, "Recent developments in PET detector technology," *Physics in Medicine and Biology*, vol. 53, pp. R287-R317, Sep 7 2008.
- [16] D. L. Prout, R. W. Silverman, and A. Chatziioannou, "Readout of the Optical PET (OPET) Detector," *IEEE Trans Nucl Sci*, vol. 52, pp. 28-32, Feb 2005.